

PhD thesis

Cold Molecular Ions: Rotational State Preparation and Single Ion Reaction Experiments



Anders Kragh Hansen

Supervisor: Prof. Michael Drewsen

Danish National Research Foundation
Center for Quantum Optics - QUANTOP
Department of Physics and Astronomy
Aarhus University

September 2012

This Thesis is submitted to the Faculty of Science at Aarhus University, Denmark, in order to fulfill the requirements for obtaining the PhD degree in Physics.

The studies have been carried out under the supervision of Professor Michael Drewsen in the Ion Trap Group at the Department of Physics and Astronomy, Aarhus University, from August 2008 to July 2012.

Anders Kragh Hansen

Cold Molecular Ions: Rotational State Preparation and Single Ion Reaction Experiments

Aarhus University, 2012

Electronically available at <http://www.phys.au.dk/iontrap>

Acknowledgements

This thesis is a summary of the work I performed as a PhD student at the Department of Physics and Astronomy at Aarhus University. Prior to my application to the PhD programme, I had spent about half a year on the molecular ions project in the Ion Trap Group getting a taste for what experimental physics was really about. In february 2009, my supervisor Michael Drewsen accepted me into his group as a PhD student, allowing me to continue on the molecular ions project to explore this interesting field in greater depth.

I would like to thank the previous PhD student Klaus Højbjerg as well as the previous post-doc on the project, Peter Staantum, for showing me how to find my feet in experimental physics, especially for teaching me those essential laboratory skills that cannot be learned from textbooks. My thanks also go out to the latest PhD student to join the team, Magnus Sørensen, the post-doc that took over from Peter Staantum, Alex Gingell, and our lab assistant Simon Kristensen, who have all been a great help in the lab. The same goes for our friends from the Max-Planck-Institut für Kernphysik in Heidelberg, Maria Schwarz, Alexander Windberger and Oscar Versolato. And, of course, none of this would have happened without Michael Drewsen keeping us on the right track.

At the beginning of the MgH^+ rotational cooling experiments, we benefited greatly from the assistance of (then) masters student Peter Skyt, who had previously as his bachelors project characterized and set up the optics for the lead salt diode laser used for the rotational cooling results of the 2010 Nature Physics paper. Last but not least, I also have the rest of the Ion Trap Group to thank for providing good advice and being stimulating conversational sparring partners, and always being helpful with the more practical matters when working in a laboratory.

List of publications

- I. K. Højbjerg, A. K. Hansen, P. S. Skyt, P. F. Staantum and M. Drewsen. Rotational state resolved photodissociation spectroscopy of translationally and vibrationally cold MgH^+ ions: toward rotational cooling of molecular ions, *New Journal of Physics* **11**, 055026 (2009).
- II. P. F. Staantum, K. Højbjerg, P. S. Skyt, A. K. Hansen and M. Drewsen. Rotational laser cooling of vibrationally and translationally cold molecular ions, *Nature Physics* **6**, 271–274 (2010).
- III. A. K. Hansen, M. A. Sørensen, P. F. Staantum and M. Drewsen. Single-Ion Recycling Reactions, *Angewandte Chemie International Edition* **51**, 7960–7962 (2012).
- IV. M. Schwarz, O. O. Versolato, A. Windberger, F. R. Brunner, T. Ballance, S. N. Eberle, J. Ullrich, P. O. Schmidt, A. K. Hansen, A. D. Gingell, M. Drewsen and J. R. Crespo López-Urrutia. Cryogenic linear Paul trap for cold highly charged ion experiments, *Review of Scientific Instruments* **83**, 083115 (2012).
- V. M. Schwarz, O. O. Versolato, A. Windberger, J. Ullrich, J. R. Crespo López-Urrutia, A. K. Hansen, A. D. Gingell, F. Jensen and M. Drewsen. Decay rate of the MgH^+ rovibrational transition $|v = 1; J = 1\rangle_X \rightarrow |v = 0; J = 0\rangle_X$ measured in a Coulomb crystal, manuscript in preparation as of 2012.
- VI. Untitled manuscript describing rotational laser cooling and dissociative state preparation in the cryogenic CryPTEx trap with ensembles and single ions. Manuscript in preparation as of 2012.
- VII. Untitled manuscript describing helium buffer gas cooling in the cryogenic CryPTEx trap with ensembles and single ions and the effect of radiofrequency micromotion. Manuscript in preparation as of 2012.

Resumé på dansk (Summary in danish)

Kolde molekyler er et felt i hurtig udvikling. Blandt de mange anvendelser af kolde molekyler er kold kemi, der vil bidrage til en større forståelse af molekylær struktur og dynamik og af astrokemi, studiet af kemiske reaktioner i rummet imellem stjernerne, hvor temperaturer typisk ligger mellem 5 K og 100 K.

Metoder til nedkøling af molekylers bevægelsesfrihedsgrader er velfunderede og anvendes allerede bredt. Nedkøling af molekylers interne rotationelle frihedsgrader er dog endnu en stor udfordring. Derudover er det ofte svært at bestemme molekylers rotationelle fordeling eller deres rotationelle karakteristiske temperatur.

Dette PhD-arbejde har omhandlet implementeringen af REMPD (resonansforstærket multifoton dissociation) som et værktøj til på en meget direkte måde at karakterisere den rotationelle fordeling af magnesiumhydrid ioner, MgH^+ , in en lineær Paul ionfælde. Fra denne rotationelle fordeling kan en rotationel karakteristisk temperatur beregnes.

Ved hjælp af målinger lavet med denne metode er en ny laserbaseret teknik til nedkøling af den rotationelle frihedsgrad af MgH^+ molekyler blevet implementeret som del af mit PhD-arbejde, hvilket i et stuetemperaturmiljø har vist sig at være i stand til at nedbringe den rotationelle karakteristiske temperatur fra stuetemperatur, 297 K, til 18 ± 2 K. Denne teknik burde være generelt anvendelig på alle diatomare polære molekyler der kan holdes stationære i minutter, som fx molekylære ioner in en Paul ionfælde.

Målinger af samme art er foretaget i en kryogenisk fælde og resulterede i en nedkøling fra cirka 38 K til 10 K. Desuden er den rotationelle laserkøling og REMPD-metoden demonstreret på enkelte ioner, og en dissociativ præparationsmetode er implementeret. Rotationel køling med en kold buffer gas, helium, er også foretaget. Databehandlingen på disse eksperimenter er stadig under udarbejdning, så resultaterne er i skrivende stund præliminære.

Som et separat eksperiment er reaktionen mellem elektronisk exciterede calciumioner, Ca^+ , og hydrogendeuterid, HD, undersøgt i en ionfælde ved stuetemperatur. Den fraktionelle produktion af CaD^+ i forhold til de to mulige produkter CaH^+ og CaD^+ er bestemt til 59 ± 3 %, hvilket giver indblik i den involverede reaktionsdynamik. I dette eksperiment blev fotodissociation anvendt til at gendanne den oprindelige calciumion efter hver reaktion, en teknik der kan få stor betydning for muligheden for at eksperimentere på sjældne eller radioaktive isotoper og elementer. Endelig er det faktum at hele eksperimentet udførtes med enkeltioner vigtigt for perspektivet at udføre kold kemi med ioner.

Contents

Acknowledgements	i
List of publications	ii
Resumé på dansk (Summary in danish)	iii
Contents	iv
1 Introduction	1
2 Equipment and methods	4
2.1 Theory of ion production, trapping, Doppler cooling and identification	4
2.1.1 Photoionization	4
2.1.2 Linear Paul ion traps	6
2.1.3 Doppler laser cooling	11
2.1.4 Ion Coulomb crystals	15
2.1.5 Single ion mass measurement (SCSI-MS)	17
2.2 Experimental implementations	19
2.2.1 The room temperature vacuum chamber and attachments	19
2.2.2 Trap parameters	19
2.2.3 Laser systems	22
2.2.4 Fluorescence imaging	24
2.2.5 Formation of MgH^+	25
3 Design and construction of two resonant cavities for frequency doubling of laser radiation	26
3.1 General second harmonic generation theory	27
3.1.1 Determining the optimal waist	29
3.1.2 External resonant cavity theory	30
3.2 272 nm second harmonic generation cavity	37
3.2.1 Design	37
3.2.2 Construction	44
3.2.3 Characterization	45
3.3 559 nm second harmonic generation cavity	49
3.3.1 Design	49
3.3.2 Construction	52
3.3.3 Characterization	58

4	Rotational cooling and population distribution measurement:	
	Theory	63
4.1	Rotational cooling scheme for MgH^+	64
4.1.1	Vibrational and rotational levels of MgH^+	64
4.1.2	Black body radiation	64
4.1.3	Rovibrational optical pumping	65
4.1.4	Rate equation modeling	67
4.1.5	Determination of the MgH^+ A coefficients	69
4.2	REMPD population measurement scheme for MgH^+	73
4.2.1	Transitions	74
4.2.2	Pulse timing	75
5	Equipment and methods used for the MgH^+ rotational cooling	
	experiments	77
5.1	Mid-infrared laser sources	77
5.1.1	The PbSe diode laser setup	78
5.1.2	The Quantum Cascade laser setup	80
5.2	Near-infrared InP diode laser	84
5.3	Nanosecond pulse laser sources	84
5.3.1	Nd:YAG lasers	85
5.3.2	The Sirah pulsed dye laser	86
5.4	Determining the number of molecules	86
5.4.1	Theoretical considerations	86
5.4.2	Analysis procedure	87
6	Rotational cooling and state preparation of MgH^+ in a room	
	temperature trap	90
6.1	Method	90
6.2	Ensemble state distribution measurements	91
6.2.1	Single color dissociation	92
6.2.2	Two color dissociation	94
6.2.3	Characterization of systematic effects	96
6.3	Modelling the effect of collisions	101
6.3.1	Theoretical estimation of Γ_c	102
6.4	Single ion measurements	105
6.4.1	Likelihood theory	106
6.4.2	Results	108
6.5	Dissociative state preparation	110
6.5.1	Results	111

6.6	Conclusions	111
7	Rotational cooling of MgH⁺ in the cryogenic CryPTE_x ion trap	114
7.1	Characteristics of the cryogenic CryPTE _x trap and chamber . . .	115
7.1.1	Vacuum chamber	115
7.1.2	Ion trap	118
7.2	Theoretical modelling of rotational dynamics and equilibria . . .	118
7.3	Preliminary characterization of the dissociation process	120
7.3.1	Outline of the model	121
7.3.2	Experimental determination of γ and η	124
7.4	Ensemble state distribution measurements	125
7.5	Single ion measurements	128
7.6	Helium buffer gas cooling	130
7.7	Measurement of the MgH ⁺ $ v = 1; J = 1\rangle_X \rightarrow v = 0; J = 0\rangle_X$ decay rate	131
7.8	Preliminary conclusions	134
8	Ca⁺ + HD recycling reactions experiment	137
8.1	Motivation	137
8.2	Theory	138
8.2.1	Modelling the reaction process	139
8.3	Experimental procedure	142
8.3.1	q -purification of impurity ions	144
8.4	Results	144
8.4.1	Determination of the reaction rate constant	144
8.4.2	Determination of reactivity ratios	146
8.4.3	Photodissociation of CaO ⁺ and CaOH ⁺	147
8.5	Comparison with Mg ⁺ + HD results and conclusions	147
9	Summary	150
A	The Mg⁺ ion	152
A.1	Atomic data for Mg	152
A.2	Transition data for ²⁴ Mg ⁺	152
B	The MgH⁺ ion	153
B.1	Transitions in the ²⁴ MgH ⁺ ion	153

C	The Ca^+ ion	156
C.1	Atomic data for Ca	156
C.2	Transition data for $^{40}\text{Ca}^+$	156

Introduction

Over the last decade [1], cold molecules have attracted an increasing amount of attention within fields such as metrology and spectroscopy [2, 3, 4, 5], quantum information and computing [6, 7, 8], uni- and bi-molecular reaction dynamics [9, 10, 11, 12, 13] and astrochemistry [14]. In addition to the electronic and translational degrees of freedom associated with atomic species, molecules also possess both vibrational and rotational degrees of freedom. Thus the study of cold molecules can be viewed as an extension of the field of cold neutral or charged atoms and these extra degrees of freedom open up interesting new possibilities for quantum physicists and chemists. Dipole allowed rotational and vibrational transitions have much higher lifetimes than typical dipole allowed electronic transitions, which makes high internal coherence times possible, and the correspondingly narrow linewidths open up a new domain in high precision laboratory metrology.

These are certainly important fields! Besides providing new, more precise time standards, metrology also provides tests of theories going beyond the standard model by determining new bounds on the time evolution of the fundamental 'constants' [15, 16, 17] as well as quantities such as the electron dipole moment [18].

Astrochemistry is unlike typical Earth-based chemistry in that the temperatures are much lower, typically from 5 to 100 K [19, 20]. When the temperature is low, even small potential barriers can completely block reaction paths, and alignment effects of molecules due to external fields start to play a large role in reaction dynamics [21]. As a consequence, there are many unknowns concerning reaction channels and rates in space as well as in the laboratory. Investigating uni- and multimolecular reactions between cold molecules in the laboratory is therefore another exciting application of cold molecules.

In quantum information and computing, having long coherence times and controllable interactions is of critical importance. Rotationally excited states in the vibronic ground state provide a low enough rate of spontaneous emission that the internal state coherence can, in principle, last for minutes.

Working with molecules offers new challenges as well, however, one of which is the lack of general applicability of Doppler laser cooling schemes. The presence of the many rovibrational states precludes the implementation of a closed electronic cooling cycle, with few exceptions [22, 23, 24].

Cold neutral molecules have been produced by a number of different tech-

niques so far, mostly within the following fields: photoassociation of laser cooled atoms [25, 26, 27], buffer gas cooling of molecules in magnetic traps [28], Stark deceleration [29, 30], electrostatic quadrupole filtering [31], trapping of molecules by electrostatic fields [32, 33, 34] and formation through Feshbach resonances in a Bose-Einstein condensate [35, 36] and from a thermal gas [37]. Stimulated Raman adiabatic passage and shaped femtosecond pulses have been used to transfer molecules to the vibrational ground state [38, 39, 40, 27]. Photoassociated molecules have also been formed directly in the rovibrational ground state [41].

For molecular ions, helium buffer gas together with cryogenically shielded 22-pole ion trap environments has been used to bring molecular ions to low temperatures [9, 42, 43, 44], although accurate and direct measurement of the temperatures or rotational distributions is still being worked on. A lot of development has been occurring through the use of molecular ions sympathetically cooled by laser cooled atomic ions [45, 46, 47, 48, 49, 50, 51, 52, 53], and cold chemistry has been studied between cold atoms and cold molecules [54, 55]. Atomic ions have also been trapped and sympathetically cooled inside Bose-Einstein condensates [56, 57], opening new possibilities [58] for ion-neutral reaction studies.

As I mentioned above, accurately measuring the rotational distribution of the molecules in question is a challenge. Various methods have been used to estimate a characteristic temperature or the actual rotational distribution, including laser-induced endothermic reactions [59, 60], radiative association [43] and laser-induced charge transfer [61]. For our experiments with MgH^+ , a Resonance Enhanced Multi-Photon Dissociation (REMPD) scheme was implemented to probe the population in any given rotational state in a clear way and with high efficiency. Such measurements of the full rotational distributions are desirable compared to simple temperature estimates since many of the various cooling mechanisms or preparation schemes used in the literature should not be expected to equilibrate thermally and the molecules in question are subject to more heating mechanisms than one might assume.

In the Ion Trap Group, MgH^+ molecules are routinely formed, trapped and sympathetically cooled by the Coulomb interaction with Doppler laser cooling Mg^+ in an ion trap. By this method, the molecular translational temperature is reduced to less than 100 mK [62]. Starting from this point, a significant part of my PhD project consisted of applying the efficient REMPD detection scheme to accurately measure rotational population distributions of the molecules and to achieve laser-induced cooling of the internal rotational degree of freedom based on a proposal by Ivan Vogelius *et. al.* in 2002 [63]. These experiments

were carried out both with Coulomb crystal ensembles and with single ions, and additionally a dissociative state preparation scheme was applied to further improve the state preparation. We first applied these techniques in a room temperature trap, and these experiments are described in chapter 6.

Subsequently, these techniques were implemented in a cryogenically cooled trap given the name CryPTEx, constructed at the Max-Planck-Institut für Kernphysik in Heidelberg and moved to the Ion Trap Group in Aarhus for the duration of the MgH^+ experiments; this is described in chapter 7. In the CryPTEx trap, experiments with He buffer gas cooling were also carried out in addition to a measurement of the decay rate $|v = 1; J = 1\rangle_X \rightarrow |v = 0; J = 0\rangle_X$, a parameter crucial to the efficiency of the rotational cooling scheme. To allow comparison of experiment with recent theory, assistance was obtained from theoretical chemist Frank Jensen, who re-computed simulations performed by Ivan Vogelius in 2002 in order to leverage the superior processing power of the latest computers. The theoretical results are presented in section 4.1.5 and appendix B, while the experimental measurements are presented in section 7.7.

Two articles were published based on the room temperature measurements and so far one has been published based on measurements in the CryPTEx chamber. With the amount and quality of data that has been gathered on the cryogenic system so far, it is expected that two or three more articles will follow describing the latest findings in the CryPTEx experiments.

We also performed an experiment on single Ca^+ ions. It consisted of investigating isotope effects in the $\text{Ca}^+ + \text{HD} \rightarrow \text{CaH(D)}^+ + \text{D(H)}$ reaction, determining the fractional formation of CaD^+ out of the two possible reaction outcomes. In this experiment, after successful identification of the product ion, a photodissociation laser pulse was applied to regenerate the reactant Ca^+ , enabling collection of large amounts of reaction statistics with only a single pair of ions, without any need to reload the trap. A description of these experiments is provided in chapter 8.

In order to facilitate these experiments, I constructed two external resonant frequency doubling cavities to serve as sources of coherent radiation at the wavelengths 272 nm and 559 nm. The cavity for 559 nm light was constructed with the assistance of bachelors student Kåre Bitsch. The light at 272 nm is used for photoionization of Ca atoms and 559 nm light is used, after another doubling step, for Doppler laser cooling of Mg^+ ions. The construction and characterization of these doubling cavities is described in chapter 3.

Chapter 2

Equipment and methods

A wide variety of techniques are applied to create, control and manipulate ions in a laboratory. In this chapter I will cover the basics of the techniques and equipment that had been taken in use prior to my arrival in the Ion Trap Group. Because the development of the theory and equipment did not form part of the work I performed in the group, the descriptions will be cursory. For greater detail, see the theses and articles in which the schemes and equipment were first introduced [64, 65, 46]. The equipment and schemes taken in use as a part of the experiments I performed during my PhD are presented in the chapters corresponding to those experiments.

2.1 Theory of ion production, trapping, Doppler cooling and identification

Photoionization of neutral atoms (section 2.1.1), trapping of ions in ion traps (section 2.1.2) and Doppler laser cooling (section 2.1.3) form the cornerstones of working with ions in the Ion Trap Group. When a collection of ions are trapped and cooled to temperatures below ~ 100 mK, they form a rigidly ordered structure known as a Coulomb crystal—the relevant characteristics of this structure is covered in section 2.1.4. In the same section you will find the concept of sympathetic cooling, a method of cooling the motion of ions that cannot be directly laser cooled. Finally, a method for measuring the mass of single ions in a Paul trap, Sympathetically Cooled Single Ion Mass Spectrometry (SCSI-MS), is introduced in section 2.1.5.

2.1.1 Photoionization

In both of the vacuum chambers used for the experiments in this thesis, ions are produced by crossing a skimmed beam of neutral atoms (either Ca or Mg) from a hot effusive source with a laser photoionization beam in the center of the ion trap.

There are also other techniques for ionizing neutral atoms and molecules for ion experiments. One of the most general is electron impact ionization, which under suitable conditions can be used to strip electrons off of any atomic species and molecule. This strength is also a major weakness, in that the process is non-

selective and will typically ionize many unwanted atoms and molecules, which will disrupt the experiment unless they can be removed from the ionic ensemble, for example by means of a - or q -purification (see section 2.1.2), which will not in general be possible or practical.

The technique used for all experiments in this thesis, photoionization, is a much more efficient and highly selective method. The photoionization scheme consists of a resonance enhanced multiphoton process consisting of exciting a neutral target atom or molecule through a non-ionizing intermediate state into the ionization continuum. Although this method requires a suitable laser source for driving the transitions, it will in general provide not just element and molecule selectivity but also isotope selectivity. A further important argument for using photoionization rather than electron impact ionization is that the weak laser beam sufficient for photoionization will lead to far less charging of insulators near the ion trapping area than an electron beam. Such patch potentials on insulators would provide temporary uncontrollable drifts of the trapping parameters, which would make some techniques such as SCS-MS (see section 2.1.5) or sideband cooling [66] impractical or impossible. Furthermore, because of the high efficiency of the photoionization process, a lower atomic flux is necessary and the oven source can thus typically be operated at a significantly lower temperature. This means the atomic source will have less of an impact on the vacuum chamber pressure.

Photoionization of Ca

The resonance enhanced two-photon process used for photoionizing calcium is depicted in figure 2.1, along with the ionization spectrum showing isotope selectivity. Starting from the ground state $4s^2\ ^1S_0$ of neutral Ca, the $4s5p\ ^1P_1$ state can be resonantly reached with 272 nm light, after which further excitation to the ionization continuum is done either with another 272 nm photon, a 397 nm photon from the simultaneously applied Doppler cooling scheme or by decay to the metastable $4s3d\ ^1D_2$ state followed by absorption of another 272 nm photon.

Photoionization of Mg

Similarly to the Ca photoionization scheme, an ultraviolet laser beam of wavelength 285 nm resonantly excites Mg atoms from the ground state $3s^2\ ^1S_0$ to the excited state $3s3p\ ^1P_1$ (see figure 2.2), from which coupling to the ionization continuum can be performed either through an additional 285 nm photon or from a photon from the simultaneously applied 280 nm Doppler cooling beam.

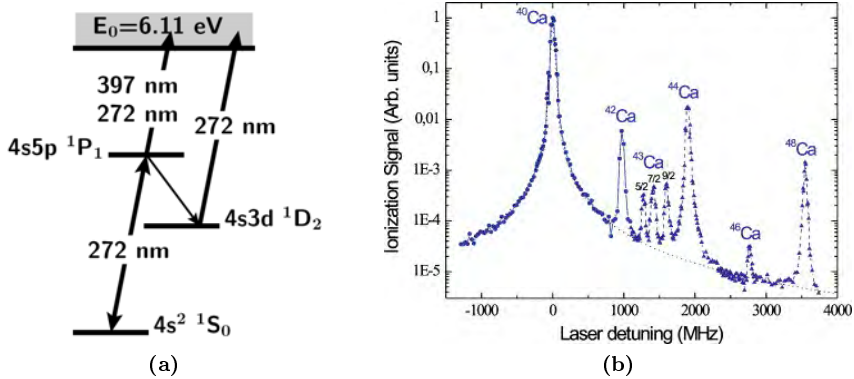


Figure 2.1: Photoionization of Ca. (a): (From [46]) Sketch of the energy levels in Ca involved in the photoionization scheme. (b): (From [67]) The spectrum of photoionization of Ca. As the photoionization laser is scanned, ionization peaks are observed corresponding to each of the stable isotopes of Ca, with peak heights corresponding to the relative natural abundances (see appendix C).

As in the case of Ca, efficient isotope selective Mg^+ loading is achieved [68].

2.1.2 Linear Paul ion traps

The principle of an ion trap is to provide confinement in all three spatial dimensions for the desired ion species by applying suitable voltages to electrodes and, in some cases, maintaining a magnetic field in the trapping region. There are several different types of ion traps, such as Penning traps, Electron Beam Ion Traps (EBITs) and Paul traps. While both Penning traps and EBITs involve magnetic fields, confinement in the Paul trap is achieved using only electric fields. A variety of Paul trap designs exist, including blade traps, surface traps, the so-called "3D" Paul trap utilizing a cylindrically symmetric ring electrode around the trapping region and finally the linear Paul trap using a number of parallel electrode rods, usually 22 or 4. These rods can then be segmented to provide extra flexibility, as shown in figure 2.3. Since the only type of ion trap used in the Ion Trap Group is the segmented 4 rod linear Paul trap, I will lay out the theory and equations for such a trap, with 3 segments per rod.

To understand how the three-dimensional confinement is established in free space in the middle of such an electrode configuration we must remember Earn-

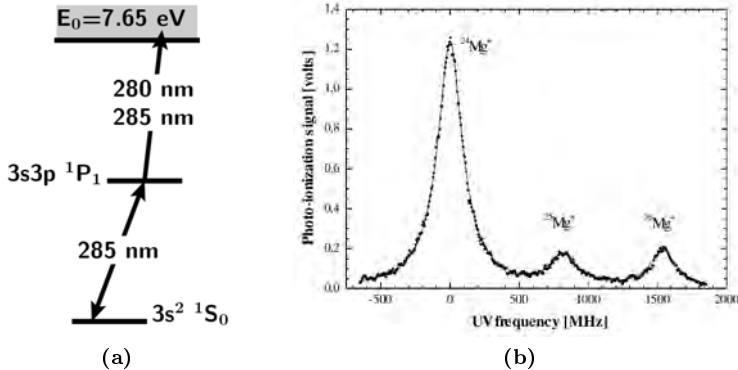
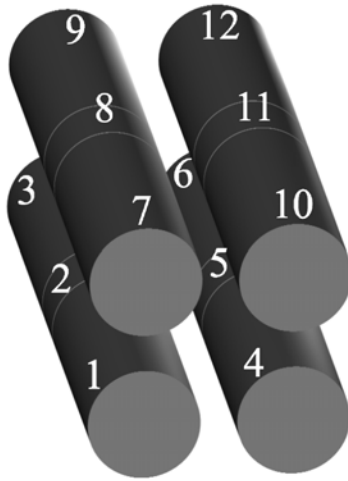


Figure 2.2: Photoionization of Mg. (a): (From [46]) Sketch of the energy levels in Mg involved in the photoionization scheme. (b): (From [68]) The spectrum of photoionization of Mg. Just as in the case of Ca, as the photoionization laser is scanned, ionization peaks are observed corresponding to each of the stable isotopes of Mg with peak heights corresponding to the relative natural abundances (see appendix A).

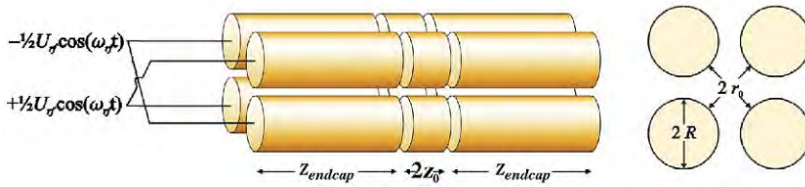
shaw’s theorem, which states that it is impossible to create a potential minimum in free space for charged particles by applying static potentials to any set of electrodes. While this is true for static potentials, it is possible to create an effectively confining potential by applying rapidly oscillating radiofrequency (rf) electric potentials, as I will explain below.

Figure 2.3 shows a simple sketch of the 3-segment 4 rod linear Paul trap. Confinement in the axial direction, parallel to the electrodes, is provided by a positive electrostatic bias U_{end} applied to the 8 outermost segments, while confinement in the radial direction, perpendicular to the electrodes, is instead provided as in a quadrupole mass filter: An oscillating quadrupole electric field is created at the trap center axis by further adding a radiofrequency voltage $\pm \frac{1}{2}U_{\text{rf}} \cos(\omega_{\text{rf}}t)$, where the + phase is applied to one diagonal pair of rods and the – phase to the other pair. As is the case for the quadrupole mass filter, this leads to confinement only for a limited interval of ion mass M to charge Q ratios.

Considering only the volume close to the center of the trap, we can ignore edge effects of the generated electric fields. The electric field contribution from the rf potential thus does not have an axial (z) component. The only axial field is therefore that provided by the endcap bias, U_{end} . Determining the electric



(a)



(b)

Figure 2.3: (From [64]) Sketch of a 4 rod linear Paul ion trap with 3 segments per rod, the type of trap used in the Ion Trap Group. Electrodes 1, 3, 4, 6, 7, 9, 10 and 12 are the endcap electrodes, on which a positive bias U_{end} is applied to provide axial confinement. Radial confinement is provided by an additional radiofrequency oscillating potential $\pm \frac{1}{2}U_{rf} \cos(\omega_{rf}t)$ applied to the rods. The + phase is added to 1, 2, 3, 10, 11 and 12, while the - phase is added to electrodes 4, 5, 6, 7, 8 and 9.

potential $V(z, r = 0)$ on the axis near the trap center as a function of endcap bias is in general done in numerical simulations, and a harmonic approximation is made. From these geometric simulations, a dimensionless geometric constant η is introduced to satisfy

$$V(x = 0, y = 0, z) = \eta U_{\text{end}} \frac{z^2}{z_0^2} \quad (2.1)$$

where z_0 is defined in figure 2.3b.

Although the endcap bias thus provides axial confinement, it necessarily also introduces a defocusing radial potential contribution due to Gauss' law in charge free space, $\nabla^2 V = 0$. The radial electric potential is then a sum of the defocusing term from the endcap bias and the instantaneous rf contribution,

$$V(x, y, z = 0, t) = -\frac{\eta U_{\text{end}}}{2} \frac{x^2 + y^2}{z_0^2} - \frac{U_{\text{rf}}}{2} \frac{x^2 - y^2}{r_0^2} \cos(\omega_{\text{rf}} t) \quad (2.2)$$

where r_0 is also defined in figure 2.3b.

While the axial motion of a hypothetical test charge will be simple harmonic, the motion in the radial plane is more complicated. Introducing the dimensionless quantities

$$\tau = \frac{\omega_{\text{rf}} t}{2}, \quad a_x = a_y = -4 \frac{\eta U_{\text{end}}}{\omega_{\text{rf}}^2 z_0^2} \frac{Q}{M} \quad \text{and} \quad q_x = -q_y = 2 \frac{U_{\text{rf}}}{\omega_{\text{rf}}^2 r_0^2} \frac{Q}{M} \quad (2.3)$$

one can write the equations of motion for the two radial directions on the form

$$\frac{\partial^2 u}{\partial \tau^2} + (a_u - 2q_u \cos(2\tau)) u = 0, \quad u = x, y \quad (2.4)$$

This type of equation is called a Mathieu equation and can, for each dimension, be solved to determine the trajectory of a test charge. It turns out that these trajectories are unbounded for some values of (q, a) and bounded for other values. The regions in (q, a) -space resulting in bounded trajectories are referred to as the stable trapping regions and are depicted in figure 2.4 as the gray areas. Since U_{end} must be positive to provide axial confinement, a will be negative for the radial dimensions. The region corresponding to three dimensional confinement is thus the one shaded in the right panel of figure 2.4.

Since both a and q are directly proportional to $\frac{Q}{M}$, different ion species will in general have different a and q parameters associated with them and may be radially confined or not. Trapping several different ion species in a Paul trap

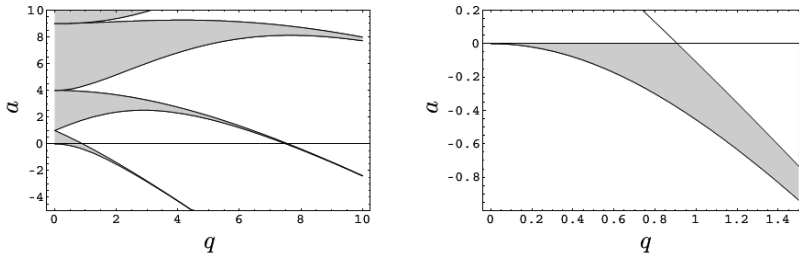


Figure 2.4: (From [65]) Graphs of the stability regions of the Mathieu equation. (q, a) values that have bounded solutions are shaded in gray. The white areas correspond to unbounded solutions. The stability regions are mirrored in the a -axis. In a Paul trap, one will typically operate with $|q| < 0.4$ and $-0.1 < a < 0$.

simultaneously thus requires them to have comparable charge to mass ratios. As in a quadrupole mass filter, one can expel unwanted ion species in this way by carefully choosing the trapping parameters so that the unwanted species have (q, a) outside the stable region while the desired species still lie within the stable region. Such a purification can be done by experimentally varying either U_{end} or U_{rf} , referred to as a - and q -purification, respectively. In chapter 8, q -purification is used extensively to remove spuriously formed ions from the trapping region.

For $|a|, |q| \ll 1$ and (q, a) within the stable trapping region, the particle trajectory solution to the Mathieu equation can be written

$$u(t) = u_0 \left(1 - \frac{q_u}{2} \cos(\omega_{\text{rf}} t) \right) \cos(\omega_r t), \quad u = x, y \quad (2.5)$$

where we have introduced the so-called secular frequency

$$\omega_r = \frac{\sqrt{q^2/2 + a}}{2} \omega_{\text{rf}} \quad (2.6)$$

This motion consists of a slowly oscillating part with angular frequency ω_r called the secular motion, and a fast oscillating motion with amplitude proportional to the secular excursion and angular frequency ω_{rf} called the micromotion. Although we will return to consider the consequences of micromotion later, we will for now regard only the time-averaged motion $u(t) = u_0 \cos(\omega_r t)$, which is simple harmonic motion.

In summary, when micromotion is averaged out, a test charge in the Paul trap near the trap center under normal trapping conditions will move as in a

three dimensional harmonic pseudopotential

$$\phi_{\text{ps}}(r, z) = \frac{1}{2}M (\omega_z^2 z^2 + \omega_r^2 r^2), \quad r^2 = x^2 + y^2 \quad (2.7)$$

where

$$\omega_z^2 = -\frac{a}{2}\omega_{\text{rf}}^2 = \frac{2\eta U_{\text{end}}}{z_0^2} \frac{Q}{M} \quad (2.8)$$

and

$$\omega_r^2 = \frac{q^2/2 + a}{4}\omega_{\text{rf}}^2 = \frac{U_{\text{rf}}^2}{2\omega_{\text{rf}}^2 r_0^4} \left(\frac{Q}{M}\right)^2 - \frac{\eta U_{\text{end}}}{z_0^2} \frac{Q}{M} \quad (2.9)$$

2.1.3 Doppler laser cooling

At the time of ionization, the newly formed ions will be translationally hot, and although they experience the trapping pseudopotential of the ion trap, the radiofrequency oscillations also contribute to further heating of the ions. Unless some cooling scheme is applied, the ions will quickly escape and the experiment will be a very short one.

Doppler laser cooling is a technique that has been widely adopted in atomic and molecular physics and is well explained in many articles and textbooks [69, 70]. In this thesis I will only provide the basics, encouraging the reader to look to the references for greater detail. Doppler laser cooling relies on the momentum transfer in the atomic absorption process as well as velocity dependence on absorption probability caused by the Doppler shift of the atom relative to the source. I will illustrate the principle in a one-dimensional case and generalize to three dimensions.

We consider a two-level atom with resonance frequency ω_a moving in one dimension with a velocity v . Two counter-propagating laser beams with frequency ω_L in a laboratory fixed frame are incident on the atom. In the reference frame of the atom, the frequencies of the two beams are shifted due to the Doppler effect: $\omega_{\pm}(v) = \omega_L (1 \pm \frac{v}{c})$, where the $+$ sign refers to the laser towards which the atom is moving. If ω_L is slightly lower than ω_a , the laser beams are said to be red-detuned, and the absorption probability is greatest for the beam the atom is moving towards.

For weak to moderate laser intensities, spontaneous decay from the excited state will dominate over stimulated emission. The spontaneous decay is directionally symmetric and the averaged momentum recoil in the emission process

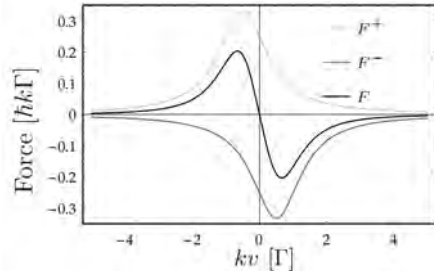


Figure 2.5: (From [71]) The force contributions from the two counter-propagating beams and their sum in the one dimensional Doppler cooling model. A laser detuning $\Delta = \Gamma/2$ was chosen for these graphs.

will therefore be zero. The absorption, however, imparts a directional momentum transfer away from the laser source. Together with the Doppler shift and red-detuned laser sources, this results in a friction force, decelerating the atom.

Denoting the resonant absorption cross section $\sigma(\omega_a)$, the laser detuning $\Delta = \omega_a - \omega_L$ and the spontaneous decay rate of the excited state Γ , the saturation intensity is defined as

$$I_{\text{sat}} = \frac{\hbar\omega_a}{\sigma(\omega_a)} \frac{\Gamma}{2} \quad (2.10)$$

and the net force on the atom with two equally intense counter-propagating beams can be found to be

$$F = \hbar k \frac{\Gamma}{2} \frac{I}{I_{\text{sat}}} \left(\frac{\left(\frac{\Gamma}{2}\right)^2}{\left(\frac{\Gamma}{2}\right)^2 + (\Delta + kv)^2} - \frac{\left(\frac{\Gamma}{2}\right)^2}{\left(\frac{\Gamma}{2}\right)^2 + (\Delta - kv)^2} \right) \quad (2.11)$$

An example plot of the force contribution of each beam is shown in figure 2.5 along with the sum, the net force. Making a linear approximation $F(v) = -\alpha v$ around $v = 0$ yields the effective friction coefficient α . α as a function of detuning Δ will exhibit a maximum at $\frac{\Gamma}{2}$ in the unsaturated case we have considered here. If transition saturation is taken into account, the maximum of $\alpha(\Delta)$ will gradually shift towards larger values of red-detuning.

The principle can be extended to three dimensions. It is, however, in general not necessary to provide 6 laser beams for Doppler cooling in three dimensions. If the atoms reside in a trapping potential, a single cooling beam can be sufficient, as long as it is not propagating along any of the three main axes of the

trap, or as long as there is significant coupling between the motional degrees of freedom. In an ensemble of ions, the Coulomb interaction between the ions will provide such a strong motional coupling.

The final temperature achievable with Doppler laser cooling is determined by the random momentum kicks of the spontaneous emission process. Although these will average to zero, they can for short times be modelled as a random walk in momentum space. From this random walk, the Doppler limit temperature can be found to be

$$T_D = \frac{\hbar \Gamma}{k_B 2} \quad (2.12)$$

Applicability of Doppler laser cooling to real atoms is crucially dependent on the ability to rapidly cycle on the Doppler cooling transition, which in turn relies on the transition being closed. A transition is called closed if the ground state is the only electronic state the atom may decay to from the excited state. For most atoms and ions, there are no naturally closed transitions available from the electronic ground state. For some of those species a so-called repumping laser can be applied to effectively reduce the level scheme to two levels, forming a closed transition. An important added benefit to using Doppler laser cooling is that the emitted fluorescence light can be imaged onto a CCD camera and used to monitor the positions of the ions. The two Doppler cooled ionic species Ca^+ and Mg^+ involved in the work presented in this thesis will now be covered as examples.

Doppler cooling of Mg^+

The Mg^+ ion (figure 2.6a) is one of the atomic species that do exhibit a naturally closed transition from the ground state. Since Mg resides in the second group of the periodic table, Mg^+ has one valence electron. The ground state configuration is $3s$ and the first excited state configuration is $3p$. Thus, the dipole allowed $3s \leftrightarrow 3p$ transition is closed. The Doppler cooling is carried out on the $3s^2S_{1/2} \leftrightarrow 3p^2P_{3/2}$ transition at 279.6 nm.

Doppler cooling of Ca^+

Although Ca^+ (figure 2.6b) also has one valence electron, it differs from Mg^+ in that the ground state is $4s$ configuration, the first excited state is $3d$ and the second excited state is $4p$. The $s \leftrightarrow d$ transition is not dipole allowed, and as such is not a good candidate for Doppler laser cooling. Instead, one can Doppler cool on the $s \leftrightarrow p$ transition and avoid shelving atoms into the metastable d

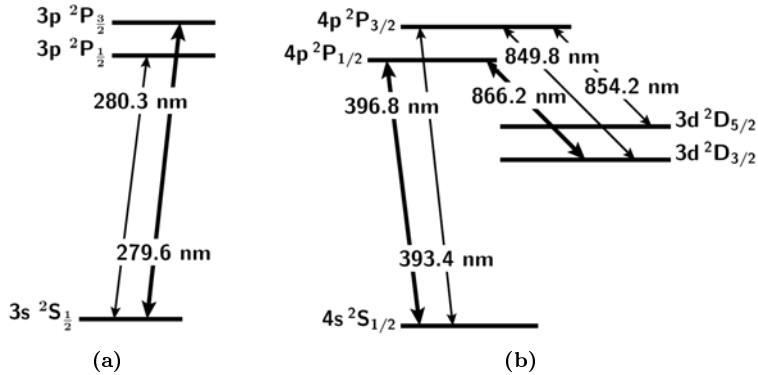


Figure 2.6: (From [46]) Reduced energy level diagrams of Mg^+ and Ca^+ . (a): Mg^+ ions are Doppler cooled on the $3s\ ^2S_{1/2} \leftrightarrow 3p\ ^2P_{3/2}$ transition, which is naturally closed. (b): Ca^+ ions are Doppler cooled on the $4s\ ^2S_{1/2} \leftrightarrow 4p\ ^2P_{1/2}$ transition. A repumping laser is required to drive the $3d\ ^2D_{3/2} \leftrightarrow 4p\ ^2P_{1/2}$ transition to avoid shelving of atoms in the metastable $3d\ ^2D_{3/2}$ state.

state by applying an extra laser driving the $d \leftrightarrow p$ transition. From the p state, the rate of decay into the s state is about 13 times that into the d state. This fact combined with the lower momentum of the photons of the $d \leftrightarrow p$ transition means the cooling effect is dominated by the detuning of the $s \leftrightarrow p$ laser rather than the $d \leftrightarrow p$ laser. The $4s\ ^2S_{1/2} \leftrightarrow 4p\ ^2P_{1/2}$ transition at 396.8 nm is chosen for Doppler cooling, while the repumping transition is $3d\ ^2D_{3/2} \leftrightarrow 4p\ ^2P_{1/2}$ at 866.2 nm.

While the above two transitions are enough to carry out Doppler laser cooling on Ca^+ , some Ca^+ ions will occasionally shelve in the dark $3d\ ^2D_{5/2}$ state due to either collisions with background gas or a forbidden decay transition from the P state. The decay time of the metastable state is about one second and thus can disrupt some kinds of experiments, especially single ion experiments. As long as the shelved ions remain sympathetically cooled by other non-shelved ions they will remain cold, but if only a single Ca^+ ion is trapped, such a shelving event may lead to heating that will take the ion into a trajectory outside the main intensity region of the cooling beams, potentially losing the ion from the trap in the worst case scenario. To prevent this, another laser can be added on the $3d\ ^2D_{5/2} \leftrightarrow 4p\ ^2P_{3/2}$ transition, at 854.2 nm.

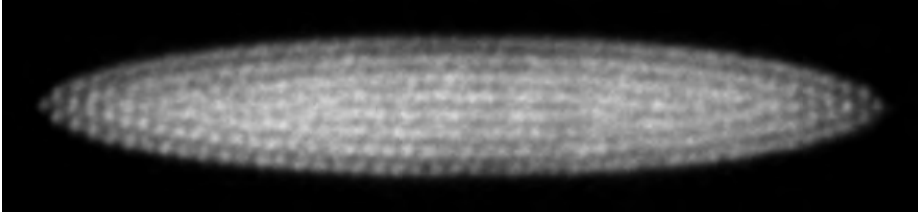


Figure 2.7: A typical experimental image of a Mg^+ Coulomb crystal with ~ 1000 ions. The image is a 2D fluorescence projection of the cylindrically symmetric 3D structure formed by the ions. The symmetry axis is horizontal in the image.

2.1.4 Ion Coulomb crystals

In section 2.1.2, the trapping potential was derived in the absence of any space charges. However, as soon as one starts to load ions into the trap, the ions will repel each other due to their charge. Once the temperature of a Doppler cooled cloud of ions (e.g., Mg^+ or Ca^+) passes below the so-called Coulomb crystallization threshold, the Coulomb interaction energy exceeds the kinetic energy and the ions assume a rigidly ordered spheroidal structure known as a Coulomb crystal where each ion is localized to within a cubic micron. An experimental image of such a crystal in the room temperature trap is shown in figure 2.7. With the typically applied detuning and cooling intensity, the temperature reached for such a crystal is around ~ 10 mK, which is below the threshold for Coulomb crystallization.

In such a crystal, the Coulomb interaction between the ions couples the motional degrees of freedom well enough that even a single axial cooling beam is enough to bring the ions to crystallize. In practice, a net cooling force of zero on the ions is often preferred, which is accomplished by using two equally intense counterpropagating axial beams.

When working with a single ion, no coupling is present between the motional degrees of freedom and a radial beam is necessary for cooling the radial degree of freedom of the ion. The same is true when working with an axial string of ions, which can be created by having $\omega_r \gg \omega_z$, typically achieved by having high U_{rf} and low U_{end} .

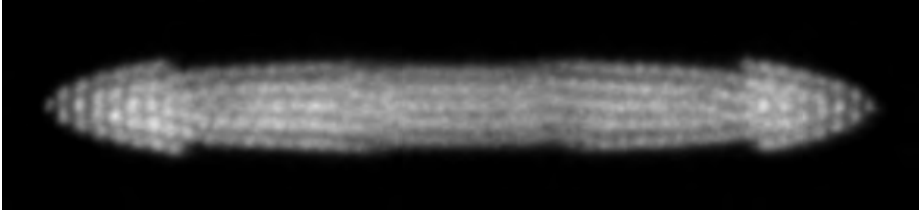


Figure 2.8: A typical experimental image of a Coulomb bicrystal containing ~ 500 fluorescing Mg^+ ions and ~ 500 non-fluorescing MgH^+ ions. The outer boundary of the crystal is indicated by the dashed ellipse, and the radial segregation of the two species is evident in that the MgH^+ occupies the volume at higher radial distance.

Multi-component Coulomb crystals

Besides coupling the motional degrees of freedom of the individual ion, the Coulomb interaction also couples the motion of all the different ions in the ensemble. This enables cold multi-species Coulomb crystals even though only one species is actively Doppler laser cooled. The laser cooled species thus functions as a cold heat sink for the other species and allows crystallization of the entire ensemble. This principle is known as sympathetic cooling and is used in the experiments in this thesis to cool the translational degrees of freedom of molecular ions formed in reactions between Ca^+ or Mg^+ and various neutral molecules.

Taking a look at equations 2.7, 2.8 and 2.9, we notice that the potential energy in the axial direction is independent of mass. This is not the case for the radial direction, since the radial trap frequency is not inversely proportional to M . The radial potential is thus more tightly confining for lower mass to charge ratios, leading to radial segregation of ion species with different mass to charge ratios. By choosing suitable trapping parameters, a Paul trap can be made confining for all Mg^+ and Ca^+ isotopes as well as molecules such as MgH^+ , CaH^+ and CaD^+ (masses ranging from 24 amu to 50 amu) simultaneously, if need be. The efficiency of the sympathetic cooling scheme is, however, highest when the cooled and uncooled species have the same charge to mass ratio and declines as the difference in charge to mass ratio becomes higher. An image of a two-component crystal where only the lighter component fluoresces due to Doppler laser cooling can be seen in figure 2.8.

Micromotion

Whenever ions are located off-axis, they experience the oscillation of the rf potential, the micromotion apparent in equation 2.5 as the term $\frac{q}{2} \cos(\omega_{\text{rf}}t)$. Equation 2.5 was derived for a particle experiencing only the trap potential and no space charges, which is only a valid model if the trap contains only a single ion. In a Coulomb crystal, however, while the secular motion is cooled down by Doppler cooling, the time averaged position of the individual ion remains fixed off-axis because of the rigid structure of the crystal. The position amplitude A_{pos} of the micromotion performed by the ion is then given as

$$A_{\text{pos}} = \frac{q}{2}r \quad (2.13)$$

where r is the distance from the rf-free trap center axis. The velocity amplitude A_{vel} in this oscillation is then

$$A_{\text{vel}} = \frac{\omega_{\text{rf}}q}{2}r \quad (2.14)$$

2.1.5 Single ion mass measurement (SCSI-MS)

In multi-species ion trap experiments it is often necessary to identify the non-fluorescent species. Most commonly, the identity is inferred from the mass of the ion. Various techniques exist for mass measurement, including quadrupole mass filtering, time-of-flight measurement and Fourier Transform Ion Cyclotron Resonance mass spectrometry. The method used in the Ion Trap Group for single ion mass measurement is called the Sympathetically Cooled Single Ion Mass Spectrometry (SCSI-MS) technique.

In the SCSI-MS technique, a single non-fluorescing ion of interest is held sympathetically cooled by a single fluorescing, Doppler cooled ion, for example Mg^+ or Ca^+ . Trapping voltages are chosen such that $\omega_r > \omega_z$, so that the two ions will form a string on the center axis of the trap. The presence of the non-fluorescing ion can be inferred from fluorescence images from the displacement of the fluorescing ion from the center of the trap, as indicated in figure 2.9a.

The mass measurement is based on measurement of the resonant excitation frequency of one of the two axial oscillatory modes of this trapped and crystalized linear two-ion system. These two modes are referred to as the common mode and the breathing mode. In the common mode, the ions move in phase with each other, while the ions move out of phase in the breathing mode.

To measure either of these frequencies, a function generator is hooked up to provide a sine wave modulation on a set of endcap electrodes as an addition to

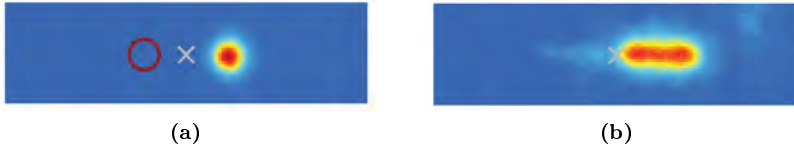


Figure 2.9: (a): One fluorescing Doppler cooled Ca^+ ion next to a non-fluorescing CaH^+ ion. The position of the trap center is marked with the gray cross, and the position of the CaH^+ ion is indicated with the red circle. (b): The same two ions undergoing the SCSI-MS measurement. The axial resonance is excited, resulting in a smearing out of the fluorescence signature of the Ca^+ ion.

the previously introduced trapping voltages. By sweeping the frequency of the modulation and observing the fluorescence signature of the ions with a CCD camera, an excitation of an axial mode will be apparent as a characteristic smearing out of the fluorescence, since the exposure time of the CCD camera (typically hundreds of milliseconds) is much larger than the oscillation period (typically $\sim 10 \mu\text{s}$). Such a smearing is shown in figure 2.9b. If the driving modulation is kept weak enough that simple driven harmonic motion remains a good model for the oscillation, the resonance frequency is then simply the frequency at which maximum amplitude is obtained.

Equation 2.8 tells us the axial angular resonance frequency of a single ion resting by itself in the trapping potential. It can be shown [72] that the two resonance frequencies for a two-ion system are

$$\nu_{\pm}^2 = \left(1 + \frac{1}{\mu} \mp \sqrt{1 - \frac{1}{\mu} + \frac{1}{\mu^2}} \right) \nu_1^2 \quad (2.15)$$

where ν_1 is the resonance frequency for a single ion of mass m_1 and $\mu = \frac{m_2}{m_1}$. ν_+ corresponds to the common mode frequency, while ν_- is the breathing mode frequency. It follows that if two ions of equal mass are co-trapped, the common mode resonance frequency will be the same as for a single ion of that mass. For the experiments in this thesis, only measurement of the common mode motion is used.

2.2 Experimental implementations

The theory of the various ion techniques has now been introduced, and I will now cover the experimental equipment and implementations we have used throughout the studies in this thesis.

2.2.1 The room temperature vacuum chamber and attachments

Figure 2.10 shows a picture of the vacuum chamber seen from the outside, and figure 2.11 shows a picture of the contents. A typical base pressure of $\sim 4 \times 10^{-10}$ mbar is maintained by a Leybold IZ 270 triode ion getter pump located beneath the chamber table. The chamber pressure is monitored with an AML UHV Bayard-Alpert ion gauge or, alternatively, with a PC controlled Spectra Satellite LM502 rest gas analyzer with a mass range from 1 to 100 amu and a resolution of 1 amu. Gas can be leaked into the chamber via a leak valve located beneath the table. Together with the ion gauge, the leak valve allows us to control the pressure of the leaked-in gas with a precision better than 1×10^{-10} mbar. Two small gas containers in front of the leak valve with capacitive pressure gauges attached are used as temporary reservoirs for gas and also enable us to prepare mixtures of gasses, such as the H_2/HD mixtures used in chapter 8.

2.2.2 Trap parameters

A picture of our ion trap can be seen in figure 2.12. The dimensions of the trap are chosen such that we achieve a nearly perfectly quadrupolar radiofrequency field radially and a near-harmonic axial potential over a few millimeters [64]. The parameters are as follows: $r_0 = 3.50$ mm, $z_0 = 2.70$ mm, $z_{\text{endcap}} = 20.00$ mm and $R = 4.00$ mm. Numerical simulations show that these choices of ion trap dimensions result in $\eta = 0.248$. The peak-to-peak radiofrequency voltage amplitude, U_{rf} , is typically a few hundred volts and is coupled resonantly onto the ion trap electrodes at an angular frequency $\omega_{\text{rf}} = 2\pi \times 3.89$ MHz. Together with a typical endcap voltage of about 1 V, a potential well with a depth of ~ 1 eV is created. 1 eV corresponds to about 11 600 K, and so is much higher than the thermal energy of the cooled ions and the thermal energy of the background gas. If the experiment involves exothermic chemical reactions that release more than an electron volt of kinetic energy when they take place, the trapping voltages

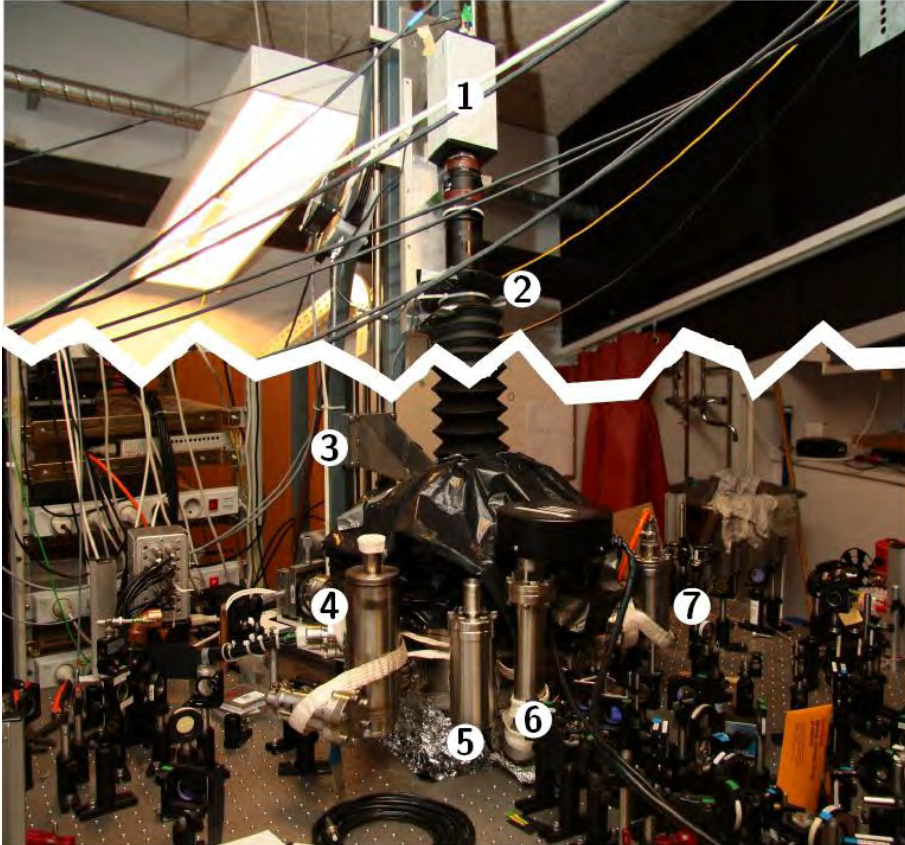


Figure 2.10: (From [46]) Picture of the vacuum chamber as seen from the outside. Seen in this picture is (1) the CCD camera to monitor the fluorescence from the laser cooled ions via (3) a lens system and (2) an image intensifier through a window in a top flange of the vacuum chamber. The distance between the lens system and the image intensifier is ~ 1.5 m. Also seen is (4) a liquid nitrogen container, (5) the electron gun, (6) the rest gas analyzer and (7) the ion gauge. Beneath the table is a leak valve controlled inlet for the admission of various gasses into the ion trap region.

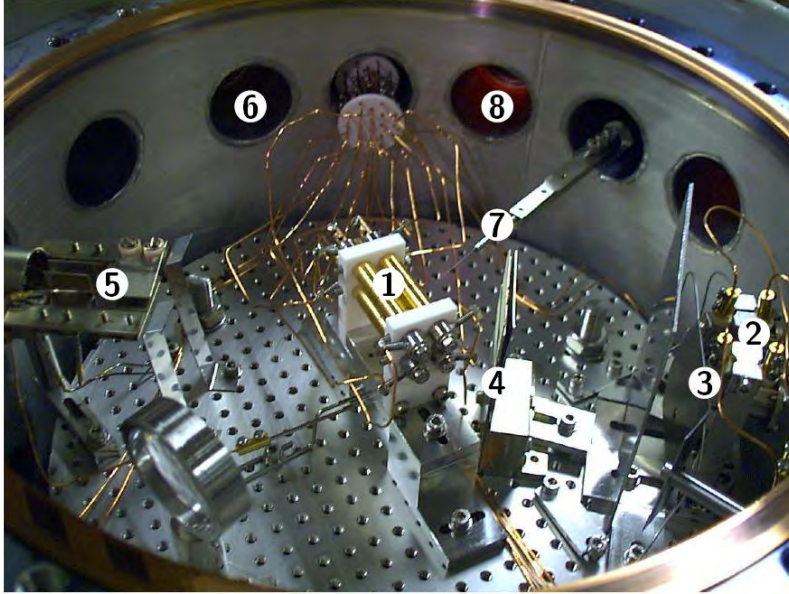


Figure 2.11: (From [64]) Picture of the inside of the cylindrical vacuum chamber used in the room temperature environment experiments. The inner diameter of the chamber is 30 cm. Essential components inside the chamber are marked by numbers. (1) The linear RF ion trap. (2) The magnesium and calcium ovens, which are the sources for the atomic beams passing through the center of the ion trap. (3) A shutter to block or unblock the atomic beams from the ovens. (4) Skimmer plates, used to collimate the effusive beams from the ovens in order to avoid contamination of the ion trap electrodes. (5) An electron gun including deflection plates installed to make an electron beam cross the atomic beams in the center of the ion trap for ion production. This was not used for any of the experiments in this thesis. (6) One of two sets of opposing window openings for sending in laser beams along the main ion trap axis (the z -axis) and along the horizontal radial direction, perpendicular to the z -axis. (7) A piece of optical fiber with a diameter of $125\ \mu\text{m}$, which can be translated into the ion trap center for tests and magnification calibration of the imaging system for the fluorescence of the laser cooled ions. (8) One of two opposed window openings that permit laser beams to cross the atomic beams nearly at right angles in the ion trap center for producing ions by photoionization.

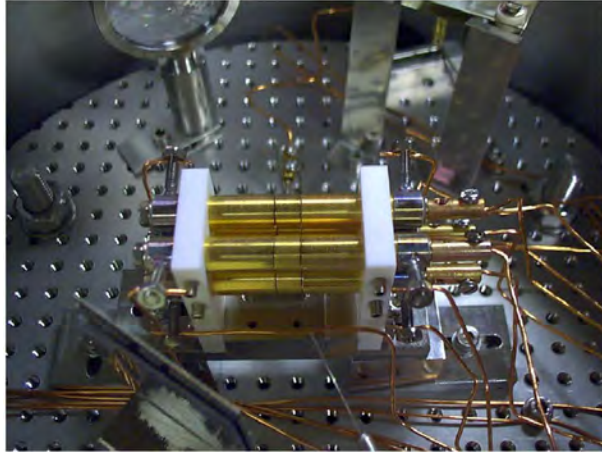


Figure 2.12: (From [64]) Picture of the ion trap in the room temperature chamber. As a scale, the center part of the electrode structure ($2z_0$) is 5.4 mm long.

can be increased to provide trap depths above 50 eV. The storage time of the ions can thus be hours or more at a typical vacuum in the 10^{-10} mbar range.

2.2.3 Laser systems

In the Ion Trap Group, a variety of laser systems have been set up to facilitate the schemes necessary to manipulate ions in ion traps. These include continuous wave (cw) lasers and pulsed, Q-switched lasers producing pulses of nanosecond duration. In the following, I will describe each of the laser systems in turn.

Mg⁺ Doppler cooling laser system

To Doppler cool Mg⁺ ions, coherent radiation at 280 nm is necessary. This light is in the Ion Trap Group generated by frequency doubling coherent radiation at 559 nm with a beta barium borate (BBO) crystal in an external resonant cavity constructed by Niels Kjaergaard [64]. We have two options for generating this light, one of which further utilizes frequency doubling of laser light at 1118 nm in another external resonant cavity, this one using a lithium triborate (LBO) crystal. Bachelors student Kåre Bitsch and I carried out the design, construction and testing of this cavity in 2011. This is described in section 3.3.

The original source of the 559 nm light is a Coherent 599 cw dye ring laser, pumped by one of two Ar^+ ion lasers. The Ar^+ lasers lase on several spectral lines, mostly 488 nm and 514 nm. The dye used in the dye laser is pyromethene 556 dissolved in ethylene glycol, which, when pumped with 5 W of Ar^+ pump light, will in locked single mode operation typically produce ~ 600 mW of 559 nm light.

The newer, generally more convenient, alternative for generation of 559 nm light is to frequency double the output of a Menlo Systems fiber laser lasing at 1118 nm. The laser consists of a seeder, pre-amplifier and power amplifier stage and outputs the infrared light through a 1 m fiber. It can deliver infrared powers up to ~ 2 W, which results in up to ~ 1 W of 559 nm light after the lithium triborate (LBO) frequency doubling process. For details see section 3.3.

With a typical 559 nm input to the final doubling cavity of 600 mW, a 280 nm ultraviolet output power of 20 mW is typical. The beam profile of this UV output is not Gaussian due to the so-called critical phase matching scheme applied in the final frequency doubling step, but the majority of the power resides in a smooth central lobe. Smaller lobes in the horizontal directions are cut away from the main lobe with an iris roughly 2 m after the doubling cavity.

Mg photoionization laser system

For photoionization of Mg, coherent radiation at 285 nm is necessary. The system for producing this is almost identical to the original system for the Doppler cooling light. It is generated by using a beta barium borate (BBO) crystal to frequency double 570 nm light originating from a dye laser of the same type as in the Doppler cooling system. This dye laser is in turn pumped with 5 W of Ar^+ ion laser light. The dye used for this system is rhodamine 6G dissolved in ethylene glycol. This dye has a longer life time than the pyromethene used in the Doppler cooling laser system but, as a tradeoff, will deliver less power, typically ~ 300 mW. A typical 285 nm output power is ~ 15 mW.

Ca^+ Doppler cooling laser systems

The transitions that need to be driven when Doppler cooling Ca^+ are at 397 nm and at 866 nm. The 397 nm violet light is created by frequency doubling in a lithium triborate (LBO) crystal the 794 nm output of a Coherent 899 titanium sapphire (Ti:Sa) laser, pumped by a Coherent Verdi V8 Nd:YAG laser at 532 nm. The wavelength of the Ti:Sa laser is locked to a temperature stabilized external reference cavity with the Pound-Drever-Hall locking scheme. At the time of the

Ca^+ experiments in this thesis, the typical 794 nm power was 250 mW and the typical 397 nm power was 20 mW.

The 866 nm laser radiation is produced directly with a home-built diode laser which is also wavelength locked to a temperature stabilized reference cavity with the Pound-Drever-Hall locking scheme.

Similarly, the 854 nm radiation is generated in the same type of home-built diode laser, although this laser was not frequency stabilized during the measurements in this thesis. Since even weak coupling is sufficient to avoid D state shelving, keeping the laser exactly on resonance was not necessary.

Ca photoionization laser system

The 272 nm light required in the Ca photoionization scheme is generated by two steps of frequency doubling in external resonant cavities, starting with a fiber laser operating at 1088 nm. The first doubling step brings the light to 544 nm in a lithium niobate (LN) crystal, and the second step further doubles the frequency in a beta barium borate (BBO) crystal to achieve the desired wavelength, 272 nm. I carried out the construction and characterization of the second doubling cavity in 2009. This work is covered in section 3.2.

Wavelength meter

A HighFinesse WS-U wavelength meter was installed in the Ion Trap Group in 2011 which enabled more convenient measurement and slow locking of the wavelengths of various laser systems. For the experiments in this thesis, the wavelength meter was used to lock the Mg^+ Doppler cooling dye laser, the Mg^+ Doppler cooling fiber laser and the Mg photoionization dye laser. The wavelength range of the WS-U is 400 to 1000 nm, so direct measurement of the ultraviolet radiation is not possible. We choose instead to measure the wavelength before the final doubling step, where the wavelengths are 559 nm and 570 nm. The wavelength meter has integrated PID locking software and feeds back to the Doppler cooling laser (the dye laser or the fiber laser) and to the photoionization dye laser. The characteristic time scale of the locking is about 500 ms for the fiber laser and about 3 s for the dye lasers.

2.2.4 Fluorescence imaging

As mentioned in 2.1.3, the Doppler laser cooling scheme has the added benefit of providing fluorescence light for monitoring the ions. The light from the ions

is imaged onto an image intensifier with a lens, and the fluorescence from the image intensifier is then again imaged onto a CCD camera with a lens. The magnification of the imaging system is about $4\times$, which is enough to distinguish individual ions in a string under normal trapping conditions.

The presence of non-fluorescing ions can be inferred from their displacement of the fluorescing ions. As part of the rotational cooling experiments, I wrote software in LabVIEW for determination of the amount of non-fluorescing ions in a bicrystal. This software is introduced in section 5.4.

2.2.5 Formation of MgH^+

Having loaded either a Coulomb crystal or a string of Mg^+ ions into the trap, it is possible to induce a reaction with hydrogen, forming MgH^+ . In the room temperature chamber this is done by introducing H_2 gas as a background gas through a leak valve, increasing the pressure from the usual background of $\sim 4 \times 10^{-10}$ mbar up to typically $\sim 2.0 \times 10^{-9}$ mbar. Introducing H_2 as a background gas was also the reaction method used in early experiments in the cryogenic chamber, but a capillary tube system was later installed to allow targeted delivery of H_2 directly into the trap center. The direct exposure of the capillary tube system allows faster reactions and a lower overall amount of hydrogen let into the chamber.

The reaction $\text{Mg}^+ + \text{H}_2 \rightarrow \text{MgH}^+ + \text{H}$ is not energetically allowed from the Mg^+ ground state, but reactions from the electronically excited $3p\ ^2P_{3/2}$ state used in the Doppler cooling scheme are allowed. The formed molecules remain trapped, since the kinetic energy released in the reaction is well below the typical trapping depths of ~ 1 eV. With a hydrogen background pressure of $\sim 1.5 \times 10^{-9}$ mbar and high Doppler cooling excitation rate, the reaction phase typically lasts ~ 1 min. Immediately after formation, the MgH^+ ions will segregate to the outside of the crystal, forming a two-component crystal or bicrystal. Since the molecular ions do not participate in the Doppler cooling scheme, they will, when looking at ion fluorescence, be visible only as 'dark' ions or as a deviation from the actually still approximately spheroidal overall crystal shape as seen in figure 2.8. Once enough atoms have reacted, the reaction can be stopped by simultaneously stopping the hydrogen leak and detuning the Doppler cooling laser, typically by about 200 MHz, to reduce the population in the excited P state from which the reaction can occur.

Design and construction of two resonant cavities for frequency doubling of laser radiation

Many atomic and molecular electronic transitions that one would like to address with lasers in a laboratory lie in the near ultraviolet part of the electromagnetic spectrum. Since many of the most convenient laser media lase in the visual or near infrared area, one often chooses to utilize frequency mixing techniques to reach the desired ultraviolet wavelengths. Frequency mixing methods are based on nonlinear optical processes such as second harmonic generation (SHG), third harmonic generation, sum frequency generation, difference frequency generation and others. In our laser setups, we make extensive use of SHG, or frequency doubling, of laser sources. As an example, as I will mention in chapter 5, the two laser pulses required for the dissociation detection scheme are formed through the use of several steps of SHG.

The applications of SHG that will be the subjects of this chapter is the production of coherent radiation at 272 nm and at 559 nm. 272 nm light is required for photoionization of Ca atoms [73, 67], while 559 nm light is, after a further doubling step, used for Doppler laser cooling of Mg⁺ ions.

Prior to my arrival to the Ion Trap Group, work was already underway to construct all-solid-state laser systems for production of both of these wavelengths. For the photoionization setup, this was to consist of a 1088 nm fiber laser, a first cavity SHG step to 544 nm light and a second cavity SHG step to 272 nm. The first two components of this new system had already been installed by the time of my arrival. The third step was temporarily taken care of by sharing of an SHG cavity intended for another laser system, that for photoionization of Mg at 285 nm. An article was published in 2007 describing the design and performance of these components [74]. As part of the preparations for working on Ca⁺ ions, I constructed in 2009 the final step of this planned system, an external cavity for doubling of 544 nm light.

The external resonant cavity for frequency doubling of 559 nm into 280 nm light had also been constructed before I arrived in the group. This was done by Niels Kjærgaard and is described in his PhD thesis [64]. The 559 nm light was at the time delivered by a dye laser, which is still operational and can still be used for this purpose today. Recently, it became feasible to employ a solid state laser system for generation of the 559 nm light instead of the dye laser,

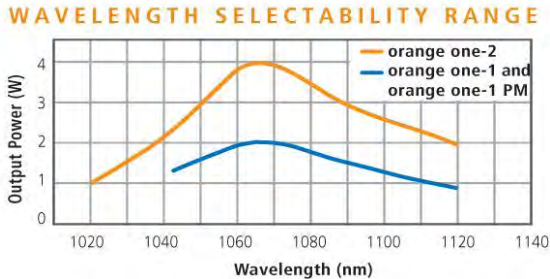


Figure 3.1: From [75], 2012. The Yb-doped fiber lasers 'orange one' can be made with a tuning range of 0.45 nm around a center wavelength which can be specified to a value between 1020 nm and 1121 nm. The laser manufactured for the Ion Trap Group was an 'orange one-2' model with center wavelength 1118.54 nm.

because of the availability of ytterbium doped fiber lasers from Menlo Systems [75]. They call this brand of laser 'orange one', and such a laser was acquired by the Ion Trap Group in 2011. The center wavelength 1118.54 nm, four times the wavelength of the Mg^+ Doppler cooling resonance, was chosen so that two frequency doubling steps would bring the radiation to the resonance. Bachelors student Kåre Bitsch and I carried out the construction of the frequency doubling cavity from 1119 nm to 559 nm immediately after delivery of the laser.

After covering some generally applicable SHG theory, this chapter will concern itself with the theory and implementation of the required features of such external SHG cavities.

3.1 General second harmonic generation theory

The theory of frequency mixing techniques and phase matching is covered in many laser textbooks, such as Chapter 24 of Pedrotti, Pedrotti and Pedrotti's 'Introduction to Optics' [76] and Chapters 17 and 18 of Milonni and Eberly's 'Lasers' [77], so I will in this section only briefly cover the theory behind second harmonic generation.

When an optical medium is exposed to an electric field $\vec{E}(t)$, the induced polarization vector $\vec{P}(t)$ as a function of the applied $\vec{E}(t)$ -field will in general

contain non-linear terms:

$$\vec{\mathcal{P}}(t) = \epsilon_0 \chi^{(1)} \vec{E}(t) + \epsilon_0 \chi^{(2)} \vec{E}^2(t) + \dots \quad (3.1)$$

where the susceptibilities $\chi^{(i)}$ are tensors of rank $i + 1$ connecting the various electric field polarization direction combinations \vec{E}^i with the resulting three components of the dipole polarization $\vec{\mathcal{P}}$ of the medium. If the \vec{E} -field is oscillating at an angular frequency ω , the induced polarization will thus in general contain angular frequency components at multiples of the driving field; 2ω , 3ω and so on, each to a degree determined by the magnitude of the corresponding χ . If the medium is isotropic, $\chi^{(i)} = 0$ for all even i due to inversion symmetry, so amplitudes of all even multiples of frequency must be zero, while this is not the case for anisotropic materials. In such an anisotropic medium, the second order polarization response generates an electric field with angular frequency 2ω called the second harmonic field. The beam at angular frequency ω is referred to as the fundamental beam.

As the fundamental beam propagates through the medium, the components of the generated second harmonic field will in general not be in phase with each other due to chromatic dispersion and will interfere destructively. Only if the chromatic dispersion is by some means compensated for, that is, $n_\omega = n_{2\omega}$, will one be able to generate a strong second harmonic field through constructive interference, and the degree to which the constructive interference is reached is known as phase matching. There are several different methods to accomplish this compensation, including the birefringence dependent critical and non-critical phase matching schemes. In the 272 nm cavity we use critical phase matching in a uniaxial crystal (BBO) and in the 559 nm cavity we use non-critical phase matching in a biaxial crystal (LBO). These two specific schemes are explained in the respective sections later in this chapter. We will only concern ourselves with the case of so-called type I phase matching in which the fundamental beam at angular frequency ω has polarization orthogonal to the second harmonic beam at angular frequency 2ω .

Because SHG depends on the quadratic term in the material polarization as a function of the electric field strength E , the SHG conversion is proportional to E^2 . The conversion efficiency will thus be increased by focusing the fundamental beam through the crystal, rather than letting it pass through as a collimated beam. However, considering a finite length of crystal and the fact that a smaller beam waist necessarily implies a smaller confocal parameter (depth of focus),

the fundamental beam spotsize cannot be made arbitrarily small over the whole length of the crystal. For the Gaussian beams we will consider in this chapter, the confocal parameter of the fundamental beam b and the beam waist w_0 are related by $b = \frac{\omega w_0^2}{c}$, where ω is the angular frequency of the fundamental light. For this reason, there exists an optimal beam waist size that maximizes the generation of the second harmonic light. In the following section, the theory for determining this waist is briefly covered.

3.1.1 Determining the optimal waist

Much of the theoretical framework for parametric interactions in crystals such as the SHG processes we are considering here was developed and published by Boyd and Kleinman in 1968 [78]. To determine what beam waist inside the crystal will correspond to the highest conversion efficiency, one must take into account not only the confocal parameter but also the beam distortion caused by the walk-off phenomenon introduced in the phase matching section of the 272 nm cavity later in this chapter. In addition to this, the optimal phase mismatch $\Delta k = 2k_\omega - k_{2\omega} = \frac{2\omega}{c}(n_\omega - n_{2\omega})$ is not exactly equal to zero for non-collimated beams. For a thorough derivation of the formalism, I urge the reader to consult the article of Boyd and Kleinman.

On the basis of equation 3.1, an effective nonlinear coefficient for a chosen fixed geometry satisfying phase matching is defined by $\mathcal{P} = 2\epsilon_0 d_{\text{eff}} E^2$. Boyd and Kleinman derive in CGS units an expression for the nonlinear power conversion coefficient $\gamma = P_{2\omega}/P_\omega^2$ far from saturation ($P_{2\omega} \ll P_\omega$), which converted to SI units is

$$\gamma = \frac{P_{2\omega}}{P_\omega^2} = d_{\text{eff}}^2 \frac{2\omega^3 L_c}{\pi \epsilon_0 c^4 n_\omega n_{2\omega}} e^{-\alpha' L_c} \times h(\sigma, \beta, \kappa, \xi, \mu) \quad (3.2)$$

with

$$h(\sigma, \beta, \kappa, \xi, \mu) = \frac{1}{4\xi} e^{\mu\alpha L_c} \iint_{-\xi(1-\mu)}^{\xi(1+\mu)} d\tau d\tau' \times \frac{\exp[-\kappa(\tau + \tau') + i\sigma(\tau - \tau') - \beta^2(\tau - \tau')^2]}{(1 + i\tau)(1 - i\tau')}, \quad (3.3)$$

where the symbols are defined as follows: ω still denotes the fundamental angular frequency. The absorption parameters α and α' are defined by the absorption coefficients of the fundamental, α_ω , and the second harmonic, $\alpha_{2\omega}$, as $\alpha = \alpha_\omega - \frac{1}{2}\alpha_{2\omega}$ and $\alpha' = \alpha_\omega + \frac{1}{2}\alpha_{2\omega}$. L_c is the crystal length and $\xi = L_c/b$ is the

dimensionless focusing parameter. The distance from the crystal center to the focus is included through another dimensionless parameter $\mu = (L_c - 2f)/L_c$, where f is the position of the focus relative to the incident surface of the crystal. $\kappa = \frac{1}{2}\alpha b$ is a dimensionless absorption parameter, $\sigma = \frac{1}{2}b\Delta k = b\omega(n_\omega - n_{2\omega})/c$ is a dimensionless phase matching parameter and $\beta = \rho b/(2w_0)$ is a dimensionless double refraction parameter containing the walk-off angle ρ and the waist of the fundamental beam, $w_0 = \sqrt{bc/(\omega n_\omega)}$.

We can take $\alpha_\omega = \alpha_{2\omega} = 0$ for both LBO and BBO crystals at the relevant wavelengths and choose to consider the (optimal) case of putting the focus in the center of the crystal: $f = L_c/2$, $\mu = 0$. Finding the optimal waist is then a matter of evaluating equation 3.3 under these conditions, which will be done numerically for each of the two frequency doubling cases in their respective 'Design' sections.

3.1.2 External resonant cavity theory

Unlike pulsed lasers, the E -field amplitudes of CW laser beams are as a general rule far too low for efficient SHG, even when optimally focused. For this reason the crystal is put inside an external resonant cavity in which light is accumulated and intensified, creating much higher E -field amplitudes and allowing efficient SHG.

Ring (traveling wave) cavities have an important advantage over standing wave cavities in that the SHG light is emitted only in one direction rather than having the SHG power split over the forward and backward direction as would be the case in a standing wave cavity. Bow-tie ring cavities had from past experience in the Ion Trap Group [74] proven quite successful at SHG of CW beams, so it was decided to use the same general design for the 272 nm cavity as the 285 nm cavity (see figure 3.2a) and the same general design for the 559 nm cavity as the 544 nm cavity (see figure 3.2b). The beam path for both these bow-tie cavity designs is such that the fundamental beam enters the cavity through mirror M1, goes through an auxiliary focus between M1 and M2 and reflects off mirror M2 towards M3. M3 is a concave mirror and focuses the beam into the crystal focus inside the nonlinear crystal, located between M3 and M4. M4 is also a concave mirror and sends the beam to M1 and back into the auxiliary focus. To allow the generated second harmonic light to escape the cavity, M4 is a dichroic mirror, coated to be transmitting to the second harmonic light while reflecting the fundamental.

The cavity must additionally be kept resonant with the fundamental light, that is, the light must interfere constructively with itself after a full round trip.

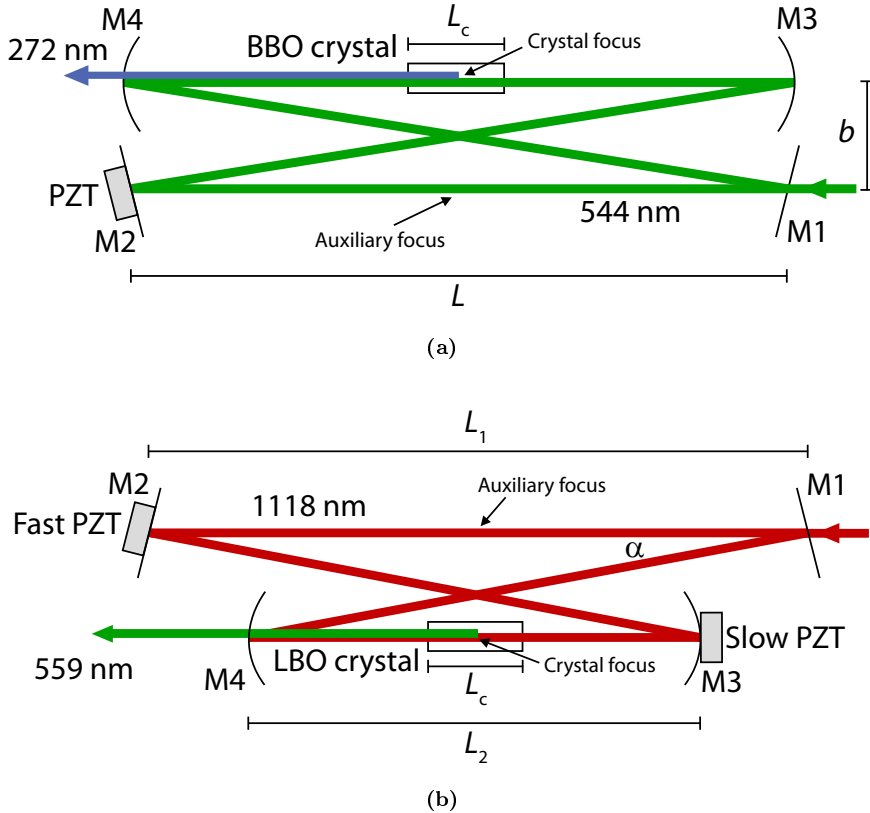


Figure 3.2: Schematic representation of the bow-tie cavity configuration designs used in the Ion Trap Group. **(a):** A design in which the distance between the curved mirrors M3 and M4 is kept equal to the distance between the flat mirrors M1 and M2. This design had previously been used in the Ion Trap Group for the 285 nm and 280 nm cavities and was used for the 272 nm cavity as well. **(b):** In this design the distance between the curved mirrors M3 and M4 is allowed to be different to the distance between the flat mirrors M1 and M2. Previously used for the 544 nm cavity, this design was also chosen for the 559 nm cavity.

This is accomplished if the light obtains a total phase shift of a multiple of 2π over the round trip. This phase shift includes the phase shift of π obtained in each reflection off of a mirror and the Gouy phase shift obtained in the passage of each focus. To keep the cavity resonant with the incoming light, one or two of the mirrors are glued onto a piezoelectric transducer (PZT) that will lengthen or shorten the total cavity path length depending on the voltage applied over it with a precision of a small fraction of a wavelength. By adjusting the voltage, the phase shift of the light can be adjusted to a multiple of 2π , bringing the cavity to resonance and enabling accumulation of light within the cavity.

ABCD matrix analysis

The choice of the dimensions of the cavity must be such that the cavity exhibits a stable mode and such that a focus is formed inside the crystal with the correct waist for this mode. To calculate the stability and waist size of a cavity, it is necessary to use ray transfer matrices, also known as ABCD matrices. In addition to describing the propagation of geometric light rays through an optical system, this analysis also describes how the spotsize of a Gaussian beam behaves in that optical system. A good summary of ABCD matrix analysis was provided by Kogelnik and Li in 1966 [79] with special attention to applications in resonators such as cavities.

In short, each sequence of optical elements is described by a 2×2 matrix, an ABCD matrix $\begin{bmatrix} A & B \\ C & D \end{bmatrix}$, while the Gaussian beam itself is for each distance along the propagation direction described by a complex beam parameter

$$q(z) = z + iz_R \quad (3.4)$$

where z is the distance to the hypothetical focus that would be formed in the absence of any other optical elements, i is the imaginary unit and z_R is the Rayleigh range of the beam. The reciprocal form of the complex beam parameter

$$\frac{1}{q(z)} = \frac{1}{R(z)} - \frac{\lambda_0}{\pi n w(z)^2} i \quad (3.5)$$

in which R is the radius of curvature of the phase front, is also often used. The spotsize of the beam $w(z)$ is the radius at which the intensity is $\frac{1}{e^2}$ of its peak value and can be found easily using the reciprocal form as

$$w(z) = \sqrt{-\frac{\pi n}{\lambda_0} \text{Im} \left(\frac{1}{q(z)} \right)} \quad (3.6)$$

The q value after passage through the sequence of optical elements described by $\begin{bmatrix} A & B \\ C & D \end{bmatrix}$ is given as

$$\begin{bmatrix} q_2 \\ 1 \end{bmatrix} = k \begin{bmatrix} A & B \\ C & D \end{bmatrix} \begin{bmatrix} q_1 \\ 1 \end{bmatrix} \quad (3.7)$$

where k is a normalization constant to satisfy $1 = k(q_1 C + D)$. By multiplication we obtain the two equations

$$q_2 = k(q_1 A + B) \quad \text{and} \quad 1 = k(q_1 C + D) \quad (3.8)$$

where we eliminate k by dividing them with each other, yielding

$$q_2 = \frac{q_1 A + B}{q_1 C + D} \quad (3.9)$$

A very handy feature of this formalism is that the ABCD matrix of a complex system can be calculated by multiplying simple matrices corresponding to each individual element. In my treatment, I will only need three such elements:

1. Propagation a distance d through a medium of constant refractive index such as air or a crystal. Note that this matrix is independent of the magnitude of the refractive index.

$$\begin{bmatrix} 1 & d \\ 0 & 1 \end{bmatrix} \quad (3.10)$$

2. Passage through a lens or reflection off of a curved mirror with focal length f . For a curved mirror, $f = \frac{R}{2}$, where R is its radius of curvature.

$$\begin{bmatrix} 1 & 0 \\ -\frac{1}{f} & 1 \end{bmatrix} \quad (3.11)$$

3. Refraction at a flat interface from a medium of refractive index n_1 into a medium of refractive index n_2 .

$$\begin{bmatrix} 1 & 0 \\ 0 & \frac{n_1}{n_2} \end{bmatrix} \quad (3.12)$$

For both cavity designs, I will calculate the ABCD matrix for a round trip around the cavity with starting point in the auxiliary focus in two steps. For the 3.2a design, I will need the diagonal distance $L_d = \sqrt{L^2 + b^2}$ from M2 to M3 and from M4 to M1. Keep in mind that subsequent ABCD matrices are

always applied by multiplying from the left, as in equation 3.7. The first step propagates the beam from the auxiliary focus into the center of the crystal with matrix M_1 :

$$M_1(L) = \overbrace{\begin{bmatrix} 1 & \frac{L_c}{2} \\ 0 & 1 \end{bmatrix}}^{\text{surf.} \rightarrow \text{cry}} \overbrace{\begin{bmatrix} 1 & 0 \\ 0 & \frac{1}{n} \end{bmatrix}}^{\text{refr.}} \overbrace{\begin{bmatrix} 1 & \frac{L-L_c}{2} \\ 0 & 1 \end{bmatrix}}^{\text{M3} \rightarrow \text{surf.}} \overbrace{\begin{bmatrix} 1 & 0 \\ -\frac{1}{f} & 1 \end{bmatrix}}^{\text{M3 curvature}} \overbrace{\begin{bmatrix} 1 & L_d \\ 0 & 1 \end{bmatrix}}^{\text{M2} \rightarrow \text{M3}} \overbrace{\begin{bmatrix} 1 & \frac{L}{2} \\ 0 & 1 \end{bmatrix}}^{\text{aux} \rightarrow \text{M2}} \quad (3.13)$$

The second step takes us the rest of the way with matrix M_2 , back to the auxiliary focus:

$$M_2(L) = \overbrace{\begin{bmatrix} 1 & \frac{L}{2} \\ 0 & 1 \end{bmatrix}}^{\text{M1} \rightarrow \text{aux}} \overbrace{\begin{bmatrix} 1 & L_d \\ 0 & 1 \end{bmatrix}}^{\text{M4} \rightarrow \text{M1}} \overbrace{\begin{bmatrix} 1 & 0 \\ -\frac{1}{f} & 1 \end{bmatrix}}^{\text{M4 curvature}} \overbrace{\begin{bmatrix} 1 & \frac{L-L_c}{2} \\ 0 & 1 \end{bmatrix}}^{\text{surf} \rightarrow \text{M4}} \overbrace{\begin{bmatrix} 1 & 0 \\ 0 & \frac{n}{1} \end{bmatrix}}^{\text{refr.}} \overbrace{\begin{bmatrix} 1 & \frac{L_c}{2} \\ 0 & 1 \end{bmatrix}}^{\text{cry} \rightarrow \text{surf}} \quad (3.14)$$

The matrix $M = \begin{bmatrix} A & B \\ C & D \end{bmatrix}$ for a full round trip is then

$$M(L) = M_2(L)M_1(L) \quad (3.15)$$

For the 3.2a design, the calculation of the ABCD matrix is done in much the same way, except that the distance between the flat mirrors M1 and M2 is denoted L_1 , the distance between the curved mirrors M3 and M4 is denoted L_2 and the folding angle of the cavity is quantified not in terms of a sideways displacement b of the mirrors but in terms of the folding angle α , as illustrated in figure 3.2b. The diagonal distance between M2 and M3 or M4 and M1 is then $L_d = \frac{L_1+L_2}{2\cos(\alpha)}$. Again starting from the auxiliary focus, we write down the matrix for half a round trip:

$$M_1(L_1, L_2) = \overbrace{\begin{bmatrix} 1 & \frac{L_c}{2} \\ 0 & 1 \end{bmatrix}}^{\text{surf} \rightarrow \text{cry}} \overbrace{\begin{bmatrix} 1 & 0 \\ 0 & \frac{1}{n} \end{bmatrix}}^{\text{refr.}} \overbrace{\begin{bmatrix} 1 & \frac{L_2-L_c}{2} \\ 0 & 1 \end{bmatrix}}^{\text{M3} \rightarrow \text{surf.}} \overbrace{\begin{bmatrix} 1 & 0 \\ -\frac{1}{f} & 1 \end{bmatrix}}^{\text{M3 curvature}} \overbrace{\begin{bmatrix} 1 & L_d \\ 0 & 1 \end{bmatrix}}^{\text{M2} \rightarrow \text{M3}} \overbrace{\begin{bmatrix} 1 & \frac{L_1}{2} \\ 0 & 1 \end{bmatrix}}^{\text{aux} \rightarrow \text{M2}} \quad (3.16)$$

And the second matrix represents the trip back again to the auxiliary focus:

$$M_2(L_1, L_2) = \overbrace{\begin{bmatrix} 1 & \frac{L_1}{2} \\ 0 & 1 \end{bmatrix}}^{\text{M1} \rightarrow \text{aux}} \overbrace{\begin{bmatrix} 1 & L_d \\ 0 & 1 \end{bmatrix}}^{\text{M4} \rightarrow \text{M1}} \overbrace{\begin{bmatrix} 1 & 0 \\ -\frac{1}{f} & 1 \end{bmatrix}}^{\text{M4 curvature}} \overbrace{\begin{bmatrix} 1 & \frac{L_2-L_c}{2} \\ 0 & 1 \end{bmatrix}}^{\text{surf} \rightarrow \text{M4}} \overbrace{\begin{bmatrix} 1 & 0 \\ 0 & \frac{n}{1} \end{bmatrix}}^{\text{refr.}} \overbrace{\begin{bmatrix} 1 & \frac{L_c}{2} \\ 0 & 1 \end{bmatrix}}^{\text{cry} \rightarrow \text{surf}} \quad (3.17)$$

The full round trip matrix is then

$$M(L_1, L_2) = M_2(L_1, L_2)M_1(L_1, L_2) \quad (3.18)$$

A stable Gaussian mode in the cavity satisfies the criterium that it reproduces itself after a full round trip. That is, if the beam starts in a focus halfway between M1 and M2 with a waist $w_{0,a}$, then the beam must be reproduce the same focus with the same waist after a round trip. This means we set $q_1 = q_2 = q_a$ in equation 3.9, so the full round trip matrix $M = \begin{bmatrix} A & B \\ C & D \end{bmatrix}$ must then satisfy

$$q_a = \frac{q_a A + B}{q_a C + D} \quad (3.19)$$

which is a quadratic equation,

$$Cq_a^2 + (D - A)q_a - B = 0 \quad (3.20)$$

Since the beam forms a focus halfway between M1 and M2 ($z = 0$ in the complex beam parameter), q_a must be purely imaginary, which together with equation 3.20 implies $D = A$. In the two cavity design cases considered here, however, this condition is always fulfilled due to symmetry. For the beam to form a stable mode in the cavity we then have

$$q_a^2 = \frac{B}{C} \quad (3.21)$$

We insert $q_a = z_{R,a}i = \frac{\pi n w_{0,a}^2}{\lambda_0} i$ with $n = 1$ and get

$$w_{0,a} = \sqrt[4]{-\frac{\lambda_0^2 B}{\pi^2 C}} \quad (3.22)$$

If B and C have the same sign, the content of the root is negative and no stable mode exists within the cavity. In our cases, where $A = D$, this condition is identical to the more general resonator stability condition $-1 < \frac{1}{2}(A + D) < 1$, considering the fact that all ABCD matrices have unity determinant ($AD - BC = 1$).

To calculate the crystal waist in the cavity one can simply apply the half round trip matrix $M_1 = \begin{bmatrix} A_1 & B_1 \\ C_1 & D_1 \end{bmatrix}$ to q_a to obtain the complex beam parameter in the center of the crystal, q_c :

$$q_c = \frac{q_a A_1 + B_1}{q_a C_1 + D_1} \quad (3.23)$$

The crystal waist is then

$$w_{0,c} = \sqrt{\frac{q_a \lambda_0}{i \pi n}} \quad (3.24)$$

Using ABCD matrix analysis it is thus possible to find cavity dimensions that will exhibit a stable Gaussian resonant mode with the crystal waist that best matches the optimum determined through the application of the Boyd and Kleinman theory. These calculations will be performed for each of the two doubling cavities in their respective sections.

Impedance matching

Impedance matching for an optical cavity such as the ones we are considering concerns the degree to which the reflection off M1 of the input beam from the outside interferes destructively with the transmission through M1 from the inside of the cavity. When the cavity is resonant, these two contributions to the electromagnetic field are out of phase and, if the M1 reflectivity is chosen correctly, the amplitudes are exactly equal and the input beam will experience no reflection at M1 and the intracavity beam will experience 100 % reflection at M1.

Denoting the reflectivity of the M1 input coupler R_1 and introducing a reflectance parameter R_m as the sum of all other losses in the cavity, linear and non-linear, it can be shown [80] that the ratio of the power of the reflected input light P_r to the power of the input light P_1 is given by

$$\frac{P_r}{P_1} = \left(\frac{\sqrt{R_1} - \sqrt{R_m}}{1 - \sqrt{R_1 R_m}} \right)^2 \quad (3.25)$$

From this equation, it is clear that the reflection goes to zero exactly when $R_1 = R_m$. If this is the case, the cavity is said to be impedance matched and the intracavity power is maximized with regards to input coupler reflectivity.

We can write up an expression for R_m that includes the linear and nonlinear losses in one round trip of the cavity. We denote the reflectivities of the mirrors M2, M3 and M4 R_2 , R_3 and R_4 , respectively, and we denote the transmission of the crystal T_C , where reflections at the anti-reflex coated surfaces are included. The relative loss of power of the fundamental beam due to SHG is proportional to the intracavity power P_c (equation 3.2), so we obtain

$$R_m = R_2 R_3 R_4 T_C (1 - \gamma P_c) \quad (3.26)$$

$$= (1 - \epsilon)(1 - \gamma P_c), \quad (3.27)$$

where $\epsilon = 1 - R_2 R_3 R_4 T_C$ has been introduced as a coefficient including all linear losses.

Equation 3.2 is only valid if the depletion of the fundamental beam is negligible in the passage through the crystal, which is still a good approximation even in the cavity enhanced case. For typical intracavity powers, the depletion per pass γP_c is still on the order of one percent. It is the fact that many passes are made by each photon that enables a high conversion efficiency for the cavity system as a whole.

At perfect impedance matching and for a cavity on resonance, the ratio of intracavity power P_c to power incident on the cavity P_i is given [80] as

$$\frac{P_c}{P_i} = \frac{1}{1 - R_m} \quad (3.28)$$

Inserting the expression for R_m and solving for P_c yields

$$P_c = \frac{-\epsilon + \sqrt{\epsilon^2 + 4(1 - \epsilon)\gamma P_i}}{2(1 - \epsilon)\gamma} \quad (3.29)$$

The impedance matched input coupler transmission is then

$$T_1 = 1 - R_m = \epsilon + (1 - \epsilon)\gamma P_c = \frac{1}{2}(\epsilon + \sqrt{\epsilon^2 + 4(1 - \epsilon)\gamma P_i}) \quad (3.30)$$

3.2 272 nm second harmonic generation cavity

The frequency doubling cavity we have called the 272 nm cavity is the cavity in which input light at 544 nm undergoes SHG to form 272 nm light. In the following sections, I will walk through the design considerations, the construction process and the characterization of the cavity.

3.2.1 Design

In the frequency doubling cavity constructed for doubling of 544 nm light, a BBO (beta barium borate, $\beta - \text{BaB}_2\text{O}_4$) crystal was chosen in a critical phase matching scheme. BBO is a negative uniaxial crystal with a broad type I phase matchable SHG range for fundamental wavelengths from 410 nm to 3300 nm and broad transmission range from 190 nm to 3300 nm [81]. The SHG nonlinear coefficient is high among nonlinear crystals ($d_{\text{eff}} = \frac{1}{2}\chi^{(2)} = 1.78 \text{ pm V}^{-1}$ for our application) and the laser damage threshold is also high. The crystal is mildly hygroscopic and thus care must be taken to keep the crystal in a dry environment, e.g., by keeping a dry air flow over it.

Satisfying the critical phase matching condition in the uniaxial BBO crystal

In a uniaxial crystal such as BBO, one crystallographic axis is different to the two others, which in turn are identical to each other. The unique axis is called the optic axis. A ray of light propagating through such a crystal will in general split into two rays. The polarization component that is linear and perpendicular to the plane spanned by the optic axis and the propagation direction is called the ordinary ray and the polarization component that is parallel to the plane is called the extraordinary ray. While the ordinary ray experiences a refractive index independent of propagation direction, the refractive index for the extraordinary ray depends on the angle θ to the optic axis through

$$\frac{1}{n_e^2(\theta)} = \frac{\cos^2(\theta)}{n_o^2} + \frac{\sin^2(\theta)}{n_e^2} \quad (3.31)$$

where n_e is the refractive index for a beam polarized parallel to the optic axis.

Values for n_o and n_e can be found from the Sellmeier equations provided in reference [82]:

$$n_e^2 = 2.3753 + \frac{0.01224}{\lambda_0^2 - 0.01667} - 0.01516\lambda_0^2 \quad (3.32)$$

$$n_o^2 = 2.7359 + \frac{0.01878}{\lambda_0^2 - 0.01822} - 0.01354\lambda_0^2 \quad (3.33)$$

in which λ_0 is the vacuum wavelength in micrometers.

When the propagation is not parallel to a crystal symmetry axis, one must accept the presence of the walk-off phenomenon, the fact that the \vec{k} vector and the Poynting vector that defines the energy transfer direction of the beam are non-parallel for light of extraordinary polarization inside the medium. This means that while the light of extraordinary polarization 'walks off' to the side at an angle ρ to the \vec{k} vector, the ordinary polarized light does not, causing internal interference structure and astigmatism in the generated second harmonic beam. By symmetry, $\rho = 0$ for propagation along the optic axis and perpendicular to the optic axis. The walk-off angle can be calculated as [83]

$$\rho(\theta) = -\frac{1}{n_e(\theta)} \frac{\partial n_e(\theta)}{\partial \theta} \quad (3.34)$$

and is an important parameter to take into consideration when determining the optimal crystal waist for SHG.

Calculation of the extraordinary and ordinary refractive indices and the walk-off angle as a function of the angle to the optic axis are presented for a fundamental wavelength of 544 nm in BBO in figure 3.3. The phase matching condition is satisfied at $\theta = 46.1^\circ$ in the intersection between the 544 nm ordinary ray line and the 272 nm extraordinary ray curve where $n = 1.673$ for both beams. At this point, the resulting walk-off angle for the SHG light is $\rho = 85.2$ mrad.

Calculating the optimal crystal waist

With this knowledge of the refractive index and the walk-off angle, the Boyd and Kleinman theory can be applied to determine the optimal crystal waist. For different values of ξ and σ , equation 3.3 is evaluated and plotted in figure 3.4.

For each value of ξ , we can choose to consider only the optimal phase matching parameter σ . This optimization with regards to σ is done experimentally by fine tuning the angle of the crystal and is a much faster adjustment than changing the crystal waist. I will follow the notation of Boyd and Kleinman and denote the optimal σ for each ξ as σ_m . I write $h_m(w_0) = h(\sigma_m, \xi)$, where the crystal waist $w_0 = \sqrt{L_c c / (\xi \omega n_\omega)}$. h_m is thus the σ -optimized value of h , expressed as a function of crystal waist rather than ξ .

I plot this in figure 3.5 along with $\gamma_m(w_0)$ from equation 3.2, the optimal input coupler transmission $T_{\text{opt},m}(w_0)$ from equation 3.30, the resulting impedance matched intracavity fundamental power $P_{c,m}(w_0)$ from equation 3.29 and the total second harmonic output power $P_{2\omega,m}(w_0)$, also in the case of perfect impedance matching. M2, M3 and M4 mirror specifications imply $\epsilon = 0.6\%$, but no specifications exist for the anti-reflex coating on the crystal surface and some dust and scattering losses are expected to play a significant role in daily operation. For this reason I chose to carry out the calculations with 0.2% extra loss per mirror and 0.3% loss per crystal interface, giving a total $\epsilon = 1.8\%$.

These figures indicate an optimal waist of the fundamental beam of about 17 μm , but since larger waists had proven to make for more stable and robust doubling setups, we chose to set up a waist of about 30 μm and later verified that this performed well enough with regards to output power, beam profile and cavity stability.

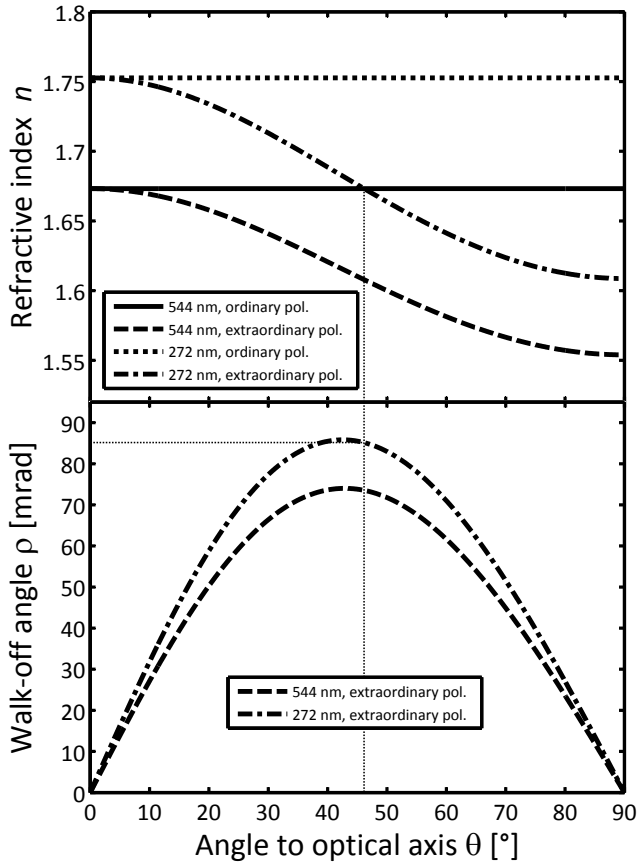
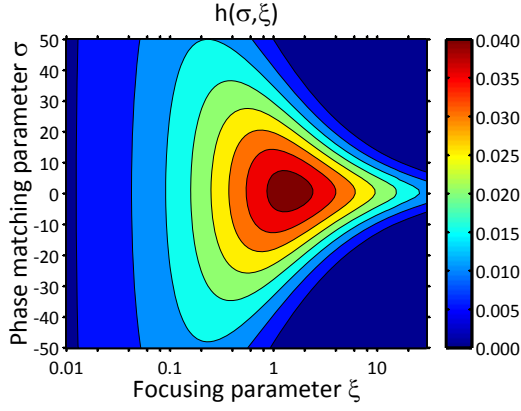
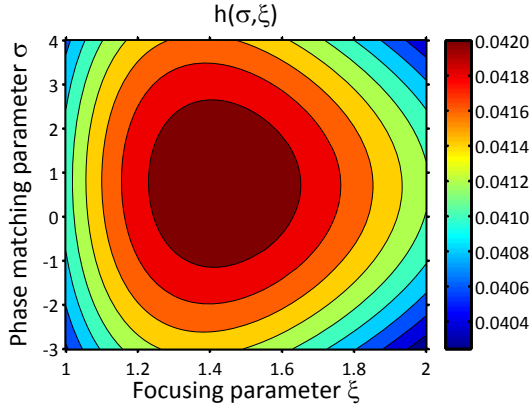


Figure 3.3: Determination of the phase matching angle in BBO for frequency doubling of 544 nm light. By choosing $\theta = 46.1^\circ$ and letting the fundamental propagate as an ordinary ray, the component of generated second harmonic light with extraordinary polarization will satisfy the phase matching condition. The walk-off angle is then $\rho = 85.2$ mrad.



(a)



(b)

Figure 3.4: (a): Values of h as a function of σ and ξ for frequency doubling of 544 nm light in a BBO crystal. The walk-off angle used for these calculations was $\rho = 85.2$ mrad and the refractive index used was $n = 1.673$. Absorption was neglected and the focus position was taken to be the crystal center. (b): A zoom on the optimal area. Note the difference in color scale.

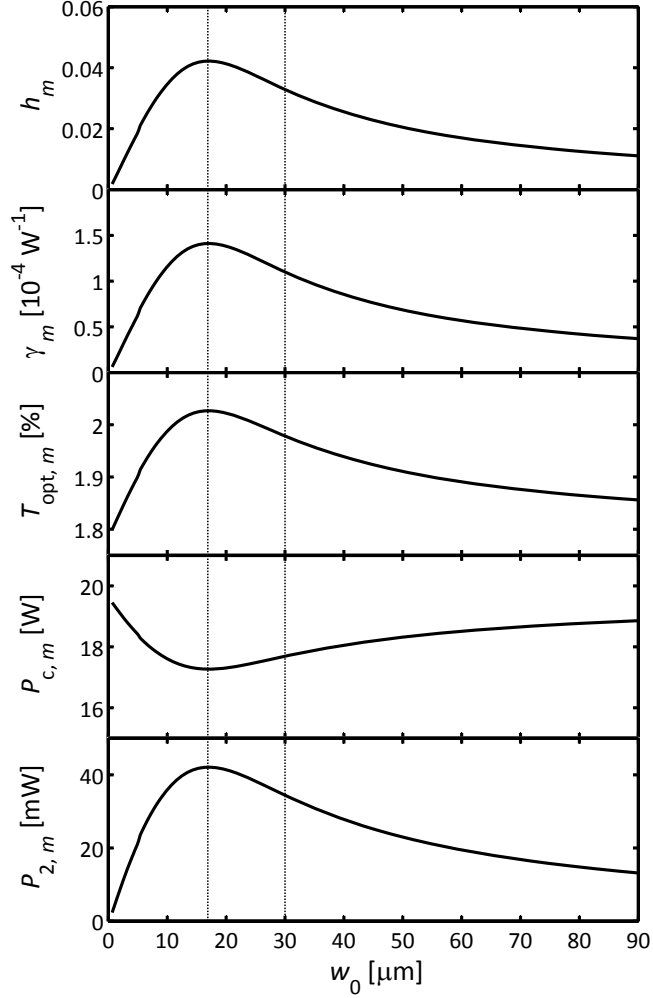


Figure 3.5: Theoretical graphs of various figures of interest in the 272 nm cavity as a function of chosen crystal waist. For these calculations, I use as linear cavity loss ϵ a realistic daily operation estimate of 1.8% per round trip. I use nonlinear coefficient $d_{\text{eff}} = 1.78 \text{ pm V}^{-1}$ and a realistic input power of 350 mW. Dashed lines indicate the theoretically optimal waist of 17 μm for SHG and the waist chosen for robustness, 30 μm .

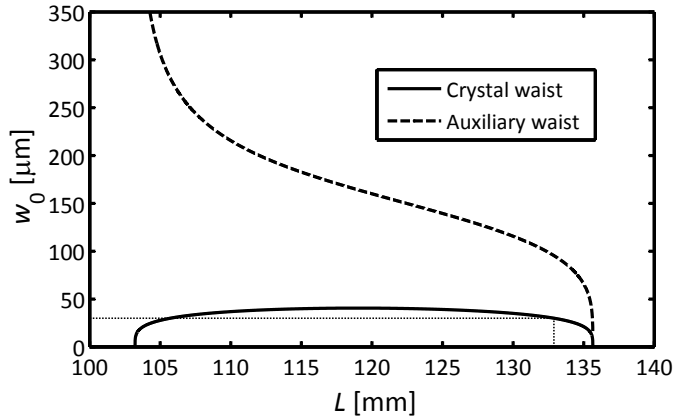


Figure 3.6: Theoretical graphs of the auxiliary waist and crystal waist in the stability region of interest. Two cavity lengths within this stability region produce a stable Gaussian mode with a waist of $30\ \mu\text{m}$ in the crystal, but the solution with larger L is preferred. This is indicated with the dotted lines, corresponding to a cavity length of $133\ \text{mm}$ and an auxiliary waist of $95\ \mu\text{m}$.

Determining cavity dimensions

Now that we have decided on a crystal waist we can turn our attention to the dimensions of the cavity itself. Using the ABCD matrix formalism of section 3.1.2 with the design of 3.2a we can graph the crystal waist and auxiliary waist as a function of cavity length L , which is done in figure 3.6.

The desired crystal waist of $30\ \mu\text{m}$ is produced for two different cavity lengths within the shown stability region. In order to minimize spherical aberration in the reflections off of the concave mirrors, the option with larger L is preferred. This is $L = 133\ \text{mm}$ and is associated with an auxiliary waist of $95\ \mu\text{m}$.

It is worth noting that an uncertainty in focal length of the curved mirrors plays a large role in the cavity dimension necessary to create a $30\ \mu\text{m}$ focus in the crystal. Repeating the calculations with a focal length of $52\ \text{mm}$ rather than the specified $50\ \text{mm}$ results in a cavity waist of $38\ \mu\text{m}$ at $L = 133\ \text{mm}$, while a focal length of $48\ \text{mm}$ pulls the instability threshold down to $130\ \text{mm}$, making a cavity with $L = 133\ \text{mm}$ unstable for all waist sizes.

3.2.2 Construction

A sketch of the optical elements in and around the cavity can be seen in figure 3.7(a). To couple the 544 nm beam into the Gaussian resonance mode of the cavity, a telescope (L1 and L2 in figure 3.7(a)) was necessary. With the use of the telescope immediately before the cavity, the focus generated with the telescope was made to match as closely as possible with the auxiliary focus of the resonant mode, both in waist and in position. An imperfect overlap, longitudinally or transversally, results in some of the light being coupled into unwanted higher order Hermite-Gaussian modes of the cavity.

In order for the cavity to be resonant for the 544 nm light, the total phase shift in one round trip must be a multiple of 2π . Because of acoustic vibrations, thermal drift and other disturbances it is necessary to maintain this resonance condition by moving one of the mirrors (in this case M2) back and forth by glueing it onto a piezoelectric transducer (PZT). Using the Hänsch-Couillaud locking scheme [84], this PZT can lock the cavity length to resonance with the aid of a servo loop. Alternatively, by simply applying a triangular scan signal to the PZT, the resonance can be seen as a peak in the scan for each phase shift of 2π (one free spectral range, FSR) covered in the scan. Because of the Gouy phase shift occurring in the two focuses [85], the higher order Hermite-Gaussian modes denoted TEM_{nm} will be displaced from the Gaussian mode TEM_{00} by a value proportional to $(n+m)$ in phase shift and, consequently, in PZT resonance position. The scan signal thus makes it possible to mode-match the cavity, that is, to obtain maximal intracavity TEM_{00} intensity by optimizing the cavity alignment and length as well as the alignment, focus position and waist of the 544 nm that is coupled into the cavity.

Figure 3.7 (a) shows the optical elements involved in the cavity setup. Lenses L1 and L2 form the telescope that couples into the auxiliary waist. Using the half-wave plate before the cavity, one can control how much light to couple into the cavity and how much to send to the locking signal by reflection off of M1. The polarization analysis elements for the Hänsch-Couillaud scheme consist of a half-wave plate, a quarter-wave plate and a polarizing beamsplitter cube. The generated 272 nm light is collimated in the vertical direction with a spherical lens L3 and magnified and collimated in the horizontal direction by a cylinder lens telescope, CL1 and CL2. A photograph of the final setup is shown in figure 3.8.

The electronic control part is visualized in figure 3.7 (b) in a block diagram. The crystal is mounted inside a copper holder on a Peltier element with a thermosensor. A temperature controller reads the thermosensor and controls the current in the Peltier element to match a temperature setting specified on

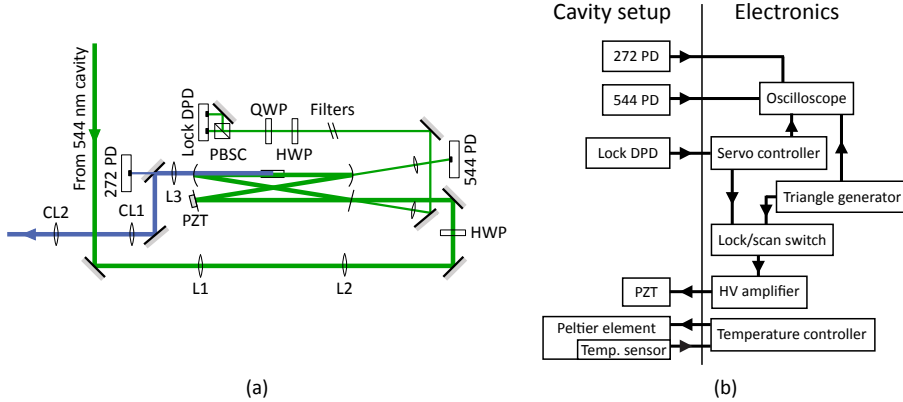


Figure 3.7: (a): Sketch of the optical setup for the 272 nm cavity. (b): Block diagram of electronic components for the 272 nm cavity. L: Lens, HWP: Half-wave plate, QWP: Quarter-wave plate, PBSC: Polarizing beam-splitter cube, Lock DPD: Locking signal differential photodetector, 544 PD: Intracavity 544 nm photodetector, 272 PD: Output 272 nm photodetector, CL: Cylinder lens, PZT: Piezoelectric transducer.

its front panel.

The differential photodetector provides the Hänsch-Couillaud error signal, which is processed in a servo loop to reduce high- or low-frequency components and used to adjust the lock signal voltage to obtain or maintain resonance. To produce the high voltages needed for the PZT, a biased high voltage amplifier is used that accepts between -5 V and $+5\text{ V}$ input and yields between 0 V and 450 V output.

3.2.3 Characterization

After finishing the mode-matching optimization, cavity characterization could be performed. While I had aimed for a crystal waist of about $30\text{ }\mu\text{m}$, the actual achieved crystal waist was important to know and thus was measured. This was done by blocking the path from M4 to M1 and measuring the variation of the 544 nm light transmitted through M4 as I gradually inserted a knife edge into the beam at different positions relative to the crystal center. The results from these measurements with the appropriate Gaussian fit is shown in figure 3.9. The fit result for the waist is $34.3\text{ }\mu\text{m}$. This was achieved at cavity length $L = 135\text{ mm}$,

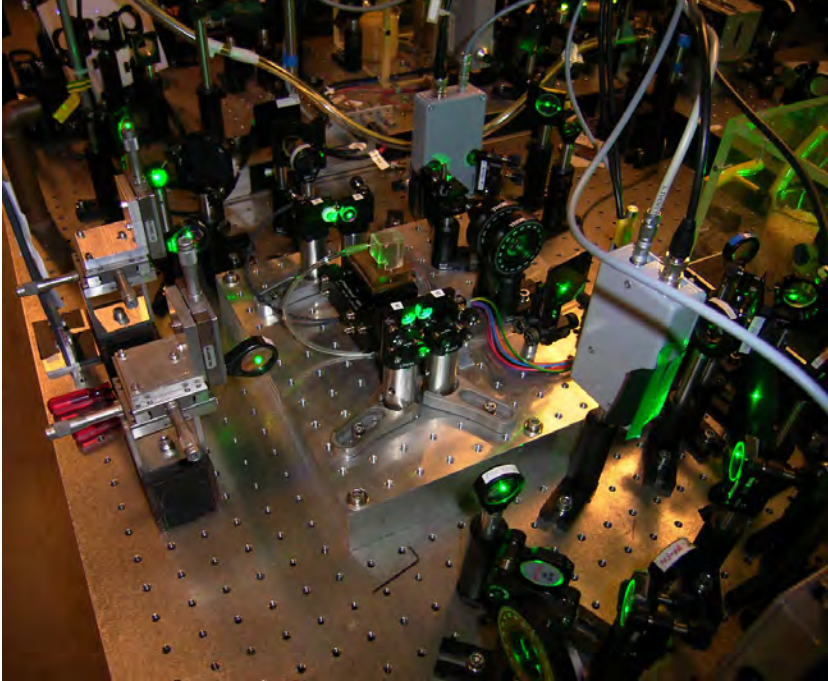


Figure 3.8: A photograph of the finished cavity construction. The tube connecting to the housing around the BBO crystal supplies dry air to avoid hygroscopic expansion. The generated 272 nm light can be seen as the right-most blue fluorescence dot on the paper in the upper left corner.

consistent with the actual focal lengths of the curved mirrors being $f = 51.5$ mm rather than the specified 50 mm.

Some traces illustrating the relevant oscilloscope signals in the scanning and locking modes of operation are shown in figure 3.10.

When the PZT lock is engaged and the cavity becomes resonant, it causes the optical path length of the crystal to decrease, most likely due either to slow buildup of temporary photorefractive effects or thermal effects due to light absorption. The PZT must compensate for this decreased optical path length, effectively causing a drift of the PZT voltage level as depicted in figure 3.11 (a). During this time, if the PZT goes out of its range it will need to be re-locked to the peak in the next free spectral range, providing enough extra compensation

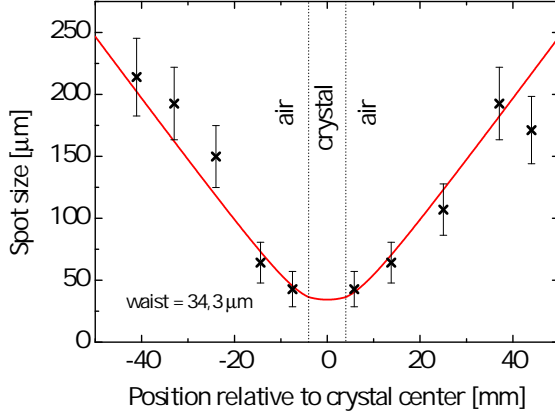


Figure 3.9: Spot size measurements for determining the crystal waist, with the best fit to a Gaussian beam shown in red. Refractions at the crystal surfaces are accounted for in the fit.

room for stable on-peak operation.

Finally, I measured the total effective conversion efficiency $\gamma_{\text{eff}} = P_{2\omega}/P_{\omega}^2$ of the cavity, where $P_{2\omega}$ is the power of the final 272 nm output and P_{ω} is the input power measured between the incoupling telescope and the cavity. These measurements are depicted in figure 3.11 (b). To reach powers lower than usual without changing the operating conditions for the 544 nm cavity, We chose to insert a half-wave plate and a polarizing beamsplitter between L2 and M1 to easily vary the input power. While the transversal overlap with the auxiliary focus was reoptimized at every measurement, the longitudinal overlap with the auxiliary focus was only optimized for the point with normal operating power, ~ 350 mW, the case without the inserted half-wave plate and polarizing beamsplitter. Therefore, the accomplished powers at all but that point no doubt would have been higher with a fine tuned mode matching. The highest power achievable with the half-wave plate and polarizing beamsplitter inserted was 260 mW.

Note that when optimizing the cavity, the user can choose how much of the incoming power to send to the locking signal at cavity resonance by rotating the half-wave plate immediately before the cavity. In normal use, as well as for all

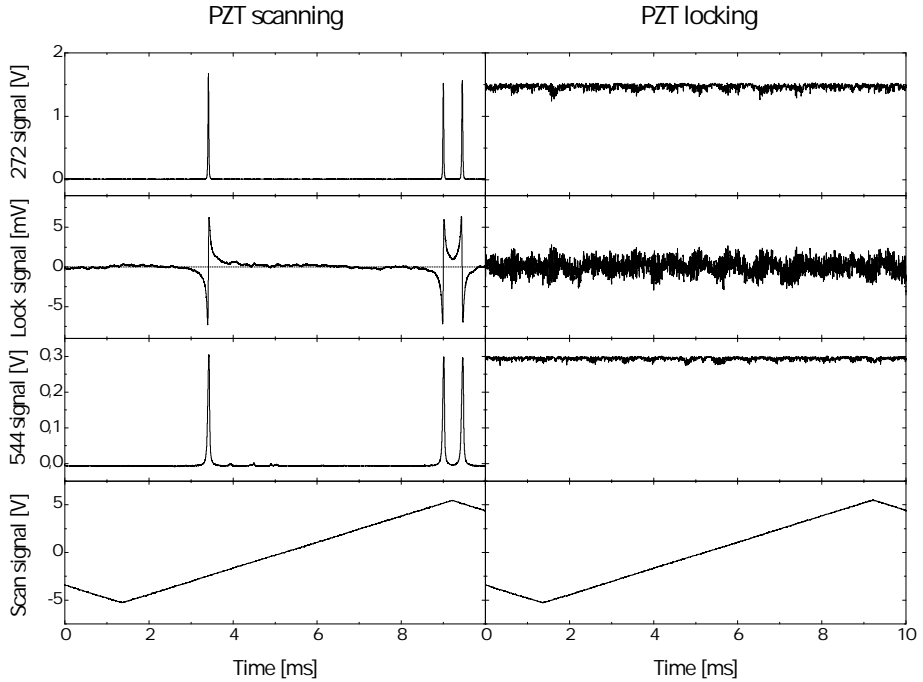


Figure 3.10: Typical oscilloscope signals at optimized cavity operation. The top row shows the detector signal for the generated 272 nm light, second row is the locking signal from the servobox, third row shows intracavity fundamental power, while the fourth row depicts the scan signal. When locking, the scan signal is used only for oscilloscope triggering.

the measurements performed for this thesis, about 10% of the green light was sent to the locking signal to make for as robust a lock as is possible with the current PZT. By reducing this percentage, one can get a higher total conversion efficiency at the expense of lock robustness.

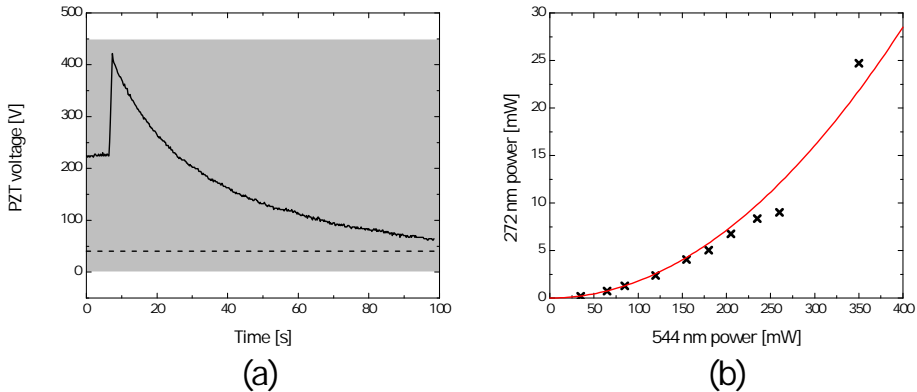


Figure 3.11: (a): The displacement compensation that is performed by the PZT due to photorefractive or thermal effects in the crystal is shown here in terms of the voltage sent to it by the HV amplifier. In the first 7 seconds, the servo was not set to lock and the PZT rested in the middle of the utilizable voltage range, indicated by the gray shaded area. At 7 seconds, the lock was engaged and the PZT found a peak near the high end of the range. Due to the high intracavity intensity, the photorefractive or thermal effects built up until the PZT displacement, in this case, reached an equilibrium at about a PZT voltage of 40 V, shown as the dashed line. (b): The output power as a function of input power. The power at normal operation is ~ 350 mW. All measurements at lower power were taken with a half-wave plate and a polarizing beamsplitter inserted into the beam, which adversely affected the mode matching quality. The red curve is the best fit to the function $P_{272} = \gamma_{\text{eff}} P_{544}^2$, with $\gamma_{\text{eff}} = 1.8 \times 10^{-4} \text{ mW}^{-1}$.

3.3 559 nm second harmonic generation cavity

3.3.1 Design

For doubling of 1119 nm light, an LBO (lithium triborate, LiB_3O_5) crystal was used in a non-critical phase matching scheme. LBO is a negative biaxial crystal and can be used for critical type I phase matching in the range 554 nm to 2600 nm, but the temperatures necessary for non-critical type I phase matching are only practical within the range[86] of roughly 1025 nm ($T = 190.3^\circ\text{C}$) to roughly 1250 nm ($T = -2.9^\circ\text{C}$). It is transparent in the region 155 nm to 3200 nm. The SHG coefficient is moderate, and laser damage threshold is high.

Crystal length l	8 mm	M1 reflectivity	99.0 %
Cavity length L	135 mm	M2 reflectivity	99.9 %
Mirror separation b	14 mm	M3 reflectivity	99.6 %
Meas. crystal waist w_c	34.3 μm	M4 reflectivity (ω)	99.9 %
Calc. auxiliary waist w_a	112 μm	M4 transmittivity (2ω)	85 %
Distance L1 to L2	162 mm	L1 focal length	50 mm
Distance L2 to M1	624 mm	L2 focal length	100 mm
Distance M4 to L3	103 mm	M3 and M4 focal length	50 mm
Distance L3 to CL1	165 mm	L3 focal length	150 mm
Distance CL1 to CL2	300 mm	CL1 focal length	100 mm
Conversion efficiency γ_{eff}	0.18 W ⁻¹	CL2 focal length	200 mm

Table 3.1: Some figures of interest for the 272 nm cavity. Mirror reflectivities, M4 transmittivity and focal lengths are specifications.

LBO is not hygroscopic.

Satisfying the non-critical phase matching condition in the biaxial LBO crystal

In non-critical temperature phase matching, the beam propagates along one of the crystallographic axes of the crystal, while temperature is adjusted to match the refractive indices of the fundamental component and the second harmonic component. This is made possible due to a difference in temperature dependence of the refractive index for beams with different polarizations and different wavelengths. We use Sellmeier equations and thermo-optic coefficients from Newlight Photonics [87] to calculate the refractive indices in the crystal:

$$n_x = \sqrt{2.454140 + \frac{0.011249}{\lambda^2 - 0.011350} - 0.014591\lambda^2 - 6.60 \times 10^{-5}\lambda^4} + (-3.76\lambda + 2.30) \times 10^{-6} \times (T - 22^\circ\text{C}) \quad (3.35)$$

$$n_y = \sqrt{2.539070 + \frac{0.012711}{\lambda^2 - 0.012523} - 0.018540\lambda^2 + 2.00 \times 10^{-4}\lambda^4} + (6.01\lambda - 19.40) \times 10^{-6} \times (T - 22^\circ\text{C}) \quad (3.36)$$

$$n_z = \sqrt{2.586179 + \frac{0.013099}{\lambda^2 - 0.011893} - 0.017968\lambda^2 - 2.26 \times 10^{-4}\lambda^4} + (1.50\lambda - 9.70) \times 10^{-6} \times (T - 22^\circ\text{C}) \quad (3.37)$$

In these equations, the subscripts x, y, z denote the direction of polarization of the wave, the vacuum wavelength λ is in micrometers and T denotes the temperature in degrees celsius. A plot of these three refractive indices for the fundamental and the second harmonic light is presented in figure 3.12. From these equations, the phase matching condition is expected to be satisfied at 88.4°C with $n = 1.6038$. The walk-off angle is zero as is always the case for non-critical phasematching.

Calculating the optimal crystal waist

As with the 272 nm cavity, the Boyd and Kleinman theory can be applied to determine the optimal crystal waist. For different values of ξ and σ , equation 3.3 is evaluated and plotted in figure 3.13.

Just as in the BBO case in the previous section, we choose to consider only the optimal phase matching parameter σ for each value of ξ . This optimization with regards to σ is done experimentally by fine tuning the temperature of the crystal. The notation is as in the previous section concerning the 272 nm cavity.

The sigma-optimized cavity parameters are plotted in figure 3.14 along with $\gamma_m(w_0)$ from equation 3.2, the optimal input coupler transmission $T_{\text{opt},m}(w_0)$ from equation 3.30, the resulting impedance matched intracavity fundamental power $P_{c,m}(w_0)$ from equation 3.29 and the total second harmonic output power $P_{2\omega,m}(w_0)$, also in the case of perfect impedance matching. M2, M3 and M4 mirror reflectivity specifications are $R = 99.9\%$ each and the anti-reflex coatings on the crystal surface are specified as $T = 99.9\%$. From this, we take $\epsilon = 0.5\%$ for use in the calculations.

Determining cavity dimensions

As for the 272 nm cavity, we now use the ABCD matrix formalism of section 3.1.2 to determine the cavity dimensions, but now with the design of 3.2b. We graph the crystal waist and auxiliary waist as a function of cavity length L , which is done in figure 3.15.

From figure 3.15 it is found that the desired crystal waist $31.1 \mu\text{m}$ is achieved at $L_1 = 107.5 \text{ mm}$, $L_2 = 62.1 \text{ mm}$. At these dimensions, the auxiliary waist is $205 \mu\text{m}$. A benefit to this design compared to that of the 272 nm cavity is that

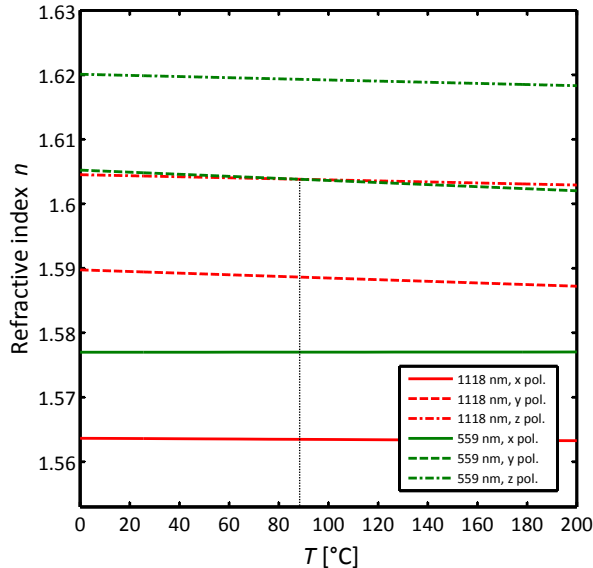


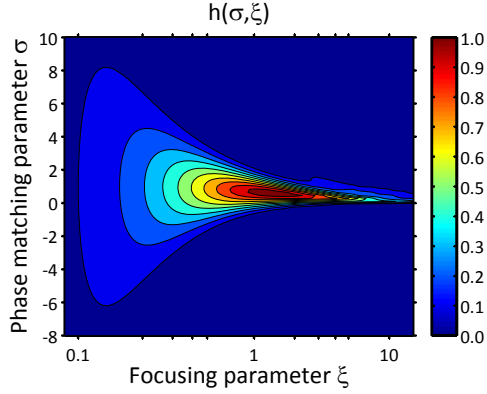
Figure 3.12: Determination of the phase matching angle in LBO for frequency doubling of 1118 nm light. Shown are the refractive indices for the three possibilities of polarizations along the crystallographic axes for the fundamental and for the second harmonic radiation as a function of temperature. By raising the crystal temperature to $T = 88.4^\circ\text{C}$ and letting the fundamental propagate along the x -axis with polarization along the z -axis, the component of generated second harmonic light with polarization along the y -axis will satisfy the phase matching condition.

the effect of uncertainty in placement of the mirrors and uncertainty in the focal length of the curved mirrors is greatly mitigated.

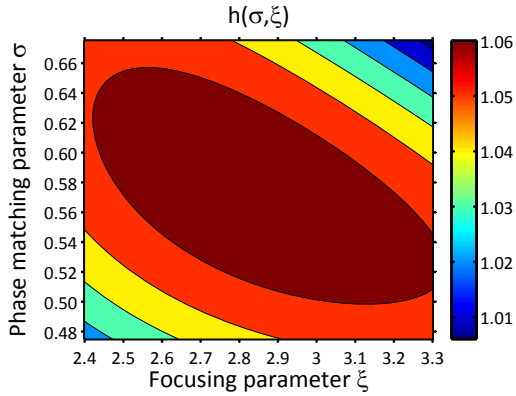
3.3.2 Construction

The construction and layout of the elements for the 559 nm cavity is very similar to that of the 272 nm cavity, the main differences being the generation of the lock signal and the addition of an extra PZT to the cavity. A sketch of the optical setup is provided in figure 3.16.

The fiber laser emitting the 1118 nm light is placed on a shelf right above



(a)



(b)

Figure 3.13: (a): Values of h as a function of σ and ξ for frequency doubling of 1118 nm light in an LBO crystal. The walk-off angle is zero and the refractive index used was $n = 1.6038$. Absorption was neglected and the focus position was taken to be the crystal center. (b): A zoom on the optimal area. Note the difference in color scale. The phase matching optimum is much narrower than in the critical phasematching case of figure 3.4. Due to the oscillatory nature of the integrand in equation 3.3, h starts to exhibit structure in the $\xi > 3$ region, visible in (a).

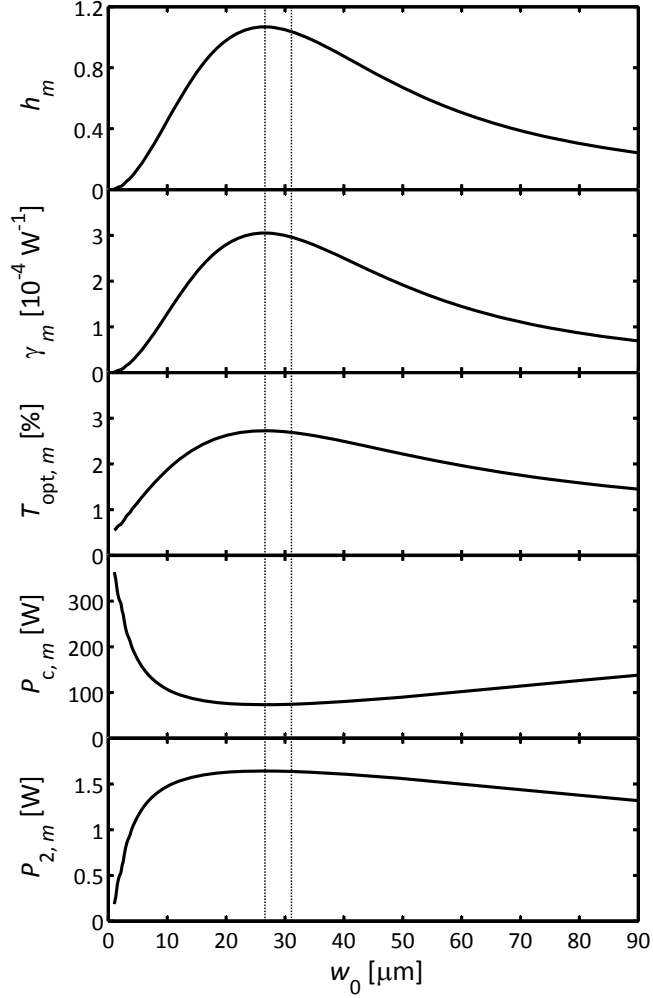
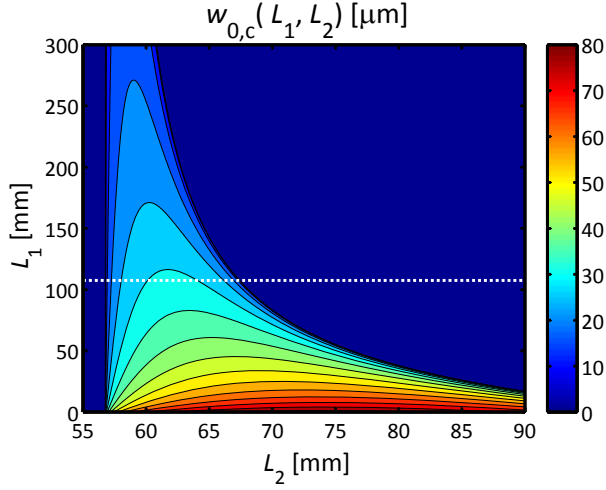
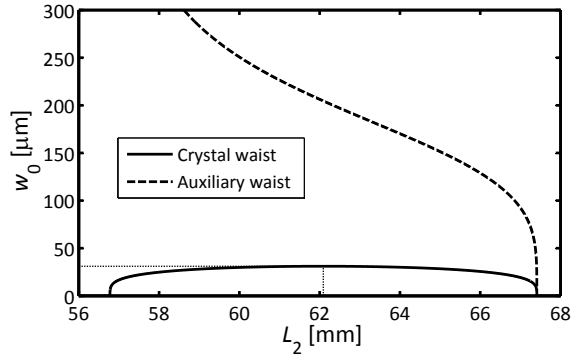


Figure 3.14: Theoretical graphs of various figures of interest in the 559 nm cavity as a function of chosen crystal waist. For these calculations, I use as linear cavity loss per round trip $\epsilon = 0.5\%$. I use nonlinear coefficient $d_{\text{eff}} = 0.98 \text{ pm V}^{-1}$ and the maximum input power of 2 W. Dashed lines indicate the theoretically optimal waist of $26.6 \mu\text{m}$ for SHG and the waist chosen for robustness, $31.1 \mu\text{m}$.

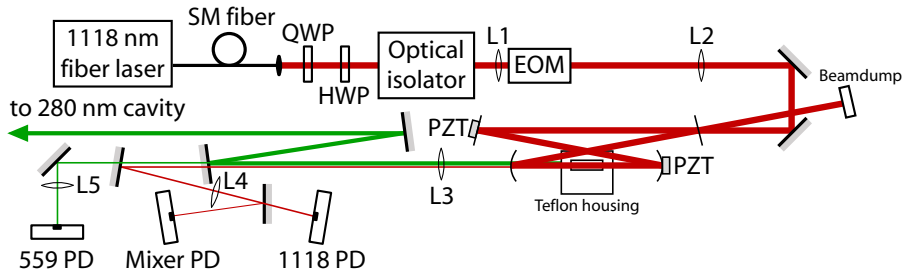


(a)

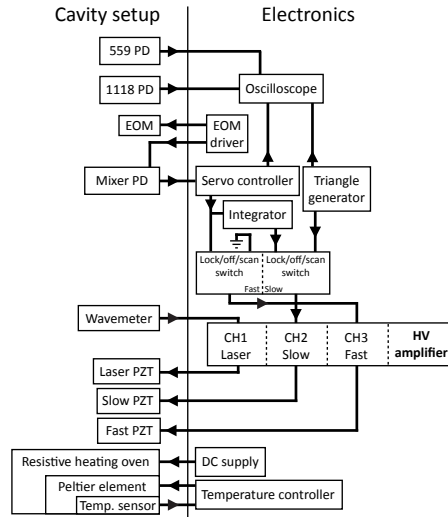


(b)

Figure 3.15: (a): Contour plot of the theoretical crystal waist as a function of the two cavity dimensions L_1 and L_2 . The crystal waist is plotted as zero outside the stability region. $L_1 = 107.5$ mm (indicated with the dotted line) was chosen such that the desired crystal waist of 31.1 μm was obtained as the maximum value along the L_2 direction. (b): The crystal waist and auxiliary waist as a function of L_2 for $L_1 = 107.5$ mm. The crystal waist 31.1 μm is the maximum and is achieved at $L_2 = 62.1$ mm.



(a)



(b)

Figure 3.16: (a): Sketch of the optical setup for the 559 nm cavity. (b): Block diagram of electronic components for the 559 nm cavity. SM fiber: Single-mode fiber, HWP: Half-wave plate, QWP: Quarter-wave plate, EOM: Electro-optic modulator, L: Lens, Mixer PD: Infrared photodetector with mixer to extract component at the EOM frequency, 1118 PD: Intracavity 1118 nm photodetector, 559 PD: Output 559 nm photodetector, PZT: Piezoelectric transducer.

the doubling cavity. The light is output through a Schäfer + Kirchhoff fiber collimator before going through the optical isolator setup for protection of the fiber laser. The optical isolator setup consists of a quarter wave plate, a half wave plate and a Conoptics model 715 optical isolator. The wave plates ensures the infrared light is linear polarized at a 45° angle to vertical. This polarization ensures maximum transmission through the optical isolator, and the output becomes vertically polarized. The optical isolator is specified for 92% transmission and between 37 dB and 40 dB attenuation of feedback.

After this, the light passes through a telescope of two spherical lenses that we denote L1 and L2, with focal lengths $f_1 = f_2 = 100$ mm. With these two lenses, the overlap with the auxiliary focus of the cavity mode is maximized, ensuring that as much as possible of the fundamental power is coupled into the Gaussian TEM₀₀ mode of the cavity rather than the higher order Hermite-Gaussian TEM_{*nm*} modes of the cavity.

The lock signal is generated through the Pound-Drever-Hall (PDH) scheme[88, 89], which requires frequency modulation of the input beam. This is done with an electro-optic modulator (EOM) placed inside the incoupling telescope, between L1 and L2. The EOM is home-built and consists of a 15 mm long *z*-cut Lithium Niobate (LiNbO₃, LN) crystal resting between two copper sheets over which a ~ 10 MHz AC voltage is applied. The oscillating electric field laid over the crystal will undergo a small degree of sum- and difference frequency mixing with the infrared laser beam to create the modulation side bands necessary for the PDH locking scheme. A fast photodetector monitoring the intracavity infrared signal mixes the signal with an EOM voltage reference signal taken directly from the EOM driver. This extracts the PDH lock signal, which is then subsequently frequency filtered, amplified and integrated in a servo loop.

Since the cavity length change necessary for a phase shift of 2π is equal to one wavelength, 1118 nm, a larger displacement of the locking PZT is, in general, necessary to obtain or maintain resonance than in the 272 nm cavity case. However, the single layer PZTs we normally use (Ferroperm Pz27 tube PZTs [90]) only have a maximum length change response on the order of one micrometer, corresponding to only about two free spectral ranges of the cavity. To provide some more leeway for vibrations of the mirrors, drifts in the crystal conditions and intentional frequency changes of the laser, we decided to put mirror M3 on a multilayer PZT (Piezomechanik HPCh 150/8-3/2) in addition to mounting M2 on a single layer Pz27 tube. Since M2 is light and the M2 PZT has a low capacitance, its response is fast and we refer to the M2 PZT as the fast PZT. The M3 PZT has higher capacitance and a heavier mirror, so it is referred to as the slow PZT.

For cavity diagnostics, the fast PZT is set to 'off', resting in the middle of its range, while the slow PZT is scanning back and forth through a few free spectral ranges. In locking mode, the PDH locking signal is coupled onto the fast PZT, while the slow PZT moves such that the fast PZT is brought towards the middle of its range. This is accomplished by using as error signal the difference between the fast PZT voltage and the mid-point of its range. The servo loop for the slow PZT is home made and consists simply of an Op-Amp integrator.

A spherical lens (L3, $f_3 = 200$ mm) collimates the 559 nm output of the cavity for sending the light to the 280 nm cavity. Two mirrors for green light are mounted close to the 559 nm cavity for easy steering of the output beam.

For diagnostics, two photodetectors are set up to monitor the intracavity infrared power and the produced second harmonic power. This is monitored off of the small component of light transmitted through both M4 and the first mirror sending the green light towards the 280 nm cavity. For the infrared light, only a little leaks through M4 while the first green mirror is mostly transparent. For the green light, M4 is 95 % transmitting, while the first green mirror only transmits a small fraction. The two wavelengths are then separated with a dichroic mirror and focused onto two photodetectors. Filters are mounted directly on the photodetectors to prevent green light registering on the infrared detector and infrared light from registering on the green detector.

Two photographs of the final setup are shown in figure 3.17.

The electronic control part is visualized in figure 3.16 **(b)** in a block diagram. The wavelength of the fiber laser is controlled by changing the voltage on an internal PZT in the laser.

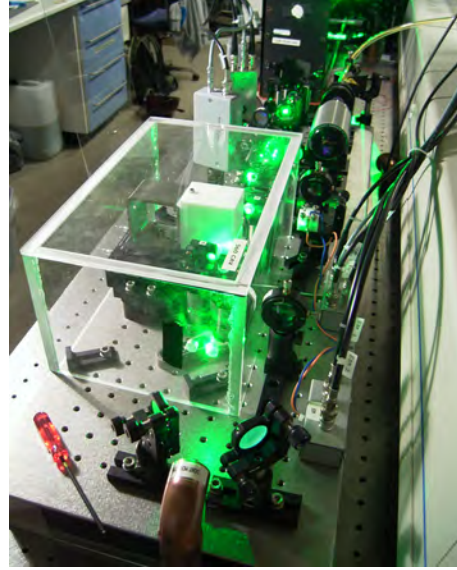
The crystal is mounted inside a oven consisting of a copper holder with a thermosensor, resting against a Peltier element. The Peltier element is in turn resting against a copper block with power resistors on it. All this is encased in a Teflon housing. To raise the temperature to $T = 88.4^\circ\text{C}$, a current is passed through the resistors to heat the copper block to close to the target temperature, while the Peltier element takes care of the rest of the temperature difference with feedback from the thermosensor. Small holes in the Teflon housing allow the laser beams to pass through.

3.3.3 Characterization

Characteristic oscilloscope traces in scanning mode and locking mode can be seen in figure 3.18. The output power and conversion efficiency was measured and is shown in figure 3.19, and a list of specifications is included in table 3.2.



(a)



(b)

Figure 3.17: Two photographs of the final 559 nm cavity setup. (a): In this image, the infrared beam (~ 2 W) is on, but the cavity is not locked on resonance. Despite this, a very small amount of green second harmonic light is visible. In the bottom left of the image, the output coupler of the fiber laser is seen. The crystal resides within the white Teflon block in the middle of the cavity. The input 1118 nm light that is reflected off of M1 is dumped in the copper tube at the top of the image and apparently registers as violet in the color filter array of the digital camera, making it readily visible in this image. (b): A view from the opposite direction with a protective acrylic housing over the cavity and with the cavity locked, producing ~ 1 W 559 nm radiation.

Crystal length L_c	18 mm	M1 reflectivity	96.4 %
Flat mirror separation L_1	107.5 mm	M2,3,4 reflectivity (ω)	99.9 %
Curved mirror separation L_2	62.1 mm	M4 transmittivity (2ω)	95 %
Folding angle α	10°	M3,4 focal length	25 mm
Calc. crystal waist $w_{0,c}$	31.1 μm	L1 focal length	100 mm
Calc. auxiliary waist $w_{0,a}$	205 μm	L2 focal length	100 mm
Distance FC to L1	385 mm	L3 focal length	200 mm
Distance L1 to L2	255 mm	L4 focal length	150 mm
Distance L2 to M1	401 mm	L5 focal length	75 mm
Distance M4 to L3	177 mm	Eff. conv. efficiency	$\leq 49\%$
Calc. temperature T	88.4 °C		

Table 3.2: Some figures of interest for the 559 nm cavity. FC: Fiber collimator. Mirror reflectivities, M4 transmittivity and focal lengths are specifications. The effective conversion efficiency is defined as in figure 3.19 and is provided here for the maximum input power.

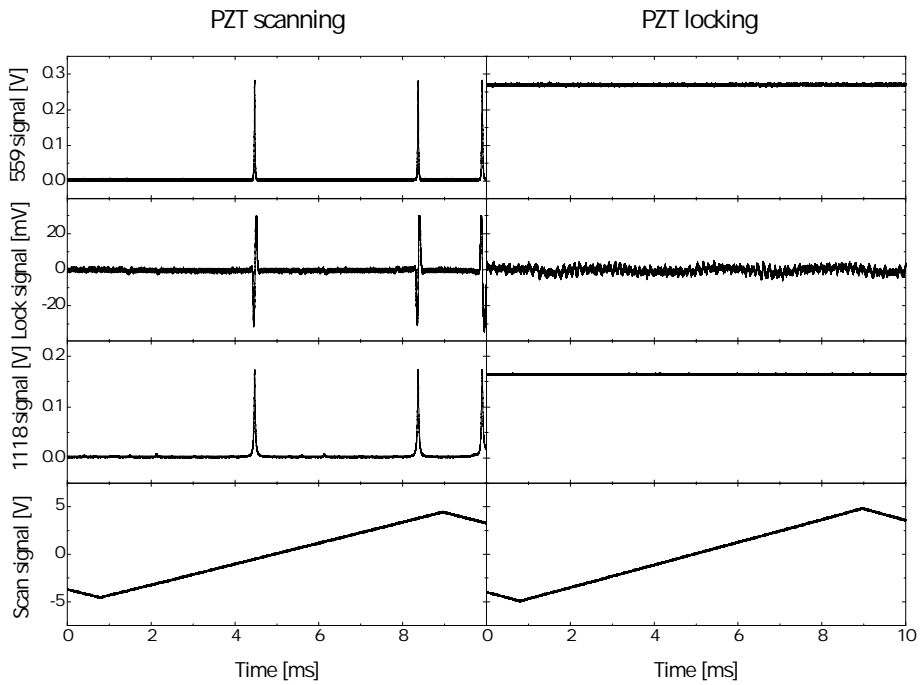


Figure 3.18: Typical oscilloscope signals at optimized cavity operation. The top row shows the detector signal for the generated 559 nm light, second row is the locking signal from the servobox, third row shows intracavity fundamental power, while the fourth row depicts the scan signal. When locking, the scan signal is used only for oscilloscope triggering.

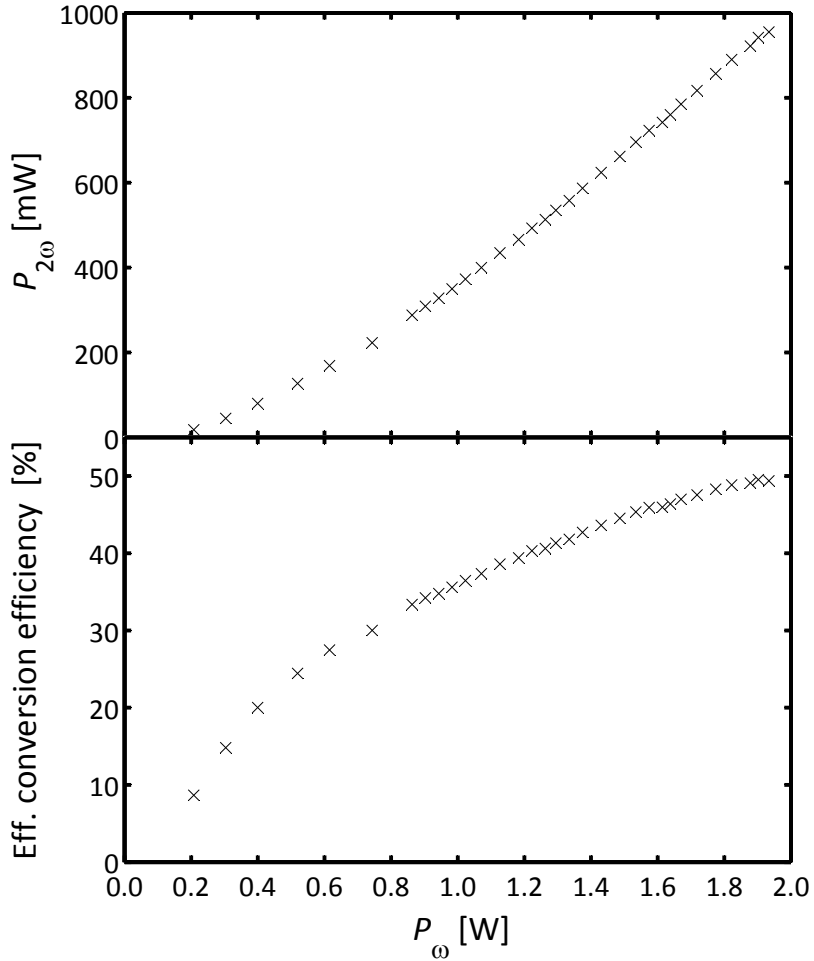


Figure 3.19: 559 nm cavity performance in terms of the fundamental power incident on M1 and the second harmonic power leaving the cavity breadboard after collimating optics and two mirrors. The effective conversion efficiency is defined as $P_{2\omega}/P_\omega$. At low input powers, the lock quality becomes poor, reducing the output power. At high input powers, saturation of the SHG process is clearly evident as the deviation from the quadratic $P_{2\omega} = \gamma_{\text{eff}} P_\omega^2$ dependence valid at low powers.

Rotational cooling and population distribution measurement: Theory

Much of the appeal of the cold molecule field lies in the possibilities that arise from preparing an ensemble in a specific quantum state, such as the ground state. While sympathetic cooling in a Coulomb crystal is highly effective in cooling the motional degree of freedom of molecular ions to temperatures down to a few millikelvin, there is no significant coupling between the internal and external degrees of freedom for ions in a Coulomb crystal [91, 92], so the rotational and vibrational degrees of freedom remain uncooled. Prior to the publication of the results of chapter 6, only helium buffer gas cooling had been successful in cooling the internal state of molecular ions [42]. The scheme we have implemented is based on a proposal made in 2002 by Ivan Vogelius *et al.* [63], based on optical pumping on a rovibrational transition. A requirement for this scheme is that the molecules are polar and get enough time to equilibrate with the black body radiation, which in a room temperature environment takes tens of seconds. Thus, molecular ions in an ion trap are perfect candidates for this scheme due to the very long trapping times.

To measure the rotational state distribution with and without cooling, two resonance enhanced multi-photon dissociation (REMPD) schemes were used, one based on dissociating with only a single color, the other using two colors for the process. In these schemes, ns-pulses couple from a chosen rotational state through an electronically excited state and from there into a dissociating state. The dissociation products escape the trap and the amount of dissociated molecules can therefore be read directly as a drop in the amount of non-fluorescent ions from the bicrystal analysis program that will be presented in section 5.4.

In this chapter, I will explain the theoretical background behind these two techniques, present some simulation results and finally evaluate the applicability of these techniques on CaH^+ .

4.1 Rotational cooling scheme for MgH⁺

4.1.1 Vibrational and rotational levels of MgH⁺

MgH⁺, being a diatomic molecule, has only one mode of vibration. We denote the quantum number for the vibrational state v , with $v = 0$ being the ground state. Furthermore, being a linear rotor, its rotational state is completely described by the angular momentum, the magnitude of which we denote J , and the length of the projection of this angular momentum onto a laboratory fixed axis, which we call M_J . For the lower rotational levels in any given vibronic state, the energies can be approximated by the expression $E_J = BJ(J + 1)$, where B is the rotational constant of the molecule in that particular electronic state. For the $X^1\Sigma^+$ ground state of $^{24}\text{MgH}^+$, $B = 9 \text{ K} \cdot k_B$, where k_B is Boltzmann's constant.

MgH⁺, being a polar molecule, has a permanent dipole moment and a non-zero derivative of the dipole moment function at the internuclear equilibrium distance. The molecule therefore interacts strongly with electromagnetic radiation through dipole-allowed rotational and rovibrational transitions. The selection rule for both rotational and rovibrational transitions is $\Delta J = \pm 1$. For rovibrational transitions, this gives rise to the R-branch transitions ($\Delta J = +1$) and P-branch transitions ($\Delta J = -1$). To give a general idea of the time scales involved in these dynamics, typical vibrational spontaneous decay rates are on the order of 10 Hz. The relevant rotational spontaneous decay rates are lower than the vibrational ones, two examples being $\sim 0.002 \text{ Hz}$ for $J = 1$ to $J = 0$ and $\sim 1 \text{ Hz}$ for decay from $J = 7$ to $J = 6$.

4.1.2 Black body radiation

A central concept to the rotational dynamics of molecules is black body radiation. A black body is an idealized object that absorbs perfectly at all wavelengths and since a good absorber is necessarily also a good emitter, a black body will be emitting light at all wavelengths in a distribution determined by its temperature. The molecular ions in the traps used for the work in this thesis are exposed to a nearly ideal black body spectrum from the surroundings. If all surroundings have temperature T , the radiation energy density distribution ρ is determined by Planck's law,

$$\rho(\omega, T) = \frac{\hbar\omega^3}{\pi^2 c^3} \frac{1}{\exp\left(\frac{\hbar\omega}{k_B T}\right) - 1} \quad (4.1)$$

If the materials surrounding the molecules are not all of the same temperature but have a discrete set of temperatures T_i occupying corresponding solid angles Ω_i , the black body radiation field experienced by the molecules is

$$\rho(\omega, T_1, \Omega_1, T_2, \Omega_2, \dots) = \frac{\Omega_1}{4\pi} \rho(\omega, T_1) + \frac{\Omega_2}{4\pi} \rho(\omega, T_2) + \dots \quad (4.2)$$

where we are again assuming that the surroundings are perfect black bodies.

If the surrounding materials are partly reflecting or scattering for the predominantly infrared thermal radiation, the materials' emissivities are said to be less than one and they cannot be assumed to be perfect black bodies. This is usually the case for polished shiny metal surfaces such as the copper and stainless steel on the inside of vacuum chambers. The radiation energy density distribution is in this case more complicated. Equation 4.1 still holds if all surroundings have the same temperature, while equation 4.2 will not. In that case, ρ will depend not only on solid angles and temperatures of the surroundings but also the wavelength dependent emissivities and the specific geometric configuration.

We will now consider the case of a radiation energy density distribution described by equation 4.1. In this case, the resulting population distribution $P(J)$ per degeneracy $2J + 1$ among levels in a system in thermal equilibrium follows a Boltzmann distribution:

$$\frac{P(J)}{2J + 1} = C \exp\left(-\frac{E_J}{k_B T}\right) \quad (4.3)$$

where C is a normalization factor to ensure the sum of all populations is 1.

Since the vibrational spacing of the MgH^+ ground state is large enough that only 0.1 % of a molecular ensemble is vibrationally excited at room temperature, it is a good approximation to assume that thermal excitations at room temperature only take place in the rotational degree of freedom. The level population is highest for $J = 4$ at room temperature, with the population in the rotational ground state being only 3%.

4.1.3 Rovibrational optical pumping

To improve on these 3% in the ground state, the scheme proposed by Ivan Vogelius consists of exciting the rovibrational transition $|v = 0, J = 2\rangle \rightarrow |v = 1, J = 1\rangle$ with an infrared laser, as shown in figure 4.1. This is a dipole allowed transition and does not require a high intensity to saturate. From this vibrationally excited state, there are two dipole allowed pathways of spontaneous

decay: To the $|v = 0, J = 0\rangle$ ground state or back to the $|v = 0, J = 2\rangle$ state. By continually driving this transition, one empties the $|v = 0, J = 2\rangle$ state by optical pumping to the rovibrational ground state.

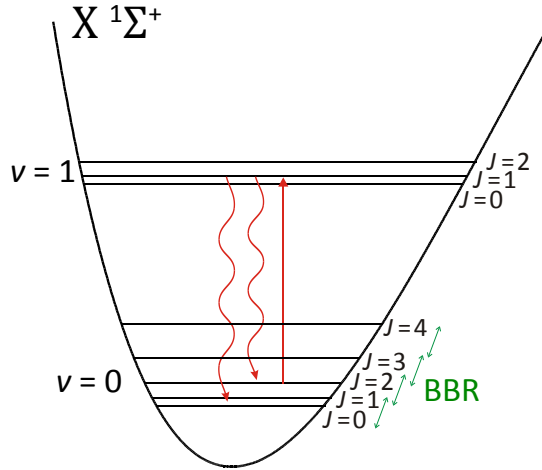


Figure 4.1: Sketch of the electronic ground state of MgH^+ illustrating the direct scheme proposed by I. Vogelius et al. The rotational degree of freedom is cooled with dipole allowed optical pumping from $|v = 0, J = 2\rangle$ to $|v = 0, J = 0\rangle$. The black body radiation (BBR) and spontaneous decay ensures that rotational states with $J > 2$ also get pumped to the ground state.

While this optical pumping is performed, the black body radiation as well as spontaneous decays will contribute to transitions between neighboring rotational states. While this means that population in all the higher lying rotational states $J > 2$ will over time decay and also get pumped to the rovibrational ground state, it also means that population will slowly get excited up out of the ground state, through $J = 1$ and up to the $J = 2$ state again. Once in the $J = 2$ state, the population will once again be transferred to the ground state. Thus, the black body radiation both makes the scheme possible and ultimately poses the limitation on its efficiency. It is always possible to add extra lasers to assist the scheme further, for example a laser driving the $|v = 0, J = 4\rangle \rightarrow |v = 1, J = 3\rangle$ transition for pumping from $J = 4$ to $J = 2$ or a laser emptying $J = 1$ to avoid

leaving a 'reservoir' of population in the $J = 1$ state. The scheme may also be assisted by the state selective dissociation of the ns-pulses used for the detection scheme.

4.1.4 Rate equation modeling

To quantitatively analyze and simulate the cooling scheme as well as other potentially interesting rotational dynamics, a numerical model was necessary. Since Rabi oscillations in the laser driven transition(s) will quickly decohere due to spontaneous decays, the processes can all be modeled as incoherent, described by rate equations using the Einstein A and B coefficients.

The transition rate \dot{N}_{ab} from a state b to a state a in the presence of only incoherent radiation can be written (Bransden & Joachain [93] eq. 4.103)

$$\dot{N}_{ab} = A_{ab}N_b + B_{ab}N_b\rho(\omega_{ab}) \quad (4.4)$$

In the case where state b is more energetic than state a , A_{ab} is the Einstein coefficient responsible for spontaneous decay and B_{ab} is responsible for stimulated emission. In the reverse case, $A_{ab} = 0$ and B_{ab} is the coefficient for absorption. In some cases, such as the single temperature case, the energy density $\rho(\omega_{ab})$ is known from Planck's law, equation (4.1), given the energy levels calculated by Balfour [94].

To determine the A coefficients, the ground state molecular dipole moment and potential were calculated as functions of internuclear distance in the program Gaussian [95] and input to the program LEVEL 8.0 [96], returning the Einstein A coefficients for all dipole allowed transitions in the ground state of the MgH⁺ system.

The A coefficients were first calculated in this way by Ivan Vogelius in 2002 [63]. In 2012, I carried out another calculation of the A coefficients based on new potential and dipole moment curves calculated to high precision by Frank Jensen at the Department of Chemistry at Aarhus University. The calculations are presented in section 4.1.5 and the results can be found in appendix B. The A coefficients of Ivan Vogelius have in this thesis only been used in figure 4.2 and figure 6.2. All other simulations in this thesis have been performed with the A coefficients determined in 2012.

The B coefficients are calculated from the A coefficients by (Bransden & Joachain [93] eqs. 4.108b, 4.109)

$$B_{ab} = \frac{\pi^2 c^3}{\hbar \omega_{ab}^3} A_{ab} \quad (4.5)$$

$$g_a B_{ba} = g_b B_{ab} \quad (4.6)$$

where $g = 2J + 1$ is the state degeneracy. With these coefficients, we now have a set of coupled rate equations, each obeying equation (4.4).

To solve this system of equations, we first introduce the population vector \vec{p} containing as elements the populations in each rotational level that is regarded. For the present simulations, we choose to include the first 20 rotational levels of the $v = 0$ and $v = 1$ states in the electronic ground state, so we have

$$\vec{p} = [p_{(0,0)}, p_{(0,1)}, \dots, p_{(0,19)}, p_{(1,0)}, \dots, p_{(1,19)}] \quad (4.7)$$

where $p_{(v,J)}$ denotes the population in state $|v, J\rangle$.

Next, we introduce the coupling matrix \mathbf{K} where

$$K_{ab} = A_{ab} + B_{ab}\rho(\omega_{ab}) \quad (4.8)$$

to write the coupled rate equation in a convenient short form:

$$\frac{d\vec{p}}{dt} = \mathbf{K}\vec{p} \quad (4.9)$$

The solution is given by the matrix exponential:

$$\vec{p}(t) = \exp(\mathbf{K}t)\vec{p}(t=0) \quad (4.10)$$

If Planck's law is used for the radiation energy density distribution, one will reproduce the Boltzmann population distribution once equilibrium is reached regardless of the initial condition $\vec{p}(t=0)$. By adding a contribution to an element in the $[\rho(\omega_{ab})]$ matrix, we simulate the effect of a laser incoherently addressing that transition. The steady state population distribution in the case with no laser is shown along with that of the case with a saturating laser addressing the cooling transition in figure 4.2. The simulations based on the A coefficients determined by Ivan Vogelius in 2002 predict a ground state population in the cooled case of 64%, quite an improvement over the thermal 3%. With the A coefficients calculated in 2012, the equilibrium cooled ground state population is 57%.

With this simulation tool, one can also simulate other aspects of the incoherent rotational and vibrational dynamics of MgH^+ . For example, applying a lamp with a well known spectral distribution or filtering out certain black body radiation wavelength components can be easily simulated by modifying the energy density matrix. One can also determine the expected rate at which

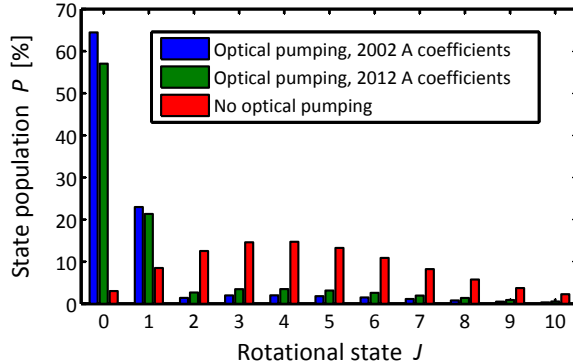


Figure 4.2: Simulated rotational population distributions at room temperature ($T = 297\text{ K}$), with red bars indicating the thermal equilibrium at room temperature and blue and green bars signifying the steady state populations predicted by including rotational cooling using the 2002 and 2012 A coefficients, respectively.

the system reobtains equilibrium after a disturbance such as dissociative state preparation, the complete or partial removal of molecules in a particular rotational state. Simulations and results of dissociative state preparation are presented in chapters 6 and 7.

4.1.5 Determination of the MgH^+ A coefficients

Since the Einstein A coefficients form the cornerstone of the simulations of the radiative vibrational and rotational dynamics, accurate calculations of these coefficients was essential. We use the symbol $A_{(v_i, J_i) \rightarrow (v_f, J_f)}$ to denote the coefficient for decay $|v = 1; J = 1\rangle_X \rightarrow |v = 0; J = 0\rangle_X$.

From knowledge of the potential energy and the permanent dipole moment as a function of internuclear distance in the MgH^+ molecules, *ab initio* A coefficients for all the relevant rovibrational transitions can be calculated using the following method: The rovibrational wave functions of the electronic ground state can be found from the potential energy curve by solving the Schrödinger equation using the Numerov method. From these wave functions and the dipole moment curve of the electronic ground state, the transition dipole moments \mathbf{D}_{ij} can be found, where the upper state is denoted i and the lower state j . Finally,

the Einstein A coefficients are given as

$$A_{ij} = \frac{\omega_{ij}^3 |\mathbf{D}_{ij}|^2}{3g_i c^3 \epsilon_0 \hbar \pi} \quad (4.11)$$

where ω_{ij} is the angular transition frequency and g_i is the degeneracy of the initial, upper state.

Ivan Vogeliuss, at the time a PhD student working with the Ion Trap Group, carried out such calculations on MgH^+ in 2002 [97] using the program *Gaussian* [95] to calculate the potential and dipole moment curves and *LEVEL 8.0* [96] to calculate the wave functions, transition dipole moments and the Einstein A coefficients. These results placed the important $A_{(1,1)\rightarrow(0,0)}$ of the electronic ground state at 7.89 Hz. For these curves, he applied a 6-311++G basis set for various choices of electron correlation modelling, and observing convergence when going to the highest level of theory, the CCSD(T) electron correlation model.

Seeking to re-determine these values with the increased computational power of 2012, we have collaborated with Frank Jensen from the Department of Chemistry at Aarhus University. He performed new high precision calculations in *Gaussian* of the potential curve as well as the permanent dipole moment curve, shown in figure 4.3. He describes in a private communication the calculation procedure as follows: Like in the calculations performed in 2002, the CCSD(T) electron correlation model was used, but this time using uncontracted versions of the aug-cc-pCVXZ ($X = \text{D}, \text{T}, \text{Q}, 5$) basis sets. The relative quality of these basis sets roughly compare as $\text{D} < \text{T} < \text{Q} < 5$, with the 6-311++G basis set used in 2002 being roughly comparable in quality to aug-cc-pCVTZ. Convergence of the diffuse functions was done using a doubly-augmented cc-pCVQZ basis set (outer exponents scaled by a factor of 3), and relativistic effects were estimated by the DKH2 formalism. Extrapolation to the basis set limit was done using an exponential fit to (T,Q,5) data for the HF energy and an L^{-3} fit to (Q,5) data for the correlation energy. Convergence of the CCSD(T) method with respect to increased electron correlation was done using the BD(TQ) method with the aug-pCVDZ and aug-pCVTZ basis sets. Dipole moments were calculated by a double numerical differentiation with respect to an external electric field of 1×10^{-4} au.

LEVEL 8.0 was subsequently used to determine A coefficients based on these curves. To verify that the curves were calculated in a sufficiently broad interval of internuclear distance values and with sufficient density of points, convergence of two representative A coefficient outputs $A_{(1,1)\rightarrow(0,0)}$ and $A_{(4,0)\rightarrow(3,1)}$ calcu-

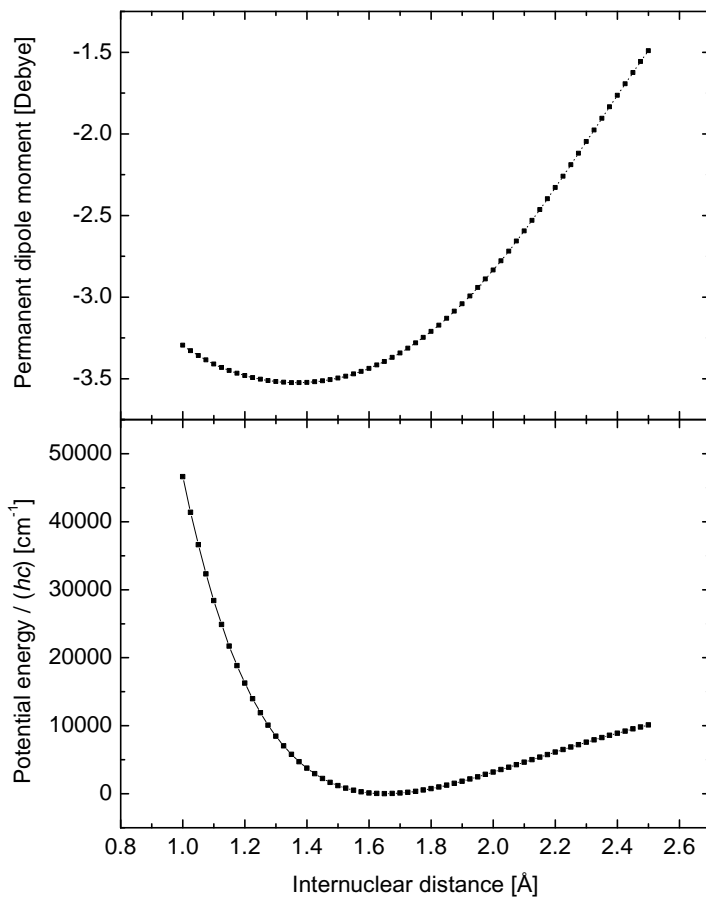


Figure 4.3: The permanent dipole moment and potential energy of the electronic ground state of MgH^+ , calculated at the highest level of theory: the aug-cc-pCVXZ extrapolated basis set, using CCSD(T) electron correlation and using DKH2 formalism for taking relativistic effects into account. For the dipole moment, the choice of origin is the center of mass of the molecule and the positive direction is taken towards the H core. The zero point of potential energy has been defined at the curve minimum.

lated with *LEVEL 8.0* as functions of these parameters was checked on the CCSD(T), aug-cc-pCV5Z curves (figures 4.4, 4.5, 4.6).

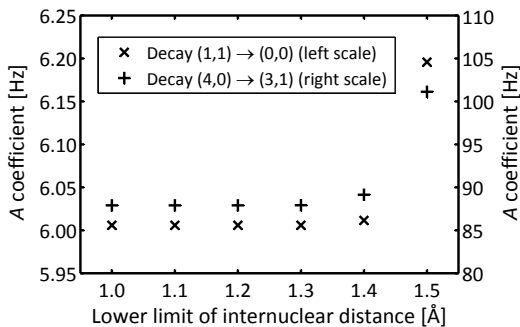


Figure 4.4: The dependence of the two test A coefficient results on the choice of lower limit of the range of internuclear distances used for the potential and dipole moment curves. In all other calculations, the lower limit 1.0 Å was used, $A_{(1,1) \rightarrow (0,0)}$ having converged to well within 0.0001 Hz and $A_{(4,0) \rightarrow (3,1)}$ having converged to well within 0.001 Hz at this value.

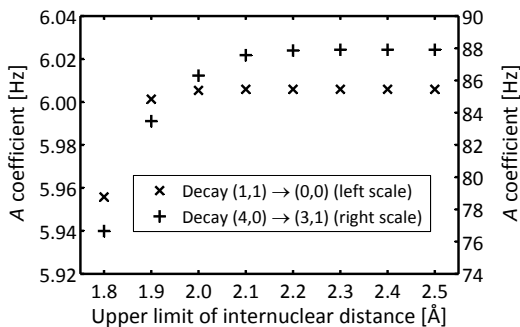


Figure 4.5: The dependence of the two test A coefficient results on the choice of upper limit of the range of internuclear distances used for the potential and dipole moment curves. In all other calculations, the upper limit 2.5 Å was used, $A_{(1,1) \rightarrow (0,0)}$ having converged to well within 0.0001 Hz and $A_{(4,0) \rightarrow (3,1)}$ having converged to well within 0.001 Hz at this value.

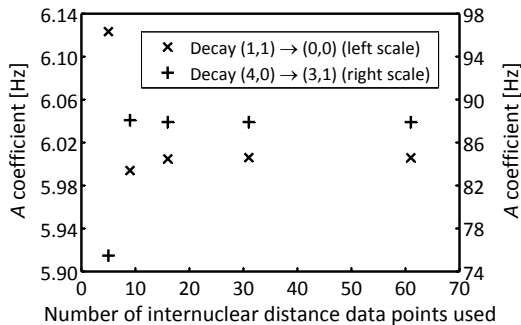


Figure 4.6: The dependence of the two test A coefficient results on the choice of the amount of points calculated between the lower and upper limits of internuclear distances used for the potential and dipole moment curves. In all other calculations, 62 points between 1.0 \AA and 2.5 \AA were used, $A_{(1,1) \rightarrow (0,0)}$ having converged to within 0.0002 Hz and $A_{(4,0) \rightarrow (3,1)}$ having converged to within 0.002 Hz at this number of points.

The A coefficients obtained from the curves in figure 4.3, our highest level of theory, are listed in appendix B. For the purpose of the decay rate measurement of section 7.7, we note that this puts $A_{(1,1) \rightarrow (0,0)} = 6.14 \text{ Hz}$. The estimated total uncertainty on this value is $\sim 0.03 \text{ Hz}$.

4.2 REMPD population measurement scheme for MgH^+

This section concerns itself with the method used for determining the actual rotational population distribution. To directly measure the population in a specific rotational state in the vibronic ground state, we use an implementation of Resonance Enhanced Multi-Photon Dissociation (REMPD). The idea is that if we dissociate molecules rotational state selectively, then the population of each state will be apparent in the reduction of the amount of molecules. We initially employed a single-color dissociation scheme, on which the results published in New Journal of Physics in 2009 were based, but later chose to use a two-color scheme, for reasons I will elaborate on below.

4.2.1 Transitions

In figure 4.7, the four lowest electronic levels of MgH^+ are shown with arrows indicating the relevant transitions of the two different dissociation schemes. In both the single- and two-color schemes, the first step of the REMPD scheme is a resonant transition from $(v = 0, J)$ in the $X^1\Sigma^+$ ground state to $(v = 0, J \pm 1)$ in the $A^1\Sigma^+$ state. This is driven with a laser pulse with a wavelength around 281 nm and a pulse length of ~ 9 ns FWHM.

The second step in the dissociation process, from A to the dissociation continuum of the C state, is performed in the single-color scheme by the same pulse as the first step. Since the coupling strength of the second transition is much lower than that of the first step, the spontaneous decay from A to X is significant in the single-color scheme and must be included in modelling of the process.

In the two-color scheme, the second step is performed with a separate, much more intense pulse with a wavelength of 266 nm, also with a pulse length of about 9 ns FWHM. Compared to the single-color scheme, the much stronger coupling from A to C enables high dissociation efficiencies ($> 90\%$ in early experiments, $\sim 100\%$ in later experiments), greatly diminishing or eliminating the role of spontaneous decay in the process. At the same time, the energy of the 281 nm pulse can be lowered, reducing power-broadening in the X to A transition and enables resolution of the individual lines of all rotational states.

Due to the difference in the rotational constant for the two electronic levels, the energies for the P ($\Delta J = -1$) and R ($\Delta J = +1$) transitions are not equidistantly spaced as would be a good approximation for rovibrational transitions, but will rather form a so-called Fortrat parabola when plotted against $J \cdot \Delta J$ as in figure 4.8.

From $A^1\Sigma^+$, a second laser pulse now takes the population through the non-resonant second step up into the dissociation continuum of the $C^1\Sigma^+$ state. Luckily, the easily produced 266 nm fourth harmonic of our Nd:YAG laser provides a very good wave function overlap between the vibrational ground state in A and the classical turning point of the C curve, resulting in strong coupling. The dissociation product from the C state is a neutral Mg atom and a H^+ ion. The magnesium will escape the trap because it is neutral, and H^+ is much too light to experience a confining effective radial potential. Upon dissociation, both products therefore leave the trap and the amount of non-fluorescent ions will drop suddenly. The 266 nm pulse used for this step is also ~ 9 ns in FWHM duration.

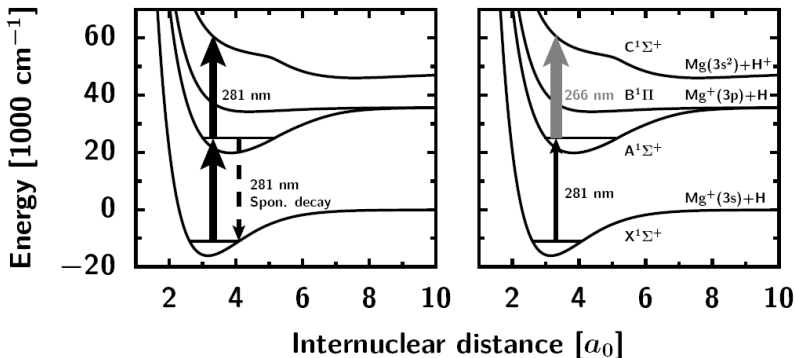


Figure 4.7: From [46]. Potential curves of the four lowest energy electronic states of the MgH^+ system, shown with asymptotic dissociation configurations and transitions of the two different schemes for resonance enhanced multi-photon dissociation. **Left:** The single-color dissociation scheme, in which a single 281 nm pulse is chosen to have sufficient energy to drive both the resonant X to A transition and the transition from A to the dissociation continuum of the C state. **Right:** The two-color dissociation scheme, in which the X to A transition is driven with a less strong pulse than in the single-color scheme, while the A to C transition is driven with a strong 266 nm pulse.

4.2.2 Pulse timing

To maximize the dissociation efficiency, one must avoid spontaneous decays from A back to X, which can happen to a number of vibrational states, causing those molecules to experience a slow (~ 10 Hz) cascade down towards the vibrational ground state. The time scale of this rovibrational cascade is far slower than the pulse duration, so all molecules that decay from A to X will not contribute to the dissociation signal of that REMPD event. The REMPI (Resonant Multi-Photon Ionization) equivalent of this phenomenon was observed in 1980 by Bergmann and Gottwald [98]. To minimize this, we must be aware that at resonance, excitation of the X to A transition will take place significantly already on the leading edge of the 281 nm pulse, rather than exactly at the pulse intensity maximum. Therefore, we choose not to let the 266 nm A to C pulse overlap temporally exactly with the resonant pulse but rather with the expected peak of population in A, which on average is about 3 ns before the intensity peak of the X to A pulse.

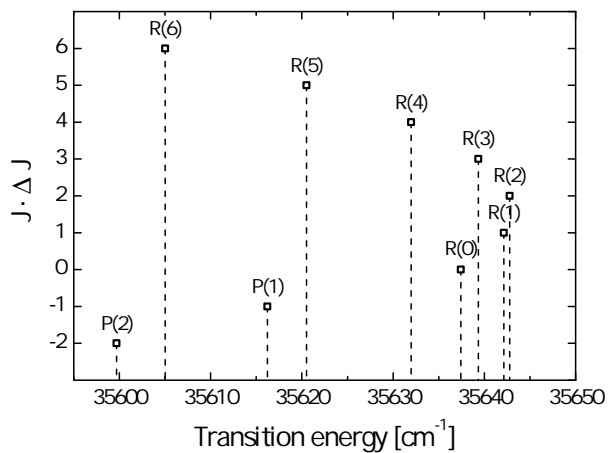


Figure 4.8: The state selectivity in the resonant transition is achieved by tuning the wavelength of the ~ 281 nm pulsed laser onto the relevant line. The symbol $R(J)$ denotes the $\Delta J = +1$ transition from the J state, while $P(J)$ denotes the $\Delta J = -1$ transition from the J state. All lines except $R(1)$ and $R(2)$ can be individually resolved. The population in the $J = 1$ and $J = 2$ states is instead probed using $P(1)$ and $P(2)$.

Chapter 5

Equipment and methods used for the MgH^+ rotational cooling experiments

In this chapter, the laser systems set up specifically for the MgH^+ rotational cooling experiments are introduced. These are the two lasers for driving the vibrational optical pumping transition, an InP diode laser for exciting the near-infrared transition from $|v = 0, J = 1\rangle$ to $|v = 4, J = 0\rangle$ and the pulsed lasers for the REMPD scheme.

I will also lay out the algorithm I wrote for computer analyzing large amounts of bicrystal images to determine the number of molecules in each image frame during the experiment, such that we could accurately track the reduction in trapped molecules caused by the REMPD scheme to determine the population in the addressed state.

5.1 Mid-infrared laser sources

In the previous chapter, I explained the optical pumping scheme that employs mid-infrared radiation for cooling the rotational degree of freedom of the target molecule. In the case of MgH^+ , the transition is known from a 1972 study by Balfour [94] to have an energy corresponding to a vacuum wavelength of 6215.2 nm.

When it was decided around 2006-2007 to order a laser system for producing radiation of this wavelength, the best option available was a PbSe lead salt diode laser. This laser and the associated diagnostics equipment was set up in 2007 by bachelors student Peter Skyt and postdoc Peter Staantum. After the 2009 measurements published in Nature Physics, the power output of the PbSe diode laser gradually degraded and, due to the availability of new quantum cascade lasers in that wavelength region with much higher power output, it was decided to buy such a quantum cascade laser. That laser system was set up by postdoc Alex Gingell in 2011 and has been used thus far for all rotational cooling experiments performed since. Although the PbSe laser output power is low, it can still be used for potential future experiments, such as ones requiring driving two mid-infrared transitions simultaneously.

5.1.1 The PbSe diode laser setup

The diode laser system was manufactured by Laser Components GmbH to lase at the specific wavelength requested, 6215.2 nm, given appropriate operating conditions. The laser is specified to operate with diode currents up to 350 mA and under temperatures up to 103 K. Cooling the diode down with the use of a liquid nitrogen dewar (N_2 boiling point 77 K) was therefore required. A picture of the final PbSe setup is shown in figure 5.1 and figure 5.2 contains a sketch of the setup.

The laser was supplied with a controller unit, regulating the temperature of the diode as well as the diode current with an optional current modulation. The laser exhibits a large amount of mode jumps in its region of operation and, in general, some tweaking of the diode temperature and current is necessary to obtain stable single mode operation at the desired wavelength. Testing determined that the lasing range was 6154 nm to 6270 nm.

To tune the laser to the required wavelength, a monochromator is used for coarse wavelength determination along with an ammonia (NH_3) absorption cell for fine absolute wavelength reference. Additionally, a germanium etalon with a free spectral range corresponding to 0.0486 cm^{-1} wavenumbers provides relative frequency reference. A suitable ammonia absorption line was located at 6214.8 nm, close to the MgH^+ resonance at 6215.2 nm. Graphs illustrating the etalon transmission and spectroscopy are shown in figure 5.3. Calibrating the dependence of lasing frequency on the diode current, $\frac{d\nu}{dI}$, the necessary current shift from the ammonia peak to the MgH^+ resonance was calculated. Based on $\frac{d\nu}{dI}$, a current modulation of 0.3 mA was chosen to increase the effective laser line width enough to ensure that the laser would not drift off resonance while keeping the spectral energy density ρ high enough to saturate the cooling transition during the experiments. The PbSe laser has so far only been used in the room temperature chamber where the laser beam was shaped into an intensity profile with a horizontal FWHM of 3.2 mm and a vertical FWHM of 0.9 mm, enough to illuminate Coulomb crystals of the sizes used in the experiments.

At the time of the measurements made for the Nature Physics article, the power at the ions was about $44 \mu\text{W}$, which is enough to saturate the optical pumping transition for all orientations of the molecule, if the polarization is scrambled on a time scale faster than the life time of the $|v = 1, J = 1\rangle$ level. In the experiments, the polarization was scrambled on a time scale of 4 Hz.

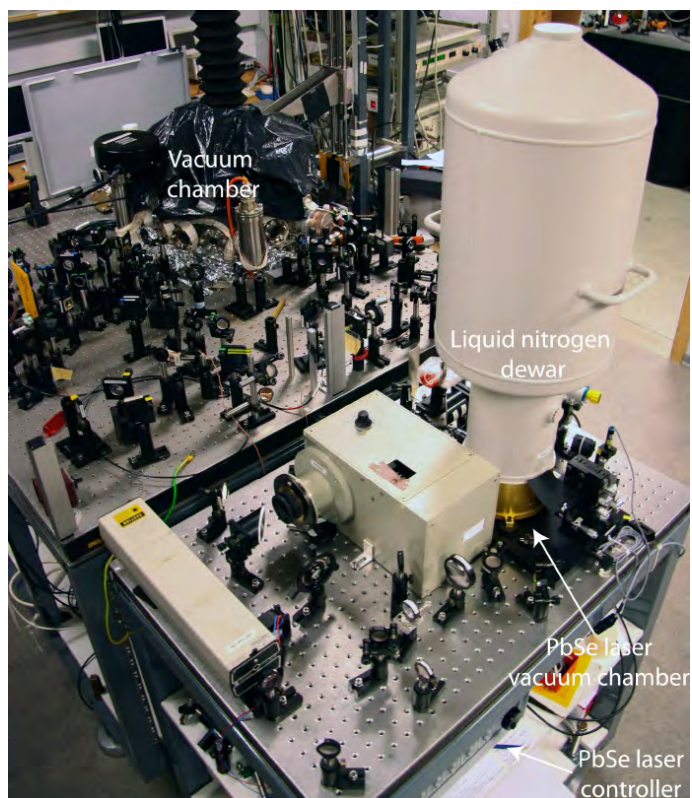


Figure 5.1: From [99]. A photograph of the finished PbSe diode laser setup. The diode is inside a small vacuum chamber underneath the gray liquid nitrogen dewar. On the PbSe optical table is also a He-Ne laser for alignment of the mid-infrared beam, a monochromator for coarse wavelength determination, an ammonia absorption cell and a fast mercury cadmium telluride (HgCdTe) detector. The absorption cell and fast detector are behind the dewar in this photo.

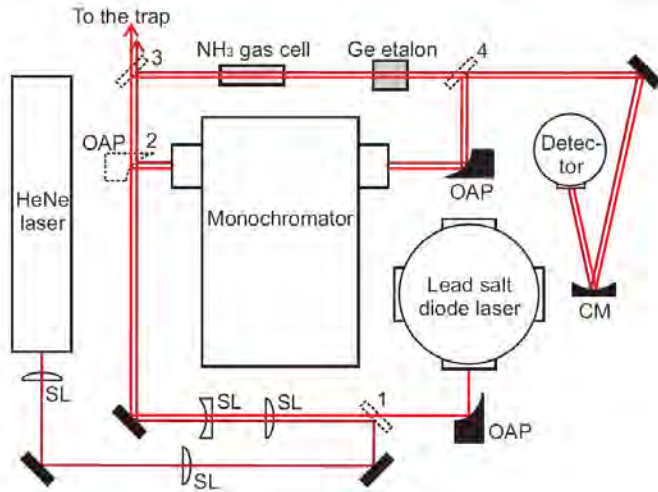


Figure 5.2: From [99]. A sketch of the finished PbSe diode laser setup. SL: Spherical lens, OAP: Off-axis parabolic mirror. The optical elements in dashed lines signify flip mirror optics. Flip mirror 1 is for using the He-Ne laser for easier alignment of the beam path. Flip mirrors 2 and 4 are for using the monochromator. The third flip mirror sends the beam to the absorption spectroscopy.

5.1.2 The Quantum Cascade laser setup

Because of the great advances in the capabilities and affordability of quantum cascade lasers (QCLs) in the years during and after the construction of the PbSe diode laser, a QCL was ordered from the laser company Daylight Solutions to supplement the existing PbSe diode laser setup. This laser system was set up by postdoc Alex Gingell in 2011. A photo of the finished setup alongside the PbSe setup is shown in figure 5.4.

For a sketch of the configuration of the QCL laser, see figure 5.5. A ThermoCube recirculating chiller was set up to provide cooling of the base plate inside the QCL laser head. As in the case of the PbSe diode laser, a controller unit is included, enabling adjustment of the QCL chip current, the temperature setpoint of the chip and coarse wavelength selection by mechanical rotation of the grating. Inputs are further provided for tuning and modulating the wavelength by current modulation and offsetting/modulating the voltage applied to a

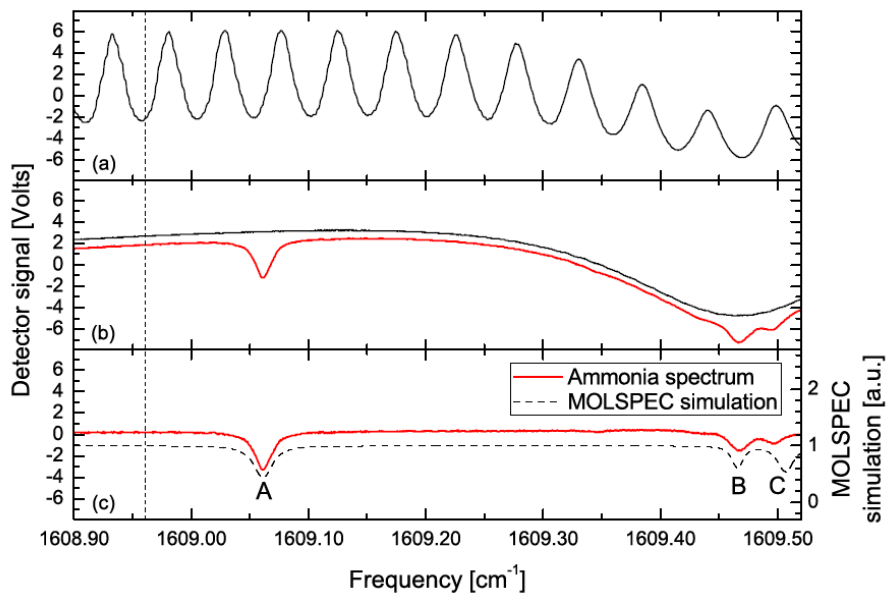


Figure 5.3: From [99]. The spectroscopy used to reach the MgH^+ resonance. Absolute and relative calibration has been applied to convert the horizontal axis from current to wavenumber. The vertical dashed line shows the position of the MgH^+ resonance. Top trace: The transmission through the germanium etalon, providing relative reference. Middle traces: Black shows the reference absorption trace where only air absorption is present, while red shows the total absorption trace after insertion of the ammonia gas cell. In both traces, a broad water line dominates in the right end of the spectrum. Bottom traces: Red shows the difference between the two middle traces, showing only the ammonia absorption contribution, and the dashed line is the result of an absorption simulation carried out in the computer program MOLSPEC.

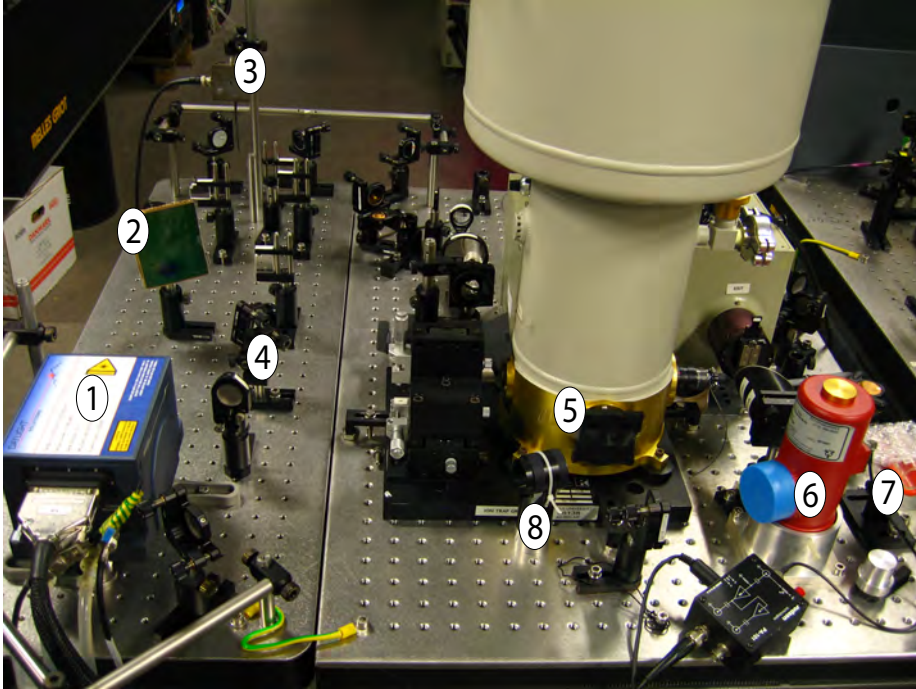


Figure 5.4: A photograph of the finished QCL and PbSe diode laser setups. 1: QCL laser head. 2: Temperature sensitive liquid crystal sheet blocking the emitted laser beam, causing a color change from green to blue. 3: Flag shutter for fast control of laser admittance to the experiment. 4: Magnetic mount mirror sending the beam to the cryogenic chamber table, easily removable to send the beam to either diagnostics or the room temperature trap. 5: PbSe diode laser chamber. 6: HgCdTe mid-infrared detector. 7: NH_3 absorption cell. 8: Ge etalon. In addition to the numbered elements, four cylindrical lenses are placed on the table to shape the QCL beam.

PZT on which the grating is mounted. The PZT can be used for slow (< 100 Hz) modulation and for fine offset, corresponding to $\sim 1.4 \text{ cm}^{-1}$ wavenumbers for the full 100 V PZT range. The current modulation (between 10 kHz and 2 MHz) is fast but is AC coupled and thus cannot be used for offsetting the laser wavelength.

The same diagnostics beampaths are used for the QCL as for the PbSe

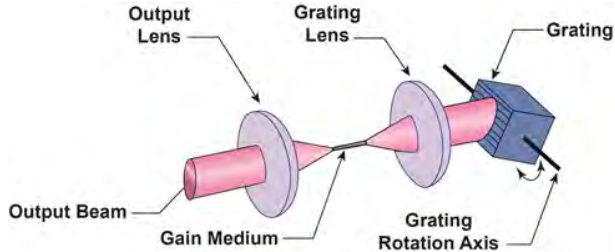


Figure 5.5: From [100], 2012. A sketch of the optics configuration used for QCLs by Daylight Solutions. The grating angle is controlled both with coarse mechanical rotation and with fine PZT adjustment.

diode laser, enabling relative and absolute reference with the germanium etalon, monochromator and absorption cell. With the chip temperature and current set to suitable fixed values, PZT modulation and offset are used to identify the ammonia absorption peak labeled A in figure 5.3 and to detune from there to the MgH^+ resonance based on a $\frac{d\nu}{dV}$ calibration. Then with the PZT modulation amplitude turned to zero, a sinusoidal current modulation at 400 kHz is activated, broadening the effective FWHM laser line width to approximately 0.05 cm^{-1} , which is above the measured long term drift of the laser while still low enough to saturate the optical pumping transition at the typical laser output power of 60 mW.

The $D4\sigma$ beam width for the QCL assisted (post-Nature Physics article) measurements in the room temperature trap was $2.43 \text{ mm} \times 1.70 \text{ mm}$ (horizontal \times vertical). For the cryogenic chamber experiments with the QCL beam entering axially, the $D4\sigma$ beam width was $3.4 \text{ mm} \times 1.6 \text{ mm}$. For the cryogenic chamber experiments with the QCL entering at an angle of 67.5° to the trap axis, the beam fully illuminated the space between the electrodes, corresponding to a beam width of roughly $4 \text{ mm} \times 2.6 \text{ mm}$.

The QCL can lase in the wavelength range $5.73 \mu\text{m}$ to $6.31 \mu\text{m}$ and mode-hop free operation is specified within the $5.93 \mu\text{m}$ to $6.19 \mu\text{m}$ range. The full tuning range enables addressing the MgH^+ transitions $R_1(0 \text{ to } 9)$ and $P_1(1 \text{ to } 3)$, where the subscript 1 implies $\Delta v = 1$, the number in the parenthesis is the initial rotational quantum number J and R and P denote whether ΔJ is plus or minus one, respectively.

5.2 Near-infrared InP diode laser

As an addition to the mid-infrared sources presented in the previous sections, an indium phosphide (InP) diode laser intended to address transitions of the type $|v = 0, J\rangle \rightarrow |v = 4, J \pm 1\rangle$ was set up. Peter Skyt [99] started constructing the laser around 2008 and it has since been worked on by several others, including Simon Kristensen [101]. It can reach wavelengths within the region 1625 nm to 1660 nm, corresponding to transitions $R_4(0)$, $R_4(1)$ and $P_4(1 \text{ to } 6)$.

Using rate equation modelling, a variety of different equilibrium state distributions have been predicted when combining the InP diode laser with one or both of the mid-infrared sources. For details on these possibilities, see the master's theses by Peter Skyt and Simon Kristensen. The laser typically delivers up to 3 mW in single-mode operation. It has not yet been taken in use in experiments. A photo of the laser without its insulating polystyrene housing is shown in figure 5.6.

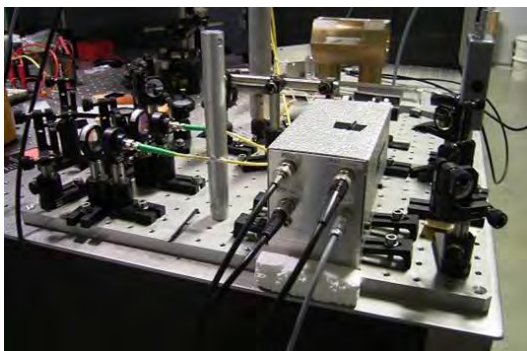


Figure 5.6: A photograph of the indium phosphide laser set up to address transitions from $v = 0$ to $v = 4$ in MgH^+ .

5.3 Nanosecond pulse laser sources

For the REMPD schemes, it is necessary to induce fast dynamics in the molecule. Specifically, the transitions into the dissociation continuum have to be faster than the spontaneous decay rate from A to X, which is on the order of 10 ns. To drive the transitions as strongly as possible within that timeframe, we use

nanosecond pulses produced by Q-switched Nd:YAG lasers and a pulsed Sirah dye laser. A sketch of the setup of the pulsed lasers is shown in figure 5.7.

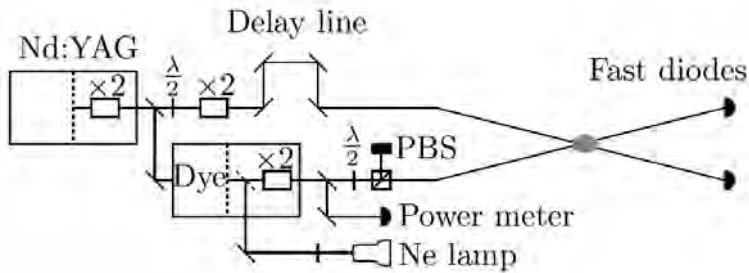


Figure 5.7: From [46]. A sketch of the pulsed laser setup. 1064 nm light from the Nd:YAG undergoes frequency doubling to 532 nm and is split in two, with one arm pumping the dye laser and the other arm being further frequency doubled to produce 266 nm light. A small component of the ~ 562 nm output of the dye laser can be referenced to optogalvanic spectroscopy carried out with a neon hollow cathode lamp. The rest of the dye laser output is frequency doubled to ~ 281 nm and variably attenuated in a polarizing beam splitter (PBS) before reaching the ions. A delay line in the 266 nm path ensures proper timing between the two ultraviolet pulses. Two fast photodiodes monitor the pulses after they exit the vacuum chamber again.

5.3.1 Nd:YAG lasers

Until 2012, the role of the Nd:YAG laser in the setup was fulfilled by a Q-switched Quantel Nd:YAG laser with a repetition rate of 10 Hz on loan from Prof. Moshe Shapiro, who is currently at the University of British Columbia, Canada.

In 2010, a Spectra Physics Quanta-Ray PRO 270-30 Q-switched Nd:YAG laser with a repetition rate of 30 Hz was installed to supplement the Quantel laser. Various technical difficulties with the Quanta-Ray laser along with the inability of the Sirah pulsed dye laser to operate stably at 30 Hz postponed the use of this laser for experiments until after the technical problems had been fixed and the repetition rate changed to 10 Hz, making the laser a Quanta-Ray PRO 270-10 laser. These final adjustments were done in 2012, at which point it took over the role of the Nd:YAG laser in the figure 5.7 setup.

5.3.2 The Sirah pulsed dye laser

Installed december 2008, the Sirah Cobra-Stretch dye laser uses Rhodamine 6G in methanol as dye and consists of an oscillator, preamplifier and an amplifier stage. Wavelength tuning is performed by rotating a grating in the oscillator with a stepper motor. Upon adjusting the wavelength, the stepper motor wavelength reproducibility of the produced 562 nm light is ~ 5 pm ($\sim 10^{-5}$). This is the value specified by Sirah and has been verified in our lab using optogalvanic spectroscopy in a Ne hollow cathode lamp. The $\sim 10^{-5}$ level is also roughly the magnitude of change one would expect from changes in the refractive index of air due to natural variation of ambient air pressure and ambient humidity. From the optogalvanic spectroscopy it can be seen that as long as the stepper motor is not moving, the wavelength will remain stable to much less than 5 pm on a time scale of hours.

5.4 Determining the number of molecules

Knowing the actual number of molecular ions in a bicrystal such as the one in figure 2.8 as a function of time is necessary to obtain a quantitative measure of the dissociation process that serves to probe the rotational state populations. Besides for dissociation, a bicrystal analysis tool would likely prove generally useful in other types of Coulomb crystal experiments in the future. As one of my first tasks within the group, I programmed such a tool in LabVIEW to calculate the absolute number of fluorescent and non-fluorescent ions from a series of the 2D projection fluorescence images of any bicrystal recorded by the CCD camera of the type in figure 2.8. Note that this requires the non-fluorescent species to be heavier, such that they gather at higher radial distance to the axis than the fluorescent component.

Since the analysis routine has formed the cornerstone of the data analysis in the ensemble rotational cooling experiments, I will explain the program in detail in this section. However, before I go into the computational steps, it is worthwhile to take a look at the theoretical considerations that justify the approximations that I will make.

5.4.1 Theoretical considerations

As I wrote in the section on the ion trap, the pseudopotential generated in the absence of space charges can be written $\phi_{\text{ps}}(r, z) = \frac{1}{2}M(\omega_z^2 z^2 + \omega_r^2 r^2)$. When

the trap is loaded with a one-component Coulomb crystal, the form that is assumed is spheroidal but due to space charge effects does not quite correspond to an equipotential surface in the above potential. Introducing the aspect ratio α of such a crystal as the ratio of the radial semidiameter R to the axial semidiameter (half-length) $\frac{L}{2}$, the volume of a single component crystal can be written as the volume of a spheroid

$$V = \frac{4}{3}\pi R^2 \frac{L}{2} = \frac{1}{6}\pi\alpha^2 L^3 \quad (5.1)$$

Since the difference in charge to mass ratio of $^{24}\text{Mg}^+$ and $^{24}\text{MgH}^+$ is only one in 24, the outer boundary of a bicrystal of those two components can be approximated by a spheroid of the same aspect ratio as the single-component Mg^+ crystal [102].

The density ρ_0 of any particular ion species is constant throughout the crystal [71] and, using the symbol conventions of the section on the ion trap, given by

$$\rho_0 = \frac{\epsilon_0 U_{\text{rf}}^2}{M r_0^4 \omega_{\text{rf}}^2} \quad (5.2)$$

Due to the difference in charge density inside the two components, an inter-component separation appears in bicrystals. The separation in $\text{Mg}^+ + \text{MgH}^+$ can be expressed as the difference $r_{\text{MgH}^+} - r_{\text{Mg}^+}$, where r_{MgH^+} is the radius of the inner MgH^+ ion shell minus half a shell width and r_{Mg^+} is the radius of the outer Mg^+ ion shell plus half a shell width. The ratio of these radii is $r_{\text{MgH}^+}/r_{\text{Mg}^+} = \sqrt{M_{\text{MgH}^+}/M_{\text{Mg}^+}} = 0,98$ [102]. In other words, the separation between these two ion species, with a mass difference of only 1 amu, is only 2% of the inner component radius. This phenomenon is also neglected in our considerations of the crystal structure. Thus, given knowledge of L and α , one can easily determine the total volume occupied by the entire bicrystal by equation 5.1.

5.4.2 Analysis procedure

In this section, I will explain the calculations for extracting the number of ions of each species step by step. The computational steps are represented schematically in figure 5.9. Recall that the Mg^+ ions fluoresce when exposed to the Doppler cooling light, while the MgH^+ ions do not and appear only as 'dark' ions around the lighter Mg^+ .

After having recorded and saved the series of images of the bicrystal, these images are imported into the LabVIEW program and converted to two-dimensional

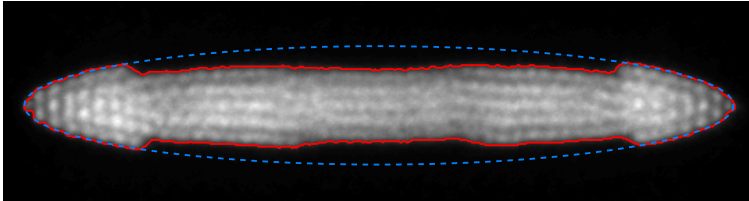


Figure 5.8: The bicrystal of figure 2.8 overlaid with a red border signifying the boundary between pixels above threshold and pixels below threshold. The outer boundary of the whole crystal is indicated by the dashed blue ellipse. The trap symmetry axis is horizontal in the image.

arrays of grayscale intensities. For each image, the following steps are now performed: The characteristic background intensity I_b is determined as the average of intensities in a 10 pixel x 10 pixel area in the upper left corner and the characteristic crystal intensity I_c as the average of intensities in a user specified 10 pixel x 10 pixel area inside the crystal. An intensity threshold I_t is now defined as $I_t = I_b + T(I_c - I_b)$, where T is a user specified threshold value between 0 and 1. For the duration of the Nature Physics experiments, $T = 35\%$ was chosen for our crystal images to most accurately reproduce the crystal boundary corresponding to half a shell widths distance from the outermost fluorescing ions. For subsequent experiments, the threshold was lowered to 30% to reflect changes in response of the image intensifier due to aging. Figure 5.8 illustrates the threshold principle.

The volume V_f in cubic pixels occupied by fluorescing ions is found using the cylinder symmetry of the crystal by the following method: For each column i of pixels, the crystal diameter d_i in pixels is determined as the amount of above-threshold pixels in that column, and the contribution to V_f in cubic pixels from that column is simply $\frac{\pi}{4}d_i^2$ due to the column width of one pixel. We then have

$$V_f = \frac{\pi}{4} \sum_i d_i^2 \quad (5.3)$$

The crystal length L in pixels is now independently found simply as the number of image columns containing 5 or more pixels above threshold. The requirement of 5 pixels was again chosen to best reproduce the correct outer shell width while also serving to avoid counting columns with only a few pixels of background noise above threshold. From equations 5.1 and 5.3 we can now find α from an image of a one-component crystal in the series as $\alpha = \sqrt{\frac{6V}{\pi L^3}}$

by setting $V = V_f$. Then, once α has been determined, one can find V for all subsequent images containing two-component crystals. Finally, the volume occupied by non-fluorescent ions is found simply as the difference $V_{\text{nf}} = V - V_f$.

We have thus determined the volumes occupied by the fluorescent and the heavier non-fluorescent ion species in the crystal. Since they are at this point still known only in cubic pixels, they are multiplied with a calibration of the imaging system as well as the density (equation 5.2) of the ion species in question, both user specified. The result is the actual number of ions of each species residing in the crystal for each image.

In the two color REMPD scheme used in the following chapters, we dissociate a certain fraction of the molecules in the bicrystal at a point in time and need a way to measure this fraction. Since the dissociation products escape the trap, these molecules are seen to disappear from one image to the next. With the bicrystal analysis tool, determining the fraction is easy. Using N_a for the amount of molecules after the event and N_b for the amount before the event, the fraction is given as $\frac{N_b - N_a}{N_b}$. To determine this drop accurately, N_a and N_b are calculated as averages over a number of frames each, typically 50.

In the single color REMPD scheme, the dissociation takes place over a few minutes and follows an approximately exponential decay. To quantify this dissociation rate constant, the analysis program can perform an exponential decay fit to the data and display the resulting rate constant.

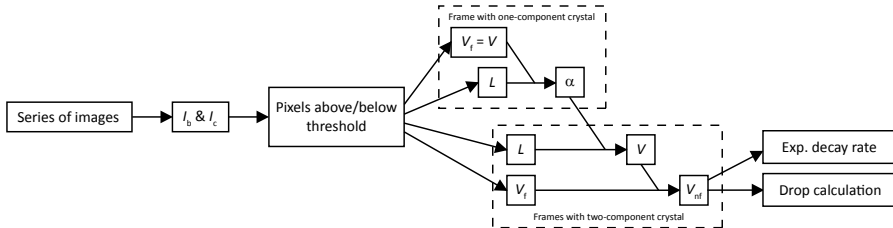


Figure 5.9: Flow diagram for the calculatory steps in the bicrystal analysis program. I_b : Characteristic background intensity, I_c : Characteristic crystal intensity, L : Crystal length, V : Total crystal volume, V_f : Volume of fluorescent component, V_{nf} : Volume of non-fluorescent component, α : Crystal aspect ratio.

Rotational cooling and state preparation of MgH^+ in a room temperature trap

Having introduced the method for preparing translationally cold MgH^+ ions in our ion trap in section 2.2.5 and covered the theoretical aspects of rotational cooling and REMPD state distribution measurements in section 4.2, the stage is set for the experimental rotational cooling results. We published an article in a special issue of *New J. Phys.* [103] while we were still pursuing single color REMPD in the room temperature measurements. Soon after this publication, we tested the two color REMPD scheme and decided to switch to this scheme due to the great simplification it offered in interpretation of the measurements. Upon completion of the measurements with the two color REMPD scheme, the results were published in the April 2010 issue of *Nature Physics* [104]. Similar results of rotational cooling from S. Schillers group [105] at Heinrich-Heine-Universität in Düsseldorf performed with HD^+ molecules were also published in the same issue of *Nature Physics*.

6.1 Method

The principles of the method have all been presented previously in the thesis, but here they are gathered together and laid out for clarity and reference. The steps involved in making the rotational distribution measurements are the following:

1. Starting with an empty ion trap, the shutter blocking the atomic Mg beam inside the vacuum chamber is moved to admit a beam of Mg atoms through the trap center.
2. The photoionizing beam at 285 nm is admitted to the trap center, intersecting the atomic beam at a right angle. This creates hot trapped Mg^+ ions.
3. At all times, the Doppler cooling light at 280 nm also passes through the trap center, cooling the Mg^+ ions down to millikelvin temperatures within milliseconds. The ions undergo a phase transition to a Coulomb crystal. The imaging system provides real time observation of the fluorescence emitted by the ions.

4. Once the desired crystal size is obtained, the ion loading process is stopped by blocking the photoionizing beam and the atomic beam.
5. At this point, images are saved to a hard drive to serve as a reference from which to calculate the crystal aspect ratio α from the single-component crystal.
6. The reaction is started. This is done by introducing hydrogen and reducing the detuning of the Doppler cooling beam to maximize the excitation rate of the Mg^+ ions.
7. Once the desired fraction of atoms have reacted, the reaction is stopped by halting the hydrogen flow and detuning the Doppler cooling laser.
8. The rotational cooling laser source may now either be blocked or unblocked, depending on whether a cooling or non-cooling measurement is made. We wait two minutes for rotational equilibration to occur.
9.
 - a For the single color REMPD, the pulsed 281 nm beam is unblocked and left unblocked until all molecules are dissociated.
 - b For the two color REMPD, two shutters blocking the two pulsed beams are simultaneously triggered to open for a single ns-pulse each, exposing the ions to a single pair of pulses.
10.
 - a For the single color REMPD, no more molecules are present, so the sequence of images is saved and analyzed.
 - b For the two color REMPD, further measurements can be made given time for reequilibration after each REMPD event. Once most molecules have been dissociated, the sequence is saved and analyzed.

6.2 Ensemble state distribution measurements

Preliminary measurements of the effect of the rotational laser cooling scheme on the rotational distribution were first made using the single color REMPD scheme. This method formed the basis for the results published in *New Journal of Physics* in 2009.

Soon after, we switched to two color dissociation and proceeded to take the measurements published in *Nature Physics* in 2010. The rotational cooling laser source used for all experiments in this section was the lead salt PbSe diode laser introduced in section 5.1.1.

6.2.1 Single color dissociation

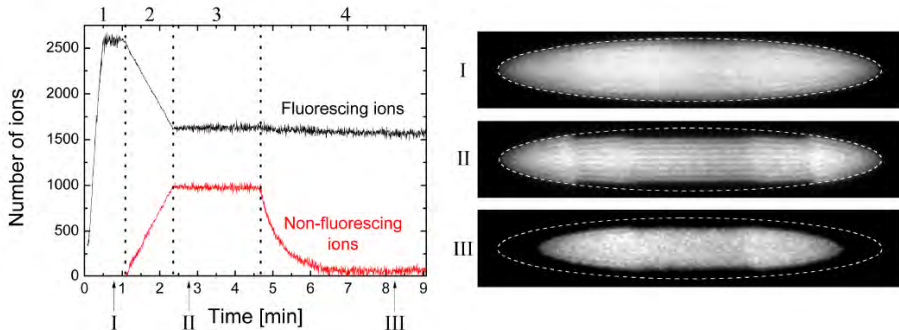


Figure 6.1: A plot of the number of fluorescent and non-fluorescent ions during a single color REMPd measurement. The fluorescent ions are $^{24}\text{Mg}^+$ and the non-fluorescing ions are $^{24}\text{MgH}^+$. The regions 1–4 correspond to the phases loading, reaction, equilibration and dissociation. The images I, II and III are snapshots of the Coulomb crystal at the times indicated on the graph. The outer boundary of the crystal at the end of phase 1 is shown with the dashed ellipse in all three images.

A trace of the number of Mg^+ and MgH^+ ions over the course of a single color REMPd measurement is shown in figure 6.1. The decay in the amount of molecules in general contains two characteristic time scales: A rapid component due to dissociation of the initial population in the addressed rotational state and a slow component characteristic of the $\text{A} \rightarrow \text{X}$ redistribution cascade and rotational mixing. The function

$$N_{\text{nf}} = N_{\text{r}}e^{-\Gamma_{\text{r}}t} + N_{\text{s}}e^{-\Gamma_{\text{s}}t} + \Gamma_{\text{i}}t \quad (6.1)$$

is fitted to the number of molecular (non-fluorescent) ions in region 4. Subscript r denotes a rapid component, subscript s denotes a slow component and subscript i denotes the contribution from ionization of residual gas molecules due to the pulsed beam.

To keep power broadening of the dissociation signal low, the intensity of the pulsed beam was kept so low that the rapid component is rarely distinguishable in the traces. For this reason, only Γ_{s} is considered in the following analysis.

Klaus Højbjerg carried out simulations of the expected values of Γ_{s} as the frequency of the pulsed laser was scanned over the dissociation lines from the

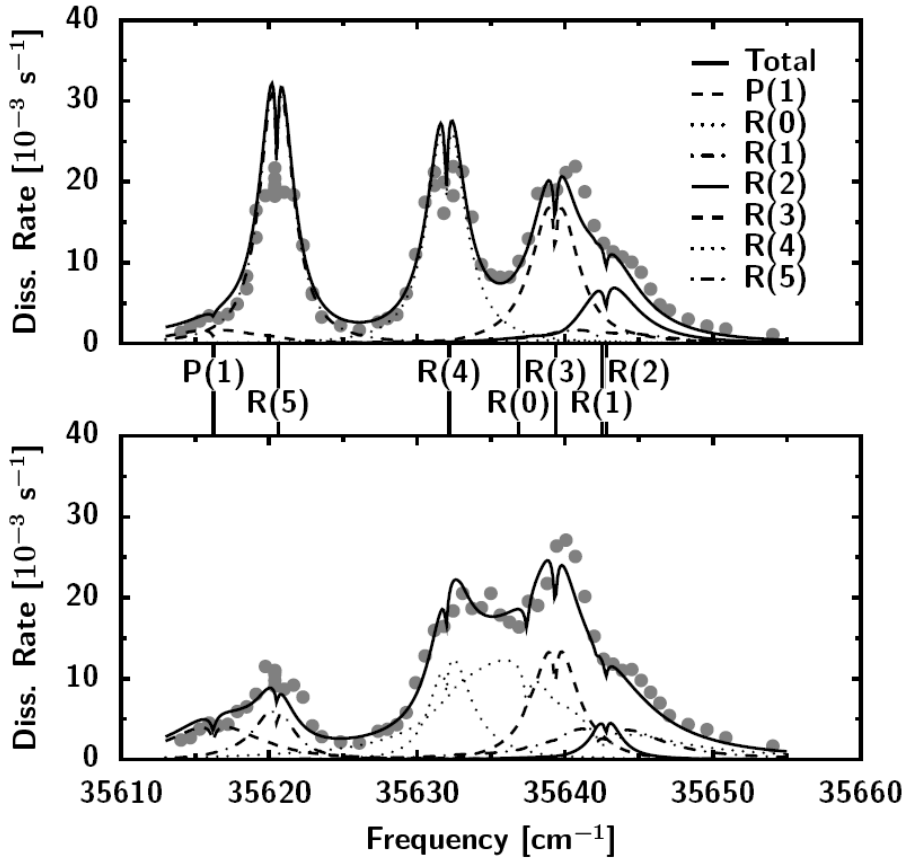


Figure 6.2: From [46]. Graphs of experimental and simulation results of Γ_s for the single color REMPD measurements in the room temperature trap. The top dissociation spectra are without cooling, while the bottom spectra are with cooling. The solid black curve is the simulation prediction of the dissociation rate, with the contributions from the various dissociation lines shown as well in dotted/dashed curves. There is a clear difference in the two spectra, which in the simulations arise from the very large difference in $J = 0$ population. This signature is, however, not immediately obvious due to the width of the R(0) line.

$J = 0-5$ states in the presence and in the absence of the rotational cooling laser. The simulations were carried out based on the A coefficients for MgH^+ calculated in 2002. For more details, see the Ph.D. thesis of Klaus Højbjerg [46]. The experimental data points are presented along with the simulation results in figure 6.2.

A clear difference is apparent between the two spectra, mainly that the cooled spectrum exhibits higher dissociation rates around $R(0)$ and lower dissociation rates at $R(5)$, as one might expect from a shift of equilibrium population distribution towards the low J values. This is supported by the theoretical prediction, which also illustrates just how much greater the $R(0)$ dissociation contribution is expected to be in the cooled case.

Although the signature of rotational cooling is evident in the single color dissociation scheme, the simulations inevitably rely on the complex interplay of electronic, vibrational, rotational and laser induced dynamics working on many different time scales. It is difficult to estimate all the relevant parameters ($A \rightarrow C$ coupling strength, Franck-Condon factors etc.) and model all of the dynamics faithfully, so the two color scheme was pursued in order to simplify the considerations drastically.

6.2.2 Two color dissociation

The addition of a pulsed beam at 266 nm allowed much greater excitation rate on the $A \rightarrow C$ transition while allowing the 281 nm pulse intensity to be significantly lowered, reducing power broadening of the dissociation lines. The 281 nm beam had a spot size of $0.62 \mu\text{m} \times 1.28 \mu\text{m}$ (horizontal \times vertical) and a pulse energy of 5 μJ , while the 266 nm beam was $0.43 \mu\text{m} \times 0.45 \mu\text{m}$ in spot size with a pulse energy of 1 mJ. The pulse timing was such that the 266 nm pulse arrived 3.4 ns before the 281 nm pulse. As I will illustrate in a moment, these REMPD parameters result in dissociation of about 90 % of the molecules in a specific rotational state using only a single pair of pulses when addressing the R transition resonantly. For this reason, only a single pair of pulses is necessary for one measurement of a rotational state's population.

Figure 6.3 depicts the numbers of Mg^+ and MgH^+ ions over the course of a two color REMPD measurement, alongside images of the Coulomb crystal at various points during the measurement. From such a trace, the fractional loss of molecules at each REMPD event can easily be determined.

With the reduced pulse energy of the 281 nm laser, the dissociation lines (figure 4.8) can all be individually resolved with the exception of $R(1)$ and $R(2)$, which are too close together to be resolved considering the spectral line

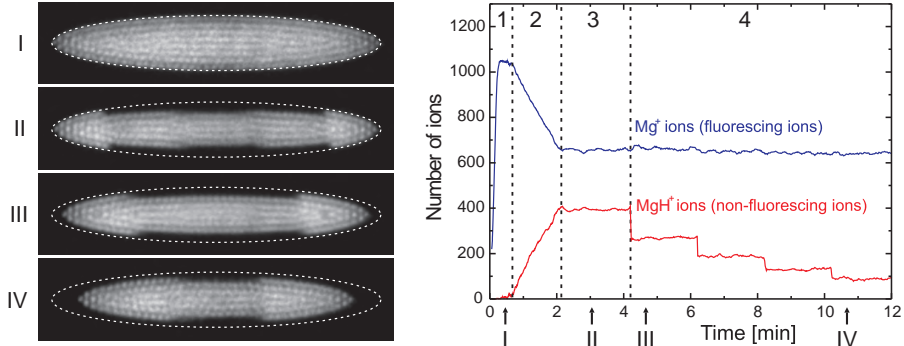


Figure 6.3: Graphs of the number of Mg^+ and MgH^+ ions during a two color REMPD measurement in the room temperature trap. As in figure 6.1, the regions 1–4 are the loading, reaction, equilibration and dissociation phases. An important difference to the single color case is that several independent population measurements can be made on the same crystal given appropriate reequilibration time (2 min). In this case, four independent measurements are performed. Four snapshots of the Coulomb crystal are also shown, with the outer boundary of the crystal at the end of the loading phase indicated with the dashed ellipse.

width of the pulsed dye laser. While all the other rotational state populations are probed using their R dissociation lines, the $J = 1, 2$ states are probed using their P lines. When dissociating through a P line, one must take into account the fact that the linearly polarized light of the 281 nm beam will only probe $2J - 1$ out of $2J + 1$ magnetic substates. For measurements based on P lines, a correction factor $\frac{2J+1}{2J-1}$ is therefore applied after subtraction of the off-resonant contribution.

Denoting the fractional loss of molecules in a dissociation event S , we model the relation between S and the population p in the addressed state as

$$S = \beta\eta p + S_0 \quad (6.2)$$

with

$$\beta = \begin{cases} 1 & \text{for R transitions} \\ \frac{2J-1}{2J+1} & \text{for P transitions} \end{cases} \quad (6.3)$$

where η is the dissociation efficiency, β is the magnetic substate correction factor

and S_0 is a two photon $X \rightarrow C$ excitation contribution induced by the 266 nm pulse. S_0 was measured to be 0.81 % for the cooled distribution and 1.37 % for the uncooled distribution.

As will be justified in a moment, it is a fair assumption that the dissociation efficiency η is independent of the addressed rotational state and furthermore that the rotational distribution without the rotational cooling laser corresponds to a Boltzmann distribution of temperature 297 K. Since data were gathered on the states $J = 0-10$, with $J = 1, 2$ addressed through their P lines, η can be determined from the uncooled distribution as

$$\eta = \frac{\sum_{J=0-10} (S - S_0)/\beta}{\sum_{J=0-10} p} \quad (6.4)$$

which is 87.0 %.

We are now in a position to present the main result of the chapter. The rotational state distributions in the room temperature trap with and without the rotational laser cooling induced by the lead salt PbSe diode laser are shown in figure 6.4.

The two color REMPD scheme thus provides a much more direct measurement of the populations in the individual states than the single color scheme. The excellent agreement between the uncooled distribution and the theoretical Boltzmann distribution for a constant temperature of 297 K, room temperature, demonstrates the validity of the probing scheme, suggesting a dissociation efficiency of 87.0 % that is roughly constant across all rotational states.

Applying the rotational cooling laser results in an equilibrium ground state population of 42 ± 2 % and a $J = 1$ state population of 17 ± 2 %. The ground state population is thus improved by a factor of 14 compared to the uncooled case and corresponds to that of a thermal distribution of 18 ± 2 K.

6.2.3 Characterization of systematic effects

Investigations were made of a variety of potential systematic effects that might affect the result. To verify that the cooling transition $|v = 0, J = 2\rangle \rightarrow |v = 1, J = 1\rangle$ was saturated, the equilibrium ground state population was measured at reduced powers of the PbSe diode laser beam used in these experiments. These results are shown in figure 6.5. It is clear that the transition is saturated at the applied power, 44 μ W, corresponding to 5.6 mW/cm² at the ions.

The duration of the equilibration phase of the experiment was also varied. Starting from an uncooled distribution, the rotational cooling laser beam was unblocked and, a time t later, the REMPD measurement was performed.

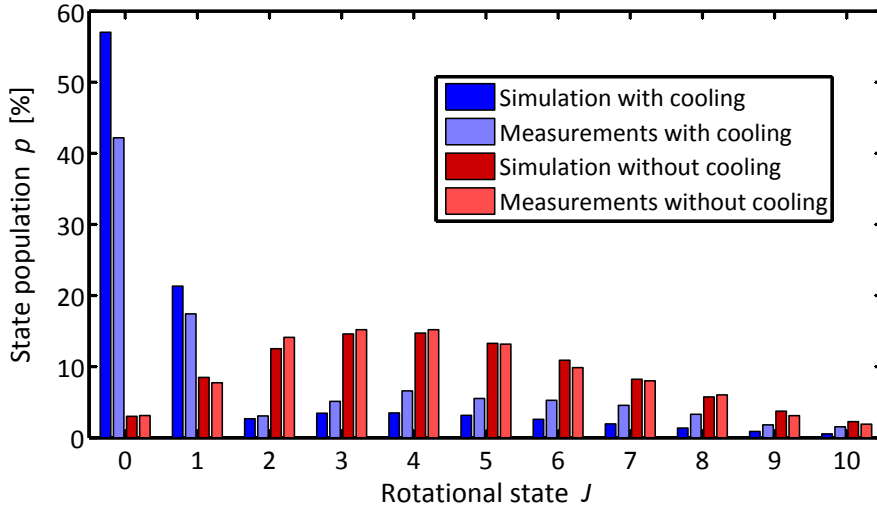


Figure 6.4: Results of the rotational state distribution measurements in the room temperature chamber with and without rotational laser cooling. The results of the simulations based on the A coefficients calculated in 2012 are provided for comparison. Measured populations are calculated from the fractional loss of molecules using equation 6.2. The effect of the rotational cooling laser is very clear, although not as great as the theoretical prediction.

This investigation is shown in figure 6.6 and shows that equilibrium has been achieved at equilibrium phase duration 120 s, which is the time chosen for all other measurements.

Additionally, we verified that the dissociation efficiency was roughly constant when varying the pulse energies of the two pulsed beams around the chosen optimum of $5 \mu\text{J}$ for the 281 nm beam and 1 mJ. Furthermore, the off-resonant two photon contribution of the 266 nm beam was verified to scale quadratically with the pulse energy.

The ion pressure gauge mounted on the vacuum chamber relies on a hot filament to ionize background gas to serve as its pressure indication. This hot filament is not in direct view of the trap center but to verify that it did not somehow indirectly affect the results, we referenced measurements with the filament on to measurements with the filament off. No change was observed.

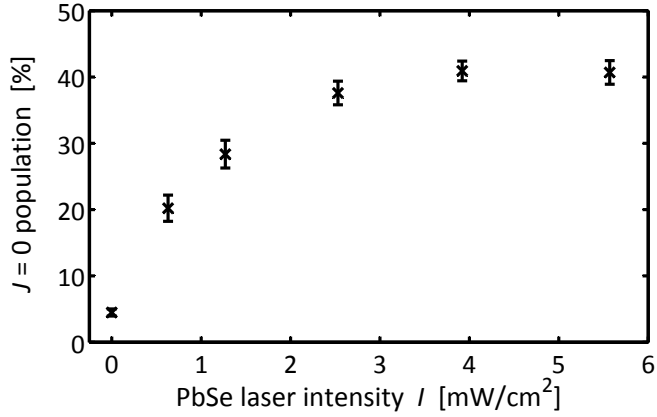


Figure 6.5: Demonstration of power saturation of the optical pumping transition of the rotational cooling scheme. In all other experiments, the power was left at the maximum level: $44 \mu\text{W}$, corresponding to $5.6 \text{ mW}/\text{cm}^2$ at the ions.

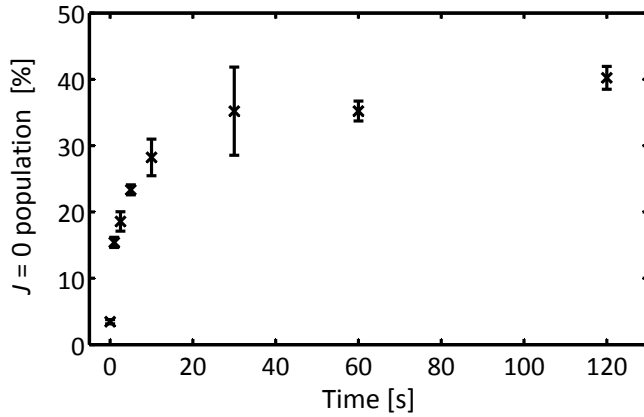


Figure 6.6: A graph of ground state population versus equilibration time. Equilibrium is seen to have been achieved at $t = 120 \text{ s}$, the equilibration time used for all other experiments.

The influence of background gas was investigated by adding neon gas during the equilibration and dissociation phases of the experiment. This is shown in figure 6.7. The addition of neon gas to the chamber resulted in a reduced efficiency of the rotational cooling scheme, indicating that collisions with background gas may have been contributing to the deviation from the simulations (figure 6.4), considering that the state distribution measurements were performed at the ordinary background pressure of 4×10^{-10} mbar.

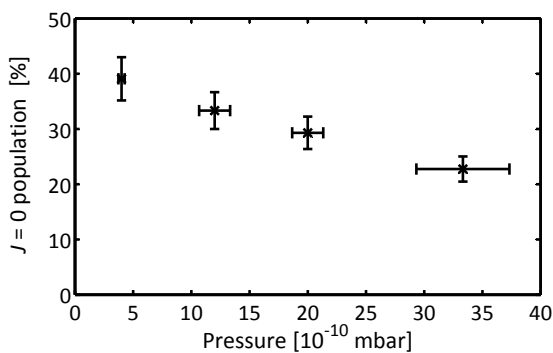


Figure 6.7: Investigation of the effect of introducing additional neon gas to the background in the chamber during the equilibration and dissociation phases. The base pressure of 4×10^{-10} mbar consisted of the usual background gases of the chamber without neon. To test the effect of higher background pressure, neon gas was added. The increase in background pressure is seen to reduce the efficiency of the rotational cooling scheme.

To obtain a time scale characteristic only of rotational dynamics and not involving any vibrational dynamics, we measured the 're-heating' rate of the system. Starting from the equilibrated cooled distribution, the PbSe laser beam was blocked and then, a time t later, the population in the ground state was measured. This evolution is then indicative purely of the rotational time scales involved as the molecules re-thermalize to the room temperature distribution. This is shown in figure 6.8 along with a theoretical prediction, shown with the dashed curve. The theoretical prediction is the result of a simulation in which the $t = 0$ distribution was set equal to the experimentally measured distribution (figure 6.4) and the dynamics then from that point on proceeded according to the theory without optical pumping. The molecules are seen to equilibrate somewhat faster than the theory based solely on black body radiation dynam-

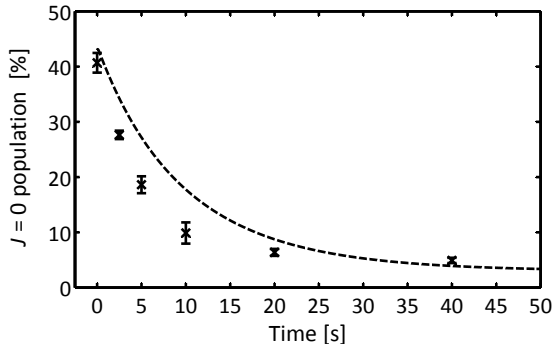


Figure 6.8: Plot of the evolution of the ground state population from the cooled distribution to the uncooled distribution. At time $t = 0$, the PbSe laser was blocked and at time t , the REMPD measurement was performed. The dashed curve indicates a simulation prediction in which the $t = 0$ population distribution has been set equal to the experimentally measured distribution and the dynamics then from that point on proceed according to the theory without optical pumping.

ics predicts, even when disregarding the discrepancy between the theoretical and experimental cooled distributions. Collisions with background gas would contribute to such an increased re-heating rate.

The dissociation process in the room temperature experiments is not 100 % efficient. Considering that the lifetime of the intermediate electronically excited state A is on the order of 10 ns, spontaneous decay from A to a variety of vibrational and rotational states in X can play a role in the dissociation process. Shortly after the passage of the pulse pair, the population in the addressed state may thus be either dissociated, redistributed by electronic and rovibrational cascade to other rotational states in X or left in the addressed state. We measured that performing REMPD events with two consecutive pairs of pulses (~ 98 ms spacing) did not result in a greater fractional loss in molecules after compensation for the additional off-resonant two photon contribution from the second pair of pulses. Therefore, we can conclude that the addressed state is indeed empty after an REMPD event, with almost all molecules dissociated and the rest redistributed to other rotational states.

In addition to the above systematic checks, some other investigations were made using the single color REMPD scheme. These verified that the dissociation

rates on R(0) and on R(5) (where the cooling signature was most prominent) were independent of the following parameters:

1. The direction of polarization of the 281 nm pulsed beam
2. The temperature of the Mg source oven
3. The magnetic field applied in the trap center
4. Whether the room lights were on or off
5. Whether the polarization of the PbSe laser beam was scrambled or not
6. The intensity of the CW 280 nm Doppler cooling beams

Although no dependence on the polarization scrambling of the rotational cooling laser beam was found, the rest of the room temperature chamber measurements were nevertheless performed with scrambling.

6.3 Modelling the effect of collisions

One possible explanation for the discrepancy between the measurements and the simulation results is that collisions with background gases occur on a faster time scale than the cooling equilibration and that these collisions change the rotational state.

Although a full and accurate description of the potential effect of collisions in the experiment is highly complicated and beyond the scope of this thesis, I will here apply a very simplified model. Collisions between molecular ions and neutral gas are known to exhibit a strongly oscillating dependence on the collision energy and show decreased rotational transition probability amplitudes with increasing $|\Delta J|$. As an example, a study was performed by Andersson, Barinova and Nyman in 2007 concerning the rotational transitions induced in CO^+ molecules in collisions with atomic hydrogen [106]. In this study it was additionally found that transitions with odd ΔJ were preferred over transitions with even ΔJ .

In our case, collisions are taking place in a broad (thermal) range of energies with a number of different background gas species. The neon used for the pressure test of figure 6.7 is atomic, while the other gases in the chamber are molecular. Some of the gases possess a permanent dipole moment, some do not. Some of the gases have high polarizability and others have only a low polarizability. Considering that ion-neutral collision cross sections are highly

dependent on the dipole moment and polarizability of the neutral, accurate modelling of the effect of collisions on this experiment is a daunting task.

Rather than attempting to model all these phenomena, I will base a qualitative model on the bold assumption that, whenever a background gas atom or molecule collides with a molecular ion, the internal state of the molecular ion is completely overwritten by a thermal Boltzmann distribution of a temperature corresponding to the background gas, room temperature. Based on the agreement between the uncooled distribution and room temperature, I choose in this model to neglect the temperature of the micromotion of the ions (section 2.1.4), which is on the order of a few tens of kelvin.

If we assume that a sufficient amount of measurements are made that the stochastic nature of these dynamics average out, we can neglect the random element and introduce the effect of collisions on the rotational distribution by modifying the elements of the coupling matrix K introduced in equation 4.8. Denoting the population vector for a MgH^+ room temperature Boltzmann distribution \vec{p}_0 , the coupling towards a room temperature state that collisions will induce in this simple model is described by adding $\Gamma_c \vec{p}_0$, where Γ_c is the collision rate for the individual ion, to each column of K .

If $\Gamma_c = (30\text{ s})^{-1}$, the simulation equilibrium results depicted in figure 6.9 are obtained. The re-heating process in this simulation is compared to measurements in figure 6.10, and the onset of the rotational cooling, starting from the room temperature thermal distribution, is shown in figure 6.11.

Although the model should only be thought of as a qualitative indicator of the effect of collisions, a collision rate of $\Gamma_c = (30\text{ s})^{-1}$ reproduces the equilibrium rotational distribution and the time scales of the re-heating process and the rotational cooling onset pretty well.

6.3.1 Theoretical estimation of Γ_c

To estimate whether such a collision rate is realistic considering the quality of the vacuum, we can make a rough theoretical estimate of the expected rate of collisions with background gases.

An approximative description of collisions between ions and non-polar neutrals is provided by the Langevin capture model. In this model, the electric field of the ion induces a polarization of the neutral atom or molecule which results in an attractive force between the ion and the neutral scaling as R^{-4} .

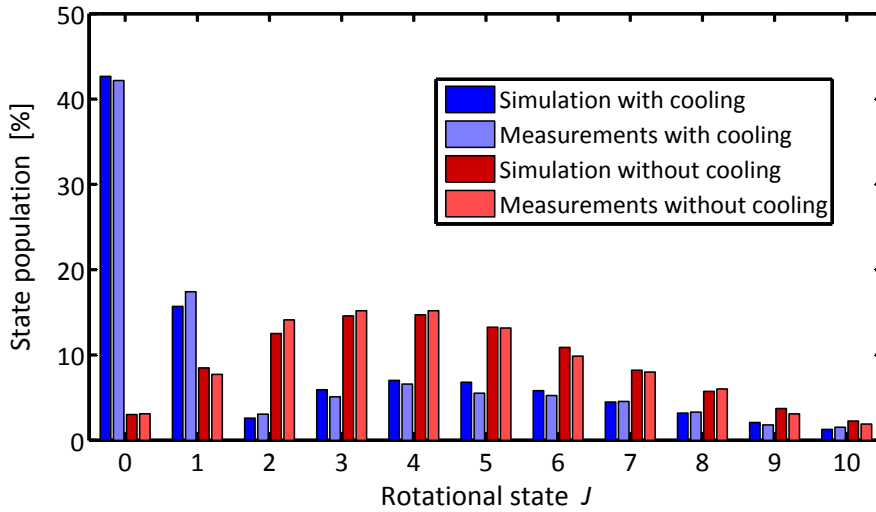


Figure 6.9: Results of the rotational state distribution simulation with the highly simplified implementation of collisions. The collision rate is here $\Gamma_c = (30\text{ s})^{-1}$.

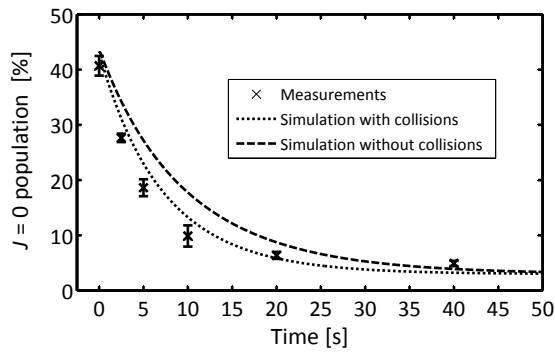


Figure 6.10: Comparison of simulations and measurements for the reheating process.

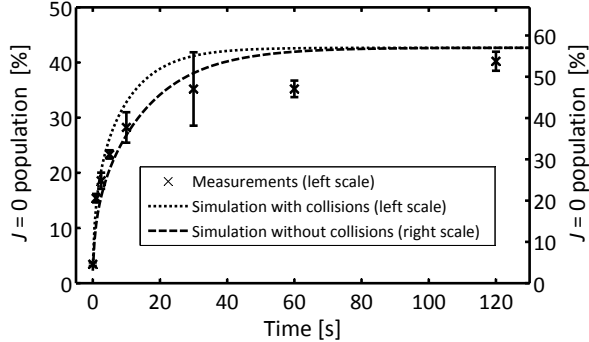


Figure 6.11: Comparison of simulations and measurements for the onset of the rotational cooling process. Note that while the measurements and the simulation with collisions are plotted against the left scale, the simulation without collisions is plotted against the right scale and is drawn here only for comparison of the cooling time scale.

The collisional cross section in this model [107] is given by

$$\sigma = \frac{e}{2\epsilon_0} \sqrt{\frac{\alpha}{\mu v_r^2}} \quad (6.5)$$

where α is the mean polarizability of the neutral, μ is the reduced mass of the ion-neutral system and v_r is the relative velocity in the ion-neutral center of mass frame. In the case of a ion stationary in the laboratory frame, the relative velocity is equal to the velocity of the neutral in the laboratory frame, v .

The collision rate Γ_c experienced by a stationary ion in an environment of neutral gas at laboratory frame velocity v and density n can thus be found through the Langevin collisional cross section as

$$\Gamma_c = nv\sigma = n \frac{e}{2\epsilon_0} \sqrt{\frac{\alpha}{\mu}} \quad (6.6)$$

This expression is independent of v , which allows us to disregard the distribution of velocities that the neutrals exhibit.

Mean polarizabilities for some neutrals of interest [108] are shown in table 6.1 with the corresponding Langevin ion collision rates for a pressure of 4×10^{-10} mbar and room temperature.

	α (au)	Γ_c/n (10^{-10} cm ³ /s)	Γ_c (mHz)	τ_c (s)
H ₂	5.314	15.27	15	67
He	1.407	5.758	5.6	178
Ne	2.571	4.336	4.2	236
N ₂	11.54	8.426	8.2	122
O ₂	10.54	7.812	7.6	131
CO ₂	16.92	9.287	9.1	110

Table 6.1: Calculations of Langevin capture collision rates for various non-polar atoms and molecules. The time scale $\tau_c = \Gamma_c^{-1}$ is also shown. The value used for $n = p/(k_B T)$ for each species is 9.8×10^6 cm⁻³, corresponding to a room temperature gas at pressure 4×10^{-10} mbar. For polarizability, 1 au = $1.648\,777 \times 10^{-41}$ C²m²/J.

The majority of the rest gas is likely to be hydrogen. Due to difficulty in calibrating the sensitivity of the ion gauge to a precision beyond a factor two, the theoretical Langevin collision time scale of 67s agrees decently with the simulation collision time scale parameter of 30s.

6.4 Single ion measurements

Although being able to cool the rotational degree of freedom of an ensemble of molecular ions as described in the previous sections is a very important step on the road to reaching the quantum limit of state preparation, it is also possible to extend the experiment to the quantum limit in terms of the amount of molecules involved. In the ion trap, it is easy to work with only a single molecular MgH⁺ ion simply by first loading two Mg⁺ ions into the trap, Doppler cooling them, introducing hydrogen gas to make one of them react and then stopping the reaction. The molecular ion is apparent by its displacement of the fluorescing Mg⁺ ion and its mass can even be verified using the SCS-MS technique (section 2.1.5), as shown in figure 2.9.

In the experiments with single ions, we occasionally observed reactions leading to molecules of mass 26 (MgD⁺) rather than mass 25 (MgH⁺). In this event, the ions were discarded and new ones were loaded. Since the experiments of reaction between Ca⁺ ions and HD gas (chapter 8) had been performed after the MgH⁺ ensemble measurements but before the MgH⁺ single ion measure-

ments, we concluded that the chamber and gas delivery foreline must still have been slightly contaminated by HD gas. Had such a contamination occurred in ensemble measurements, the small amount of MgD^+ ions would be both impossible to detect and unfeasible to remove, but would still skew the dissociation measurement results. This is one of the strong arguments in favor of performing single ion experiments rather than ensemble experiments: No averaging is performed over an ensemble that may contain impurities, known or unknown.

The molecular ion is held translationally cold due to the sympathetic cooling of the Doppler cooled Mg^+ ion. Trap parameters are chosen such that $\omega_r > \omega_z$, so that the two ions form a string on the rf-free center axis of the trap. The rotational cooling scheme can be applied in the same way as in the ensemble case to cool the molecule internally.

Although a more complete charting of the rotational distribution for a single molecular ion in the cooled and uncooled case was carried out in the cryogenic trap (section 7.5), the early experiments presented here were performed in the room temperature trap.

Rather than, as in the ensemble case, performing one REMPD event and measuring the fraction S of dissociated molecules, the outcome of a single ion REMPD measurement is binary in nature—either the molecule dissociates or it does not, and the probability for the dissociation to occur is S . An event where the molecule did not dissociate is counted as a measurement that the molecule was, in that instant, not in the targeted state. After re-equilibration, another pulse pair can be admitted to make a new measurement. An event where the molecule does dissociate is counted as the molecule either being in the targeted state or having dissociated due to the off-resonant two photon transition caused by the 266 nm beam. Upon dissociation, a new $\text{Mg}^+ + \text{MgH}^+$ ion pair is then prepared and equilibration is reached before the next REMPD event is initiated. The contribution of off-resonant dissociation was calibrated using ensembles to 0.55 % for these experiments.

6.4.1 Likelihood theory

The experiment thus results in a number of dissociations n out of a number of REMPD attempts N . While a simple rough estimate of the dissociation probability S per REMPD attempt can be made using $S = \frac{n}{N}$, it is worthwhile to look into the likelihood theory concerning this type of probabilistic measurement.

Assuming complete reequilibration before each REMPD attempt, the outcome of each event can be considered completely independent of the history of the experiment and the probability of getting a dissociation is the same, S , for

each event. The problem is, as such, the same as determining the probability of getting heads in a coin toss and is treated in many statistics textbooks. In this type of problem one is interested in the likelihood function of S , that is, the distribution of conditional likelihood that S is equal to any particular value given an experimentally measured number of 'heads' (dissociations) n out of a total number of attempts N .

I will here give the result of the standard solution to the problem using the coin toss analogy. The total amount of coin tosses is N , the amount of heads is h , the amount of tails is t and the actual probability of getting heads in a toss is p . p is the quantity that we must determine.

The probability of getting h heads in N coin tosses is given by the binomial distribution:

$$\Pr(H = h|p, N = h + t) = \binom{N}{h} p^h (1 - p)^t \quad (6.7)$$

The likelihood distribution $f(p)$ is given by the probability density function of the conjugate prior for the binomial distribution, which is the beta distribution. Since h and t are integers, the beta distribution can be written using factorials as

$$f(p|H = h, T = t) = \frac{(N + 1)!}{h! t!} p^h (1 - p)^t \quad (6.8)$$

We now change to our use of variables. Since we denote the number of successful attempts n and the probability S , our likelihood distribution is

$$f(S|n, N) = \frac{(N + 1)!}{n! (N - n)!} S^n (1 - S)^{(N - n)} \quad (6.9)$$

some figures that may be of interest to the reader for this distribution include the maximum likelihood value

$$S_{\text{ML}} = \frac{n}{N} \quad (6.10)$$

where the likelihood function peaks, the expected value

$$E(S) = \frac{n + 1}{N + 2} \quad (6.11)$$

which is the mean of the distribution and the variance

$$\text{Var}(S) = \frac{(n + 1)(N - n + 1)}{(N + 2)^2 (N + 3)} \quad (6.12)$$

No closed form expression exists for the median value of the distribution.

6.4.2 Results

Single ion measurements on R(0) with rotational cooling showed 36 dissociations in 108 dissociation attempts. The convergence of the dissociation probability S with increasing number of dissociation attempts is shown in figure 6.12.

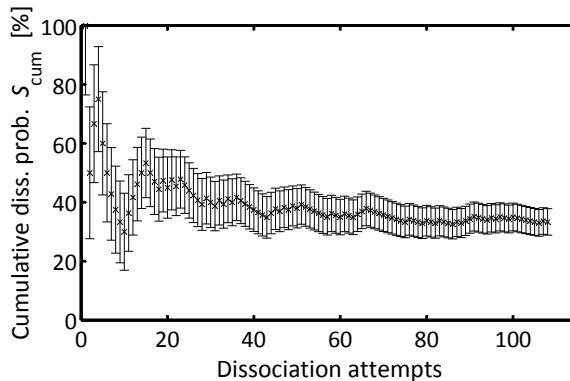


Figure 6.12: A visualization of the convergence of the cumulative dissociation probability S_{cum} as the single ion experiment on R(0) progressed. The data points drawn are the cumulative maximum likelihood estimates $n_{\text{cum}}/N_{\text{cum}}$ and the error bar shown in this visualization is $\pm\sqrt{\text{Var}(S_{\text{cum}})}$, the standard deviation of the beta distribution.

The most faithful representation of the result of this experiment is the likelihood distribution for S . The likelihood distribution is the probability density function (PDF) of the beta distribution shown in figure 6.13. Also shown is the dissociation probability S for ensemble experiments.

In addition, 114 shots were made on R(5) with rotational cooling, with 8 of them resulting in dissociation. As for R(0), the convergence is illustrated in figure 6.14. The likelihood distribution for this statistic is seen in figure 6.15 along with the corresponding ensemble S value.

From these two measurements, no obvious difference is apparent between the single ion case and the ensemble case. More data would have had to be collected to make a statement about whether a rotationally cooled single ion is more or less cold than a rotationally cooled ensemble in the room temperature trap. Because of time constraints, we had to move on to testing an important further enhancement of the state preparation scheme: Dissociative state preparation.

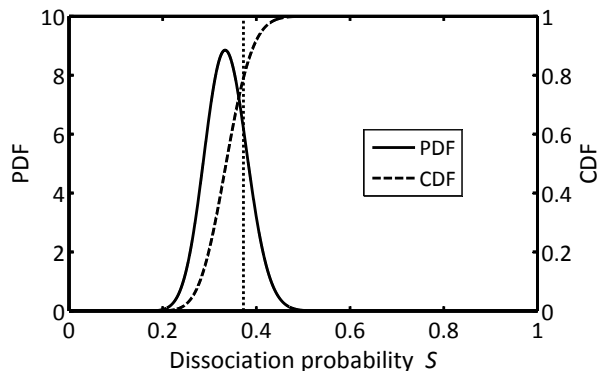


Figure 6.13: Likelihood distribution of the dissociation probability p for single ion REMPD on R(0) with rotational cooling. 108 REMPD attempts were performed, with 36 of them resulting in dissociation. The probability density function (PDF) and cumulative distribution function (CDF) for the likelihood distribution are shown. The vertical dotted line is S for the ensemble case.

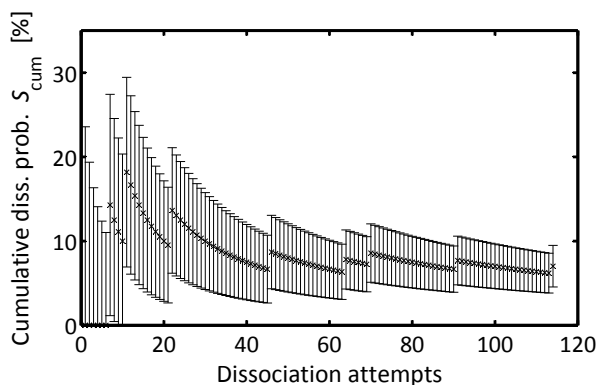


Figure 6.14: A visualization of the convergence of the cumulative dissociation probability S_{cum} as the single ion experiment on R(5) progressed. The data points drawn are the cumulative maximum likelihood estimates $n_{\text{cum}}/N_{\text{cum}}$ and the error bar shown in this visualization is $\pm\sqrt{\text{Var}(S_{\text{cum}})}$, the standard deviation of the beta distribution.

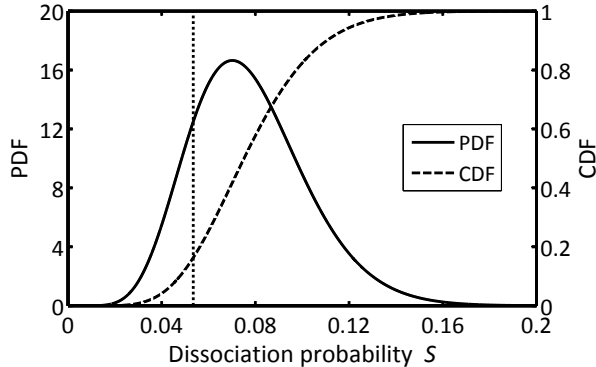


Figure 6.15: Likelihood distribution for the dissociation probability of measurements on R(5). 114 REMPD attempts were performed, of which 8 resulted in dissociation. The probability density function (PDF) and cumulative distribution function (CDF) for the likelihood distribution are shown. Note the change in S -axis compared to figure 6.13. The vertical dotted line is S for the ensemble case.

6.5 Dissociative state preparation

Before the arrival of the cryogenic trap chamber covered in chapter 7, we had time to quickly test the application of so-called dissociative state preparation in the room temperature trap. For ensembles, the principle of dissociative state preparation is that, starting from a rotationally cooled distribution, the fraction of molecules in the ground state can be increased by state selectively dissociating molecules that are not in the ground state.

The same method can be applied to a single molecular ion, although the interpretation is then slightly different. At an REMPD event, rather than having removed molecules in the addressed state, one obtains knowledge about the state of the molecule. If the molecule did not dissociate, it is then known to not have been in the addressed state and the *probability* that it is in each of the other states is thus higher than before the REMPD event. If the molecule does dissociate, one can simply load another molecule and try again. This is a type of quantum projection measurement, in which the wave function representing our knowledge of the state of the molecule is at every dissociation attempt projected into the states that are not addressed by the REMPD scheme.

The scheme that was tested in the room temperature trap was, after preparing a single molecular ion in the trap and equilibrating in the presence of the PbSe rotational cooling laser, to open the shutters for the pulsed lasers at time $t = 0$ and leave them open, repetitively dissociating on R(5), emptying the $J = 5$ state. For each dissociation attempt the molecule survives, a new quantum projection is made and new information is gathered about the state of the molecule. With the aid of simulations of the rotational and vibrational dynamics, the evolution of the probability distribution of the molecular ion can be mapped out as a function of time.

In the simulation, a dissociation event at time t_0 is modelled by propagating the population vector \vec{p} at $t < t_0$ and $t > t_0$ as usual, but at $t = t_0$ setting $p_{(0,5)} = 0$ and renormalizing to unity total population. Redistribution is thus neglected in this simulation. A plot of the simulated ground state population and the survival probability during the dissociative preparation scheme is shown in figure 6.16, with and without the simplistic collision implementation of section 6.3 with $\Gamma_c = (30\text{ s})^{-1}$. The A coefficients used for these simulations are the ones determined in 2012.

In both simulations, the dissociative state preparation has taken full effect after ten seconds. The increase in ground state population/probability is seen to be greater in the case with collisions than in the case without collisions. However, the probability that the molecule has not been dissociated is lower in the simulation with collisions.

6.5.1 Results

Out of 8 dissociative state preparation sequences on single molecular ions, 2 ions survived past the 10s mark, reaching 15.5s and 27.3s. At these times, the probability of residing in the ground state was predicted to be 64% by the model with collisions and 68% by the model without collisions.

More data was collected in a corresponding experiment performed in the cryogenic trap, but the data treatment on these measurements was not ready in time for the writing of this thesis and the measurements are thus not included.

6.6 Conclusions

The implementation of laser induced cooling of the rotational degree of freedom of MgH^+ ions has proven successful, along with the REMPD schemes for measurement of the rotational population distribution. Although the cooling

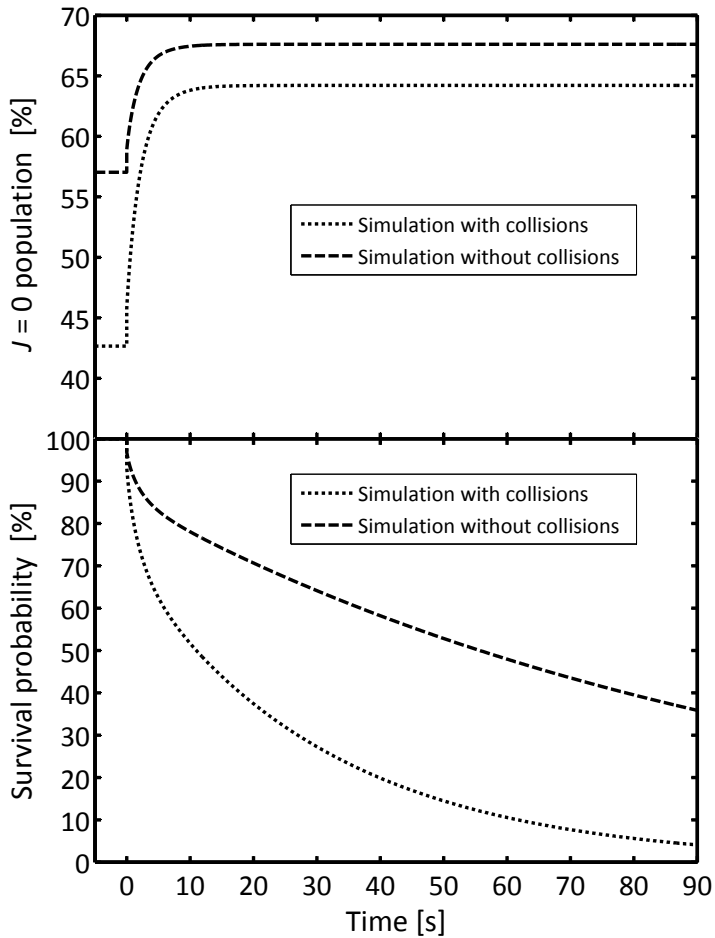


Figure 6.16: Simulation modelling of R(5) dissociative state preparation. In this implementation, the molecule(s) are allowed to equilibrate in the presence of the rotational cooling laser, after which $J = 5$ is emptied at $t = 0$ and at all later multiples of the pulsed laser repetition period $(10.19\text{ Hz})^{-1}$. This repetition rate was chosen to correspond to that of the Quantel Nd:YAG laser that the experiments in this chapter was performed with. Redistribution is disregarded, as well as the risk of dissociating through a two photon excitation.

signature was visible in the single color dissociation scheme, much more information was provided by the two color dissociation scheme.

Using the two color dissociation scheme on Coulomb crystal ensembles, the final achieved ground state population was measured to be $42 \pm 2\%$ with a $J = 1$ population of $17 \pm 2\%$. In terms of ground state population, this is equivalent to a thermal distribution at $18 \pm 2\text{K}$. The deviation from theory may be related to collisions with background gas.

In addition to the ensemble measurements, rotational cooling of single ions was also carried out with measurements based on the same two color dissociation scheme. Since single ions located on the field free center axis of the linear Paul trap do not exhibit micromotion and may even with a suitable laser source be cooled through sideband cooling, reaching this regime is essential for experimenting with molecular ions that are cold in all degrees of freedom.

Finally, we made a few measurements on an implementation of dissociative state preparation in the room temperature trap. Depending on the simulation model applied, the equilibrium ground state population in these measurements was in the region of 64% to 68%. The scheme used here consisted of dissociating on the $R(5)$ transition with the rotational cooling applied, but many other schemes are feasible, including dissociation through $R(0)$ with rotational cooling, causing population to accumulate in the $J = 1$ state.

Rotational cooling of MgH^+ in the cryogenic CryPTEx ion trap

Another way of cooling the internal degree of freedom of molecules is to put them inside a cryogenic environment where the spectral energy density of the black body radiation will be far lower than inside a room temperature chamber such as the one used for the experiments of chapter 6. In addition to reducing the intensity of the thermal radiation experienced by the molecules, the cryogenic surfaces inside the chamber will function as a cryopump, adsorbing to a large degree those gas species that have a higher boiling point than the temperature of the cryogenic shields. This contributes to increasing the quality of the vacuum, and the cryogenic shields will tend to decrease the temperature of the remaining background gases such that a collisions between a trapped molecular ion and background gas will not heat the molecule as much as in a room temperature trap.

In collaboration with the group of José Crespo at the Max-Planck-Institut für Kernphysik in Heidelberg, Germany, experiments were carried out at the Ion Trap Group in Aarhus to measure the rotational distributions of MgH^+ ions in various experiments in such a cryogenically cooled ion trap. The chamber, ion trap and its accessories were constructed at the Max Planck Institute in Heidelberg by PhD student Maria Schwarz with the help of diploma student Franziska Brunner and masters student Tim Ballance under the supervision of Dr. José Crespo. The ion trap will be used in the coming years for studying highly charged ions, and the system has been given the name 'Cryogenic Paul Trap Experiment' (CryPTEx). A publication detailing the characteristics of the trap and chamber was published in Review of Scientific Instruments in 2012 [109].

The CryPTEx chamber was shipped to Aarhus and installed in the Ion Trap Laboratory in September 2011. At the time of writing of this thesis, September 2012, final measurements are being performed to wrap up the rotational dynamics experiments on that chamber. After completion of those experiments, the CryPTEx chamber will return to Heidelberg in Germany and be used for studying the spectroscopy of highly charged ions delivered from an EBIT (Electron Beam Ion Trap).

7.1 Characteristics of the cryogenic CryPTE_x trap and chamber

I will here provide a basic overview of the CryPTE_x vacuum chamber and ion trap. For a much more in depth description and characterization, consult the PhD thesis of Maria Schwarz [110].

7.1.1 Vacuum chamber

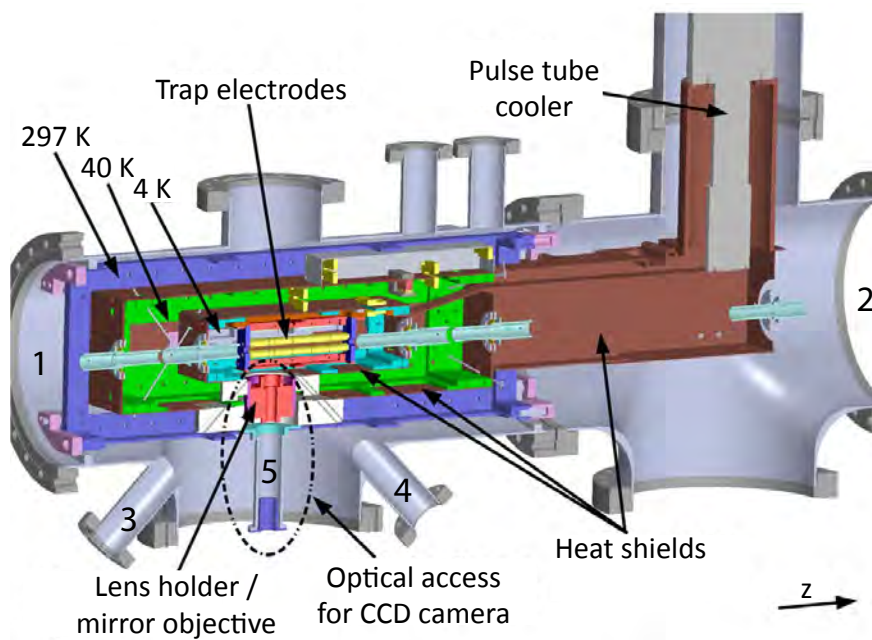


Figure 7.1: From [110]. A vertical cross section through a Solidworks model of the CryPTE_x chamber.

A vertical cross section through a Solidworks model of the CryPTE_x chamber is shown in figure 7.1. The CryPTE_x chamber features a pulse tube cooler (Sumitomo Heavy Industries model SRP-082B-F20H) cooling two heat shield stages within the chamber. The outer frame is not actively cooled and is thus

near room temperature. The intermediate heat shield is cooled to a temperature of roughly 40 K, while the inner heat shield and trap electrodes are cooled to a temperature of 4 K. A helium flow is maintained through the pulse tube cooler by a water cooled He compressor.

Vacuum is obtained and maintained by two 300 L turbomolecular pumps, backed by a 70 L turbomolecular pump, which is further backed by a scroll pump. The pressure in the chamber is measured with Penning gauges and ionization gauges, and drops to the 1×10^{-8} mbar level when the chamber is pumped with the turbomolecular pumps but the cryogenic system is not engaged. Upon activation of the cryogenic cooling, the pressure drops further, reaching about 1×10^{-9} mbar at the pressure gauges mounted on the walls of the chamber. The pressure inside the 4 K stage is expected to be significantly lower than this due to the cryopump effect of the heat shields.

Access to the trap center is available in both directions through the center axis of the trap (numbered 1 and 2 in figure 7.1), vertically and diagonally below the chamber (numbered 5, 3 and 4 respectively in figure 7.1) and through 10 viewports on the side of the chamber (numbered 1–10 in figure 7.2). Figure 7.2 shows a horizontal cross section through the trap center in a Solidworks model, illustrating the axial access and the 10 viewports on the side of the chamber, all pointing towards the trap center.

In access path 5 of figure 7.1, a lens with focal length $f = 40$ mm is mounted inside a lens holder. The lens focuses the light from the ions in the trap center onto an image intensifier mounted outside and below the chamber. As in the setup for the room temperature chamber, the light of the image intensifier is imaged onto a CCD camera. The total magnification of the system from ion to CCD chip is $\times 9$, which is enough to clearly distinguish neighboring ions. For the future experiments on highly charged ion spectroscopy, it will be replaced with a mirror objective because of the need for an achromatic imaging system for such experiments.

Side port 1 in figure 7.2 was in early experiments occupied by a gas delivery system, which was used for introducing hydrogen for the $\text{Mg}^+ + \text{H}_2$ reaction. It was removed after the installation of another hydrogen source mounted on diagonal access path 4 underneath the chamber.

The side port opposite of the original hydrogen source, side port 6, is occupied by a Mg source. Separated from the main chamber by a gate valve, it contains an Alvatec Mg source aligned in the path leading to the trap center. A flux of atomic magnesium through the trap center can thus be established by opening the gate valve and heating the source to ~ 350 °C.

A translation stage is mounted on side port 9 enabling the insertion of a fiber

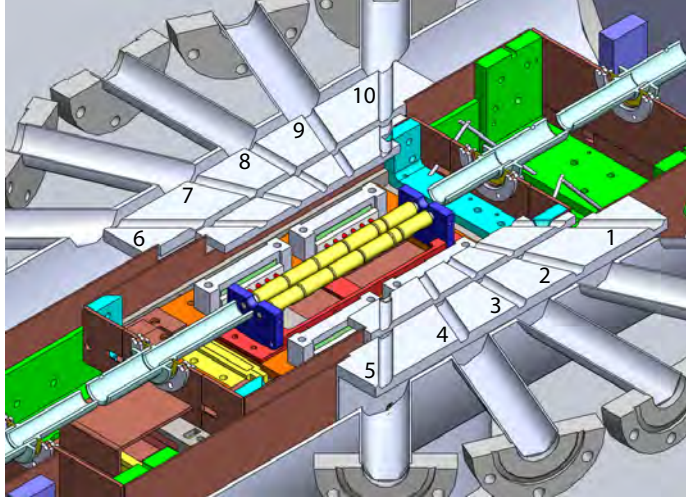


Figure 7.2: A horizontal cross section through a solidworks model of the CryPTEch chamber. The lower 12 of the 24 trap electrodes are visible in this section. The 10 side port access paths are also shown in addition to the axial path. The light blue cylindrical tubes along the trap axis are Einzel lenses for injection and ejection of ions in future experiments in Heidelberg.

tip of diameter $125\ \mu\text{m}$ into the trap center with a precision of about $50\ \mu\text{m}$. As in the room temperature chamber, this is used for calibration of the imaging system and for positioning of the laser beams by observing either the shadow of the fiber in the transmission of the beam through the chamber or the diffraction pattern caused by diffraction around the fiber.

$280\ \text{nm}$ Doppler cooling beams were aligned through the axial ports 1 and 2 of figure 7.1 as well as through the radial side port 3 of figure 7.2. The radial beam was used only for the single ion experiments. The $285\ \text{nm}$ ionization beam was admitted through side port 10. The pulsed REMPD beams ($281\ \text{nm}$ and $266\ \text{nm}$) were both introduced through side port 5, opposite the ionization beam. In some measurements, the QCL (Quantum Cascade Laser) beam at $6.2\ \mu\text{m}$ was admitted through side port 2 but in other measurements it was admitted through the axial port 2.

After some initial measurements, some CaF_2 windows, fused silica windows and aluminum discs were installed inside many of the access paths to the trap center. These were mounted in the $40\ \text{K}$ stage to reduce the potential impact of

collisions with background gas molecules originating from the room temperature viewports. CaF_2 windows were installed in the axial paths 1 and 2 and the side ports 2, 3, 7 and 8, fused silica windows were installed in side ports 5 and 10 and aluminum discs were inserted in side ports 1 and 4 and in the diagonal port 3. Considering that a fused silica lens was from the beginning mounted in the 4K stage of the vertical access port 5 for imaging, this operation left only diagonal port 4 (H_2 source) and side ports 6 (Mg source) and 9 (alignment fiber) unblocked.

The measurements presented in section 7.7 were performed before the installation of the windows, while all other measurements I will present in this chapter were performed after the installation. These windows are assumed to have no effect on the measurements of the vibrational decay studied in section 7.7, since it in any case is much faster than the rate of interaction with background gas or black body radiation.

7.1.2 Ion trap

The CryPTEEx ion trap is a linear Paul trap with each of the 4 rods segmented into 6 electrodes, making for 24 electrodes in total. The first three segments are nearly identical in dimensions to the trap used for the experiments in the room temperature chamber, that is, two endcap segments of length $z_{\text{endcap}} = 20.00$ mm, a center electrode of length $2z_0 = 5.40$ mm, a rod radius of $R = 4.00$ mm and a diagonal rod separation $2r_0 = 7.00$ mm (see figure 2.3b). Due to a slight difference in the spacing between the segments, the geometric factor for the CryPTEEx trap is $\eta = 0.259$ as opposed to 0.248 for the room temperature trap. The last three segments are all 20.00 mm long and define a pre-trap region that can be used in addition to the main trap region created by the first three segments. The radiofrequency voltage is applied to all electrodes along each rod, creating radial confinement in both the pre-trap and the main trap. The pre-trap region was not used in the experiments in Aarhus, and all of its 12 electrodes were grounded during all experiments. An image of the CryPTEEx trap during assembly is shown in figure 7.3.

7.2 Theoretical modelling of rotational dynamics and equilibria

When assembling a cryogenic system, it is necessary to polish the heat shields to minimize the emissivity of the surfaces, such that the shields will absorb as little

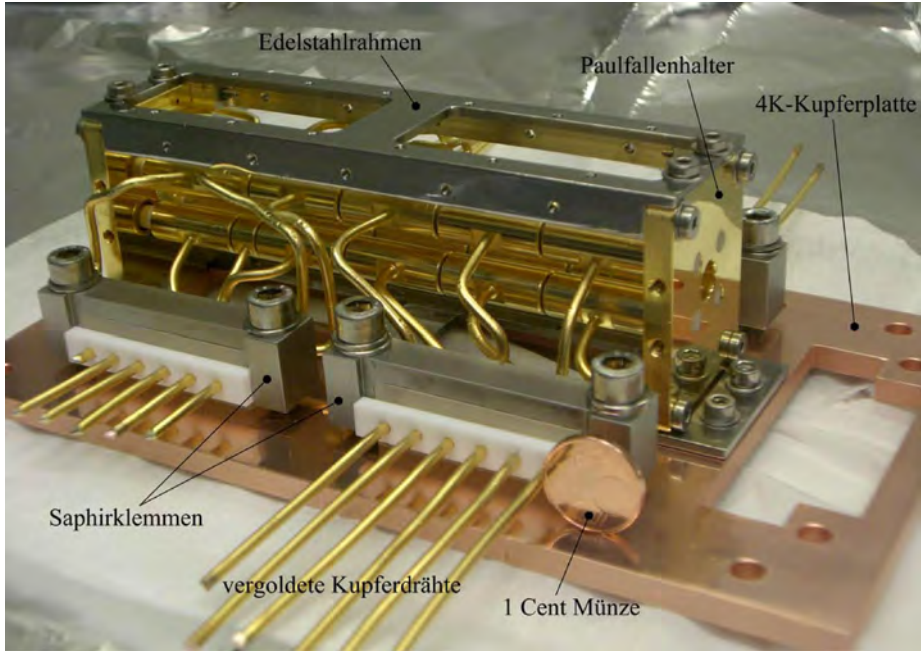


Figure 7.3: From [110]. A photograph of the CryPTEx trap taken during assembly. Saphirklemmen: Sapphire clamps; vergoldete Kupferdrähte: Gold plated copper wires; 1 Cent Münze: 1 cent coin (€); Edelstahlrahmen: Stainless steel frame; Paulfallenhalter: Paul trap holder; 4K-Kupferplatte: 4K copper plate.

thermal radiation from warmer surfaces as possible. Since the trap center is thus surrounded by shiny surfaces with low emissivity, the surroundings cannot be modelled as black bodies.

Because of the need for access to the trap center for laser beams, atomic beams and molecular beams, room temperature surfaces are in direct view of the ions. As mentioned in section 4.1.2, the spectral energy density ρ in the case of such a mixed-temperature environment with reflecting surfaces depends not only on solid angles and temperatures but also the wavelength dependent emissivities and the specific geometric configuration of the surfaces. Since the emissivity curves into the far infrared are generally not known, we have not attempted to make an accurate theoretical assessment of ρ .

It is, nevertheless, instructive to simulate the rotational dynamics in the hypothetical limit case of a 4 K black body radiation field without any collisions. To get an impression of the time scale for equilibration in this kind of environment, four different initial population distributions have been chosen: Boltzmann distributions of temperatures 3000 K, 297 K, 30 K and 10 K. Equilibrations from these distributions are plotted in figure 7.4. At 4 K, the rotational distribution has a population of 96.8 % in the ground state and 3.2 % in the $J = 1$ state.

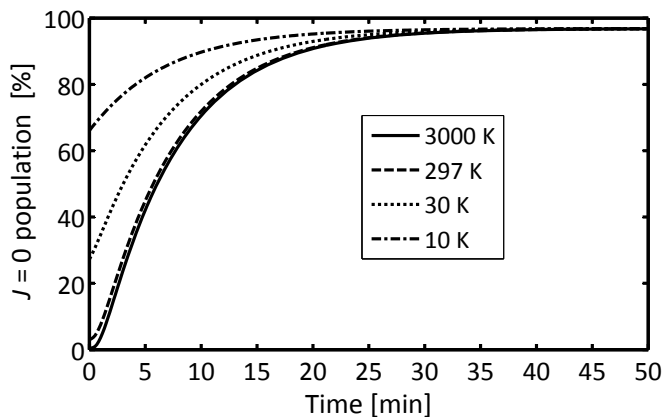


Figure 7.4: Theoretical equilibration to a perfect 4 K black body radiation environment with no collisions, starting from Boltzmann distributions of various temperatures. The equilibration is dominated by the slow spontaneous decay from $|v = 0; J = 1\rangle \rightarrow |v = 0; J = 0\rangle$ with $A = 0.0023$ Hz. The equilibration time is largely independent of the initial distribution.

7.3 Preliminary characterization of the dissociation process

Many of the types of measurements carried out in the room temperature trap were repeated in greater detail in the CryPTE_x trap. Since the degree of state preparation was greater than in the room temperature trap, it was necessary to have a model incorporating the effects of redistribution in the dissociation

process (the $A \rightarrow X$ spontaneous decay). That is, we had to determine the probability of resonantly dissociating an ion in the target state P_d , the probability of having the ion experience redistribution P_r as well as the probability for any molecular ion to be dissociated by the non-resonant two photon process P_{266} .

As of the time of writing of this thesis, the data treatment concerning the REMPD characterization is still ongoing and I will in the rest of the chapter only provide careful preliminary results and conservative estimates.

7.3.1 Outline of the model

Several models may be applied to describe the dissociation process. In the following I will walk through one such model which may or may not be the one used for the final interpretation of the data.

To model the process of a single REMPD event I apply a two step model, in which the first thing to happen is the dissociation of a fraction P_{266} of all molecules in all rotational states. The second step is then the resonant addressing of a fraction of molecules P_d out of each addressed magnetic substate to be dissociated and a fraction P_r out of each addressed magnetic substate to be redistributed to other rotational states. I assume, as in the room temperature case, that P_d and P_r are independent of rotational state.

Since only the fraction $\beta = \frac{2J-1}{2J+1}$ of magnetic substates get probed when using a P transition with linearly polarized light, we can write the fraction of dissociated molecules βP_d and the fraction of redistributed molecules βP_r , this time relative to the population of the entire rotational state rather than just the probed magnetic substates. We extend this expression to cover R transitions as well by defining that $\beta = 1$ for R transitions.

Starting with a population p_0 in a particular rotational state, the population $p_{1,266}$ in that state and the population $q_{1,266}$ in all *other* states after the first step of the REMPD event is thus:

$$p_{1,266} = p_0(1 - P_{266}) \quad (7.1)$$

$$q_{1,266} = (1 - p_0)(1 - P_{266}) \quad (7.2)$$

The (non-renormalized) population p_1 in the state and q_1 in all other states after the second step of the REMPD event is then:

$$p_1 = p_0(1 - P_{266})(1 - \beta P_r - \beta P_d) \quad (7.3)$$

$$\begin{aligned} q_1 &= q_{1,266} + p_{1,266}\beta P_r \\ &= (1 - P_{266})((1 - p_0) + p_0\beta P_r) \end{aligned} \quad (7.4)$$

The total fraction of molecules remaining is the sum:

$$p_1 + q_1 = (1 - P_{266})((1 - p_0) + p_0\beta P_r + p_0(1 - \beta P_r - \beta P_d)) \quad (7.5)$$

We chose in various contexts to measure using several consecutive pulses separated in time only by the pulsed laser repetition period and for this reason, a description of the surviving fraction of molecules after n successive REMPD events is necessary. If we consider the rotational transitions negligible on the time scale of the pulsed laser repetition period, 100 ms, we can propagate these quantities through another REMPD event.

It was experimentally verified that the fractional loss of molecules on subsequent events behaved according to the same ratio of magnetic substate addressing as the first event, implying that the time scale of the coupling between the magnetic substates was lower than 100 ms, so that memory of the selectivity of a P line REMPD event is lost in between subsequent REMPD events. We can thus proceed in exactly the same way as in the first event, so that after the first step of the second event we get

$$p_{2,266} = p_0(1 - P_{266})^2(1 - \beta P_r - \beta P_d) \quad (7.6)$$

$$q_{2,266} = (1 - P_{266})^2((1 - p_0) + p_0\beta P_r) \quad (7.7)$$

And after the second step:

$$p_2 = p_0(1 - P_{266})^2(1 - \beta P_r - \beta P_d)^2 \quad (7.8)$$

$$q_2 = (1 - P_{266})^2((1 - p_0) + p_0\beta P_r + p_0\beta P_r(1 - \beta P_r - \beta P_d)) \quad (7.9)$$

$$p_2 + q_2 = (1 - P_{266})^2((1 - p_0) + p_0\beta P_r + p_0\beta P_r(1 - \beta P_r - \beta P_d) + p_0(1 - \beta P_r - \beta P_d)^2) \quad (7.10)$$

The general result after n events is

$$p_n = p_0(1 - P_{266})^n(1 - \beta P_r - \beta P_d)^n \quad (7.11)$$

$$q_n = (1 - P_{266})^n \left((1 - p_0) + p_0\beta P_r \sum_{i=0}^{n-1} (1 - \beta P_r - \beta P_d)^i \right) \quad (7.12)$$

$$p_n + q_n = (1 - P_{266})^n \left((1 - p_0) + p_0 \beta P_r \sum_{i=0}^{n-1} (1 - \beta P_r - \beta P_d)^i + p_0 (1 - \beta P_r - \beta P_d)^n \right) \quad (7.13)$$

The interpretation of expression 7.13 for the fraction of surviving molecules $p_n + q_n$ is this: The factor $(1 - P_{266})^n$ is the fraction of molecules surviving the n two photon dissociations. The term $(1 - p_0)$ is the initial population in all other states, the term $p_0 \beta P_r \sum_{i=0}^{n-1} (1 - \beta P_r - \beta P_d)^i$ contains the population that has been sent from the addressed state to the other states through redistribution and the final term $p_0 (1 - \beta P_r - \beta P_d)^n$ is the population left in the addressed state.

Before proceeding to simplify this expression, we will relate this expression directly to the fractional loss of molecules after n consecutive REMPD events S_n . We note that $1 - S_n = p_n + q_n$ and introduce the shorthand notation

$$\delta_n = 1 - \frac{1 - S_n}{(1 - P_{266})^n} \quad (7.14)$$

$$\gamma = P_r + P_d \quad (7.15)$$

$$\eta = \frac{P_d}{P_r + P_d} \quad (7.16)$$

where η , as you will see, plays the same role as the η in the previous chapter. δ_n is the fractional loss of molecules S_n corrected for the two photon contribution from the 266 nm pulsed beam.

In this notation we have

$$\delta_n = p_0 - p_0 \beta \gamma (1 - \eta) \sum_{i=0}^{n-1} (1 - \beta \gamma)^i - p_0 (1 - \beta \gamma)^n \quad (7.17)$$

The sum consists of the first n terms of the well known geometric series:

$$\sum_{i=0}^{n-1} (1 - \beta \gamma)^i = \frac{1 - (1 - \beta \gamma)^n}{\beta \gamma} \quad (7.18)$$

We insert this and get

$$\delta_n = p_0 - p_0 \beta \gamma (1 - \eta) \frac{1 - (1 - \beta \gamma)^n}{\beta \gamma} - p_0 (1 - \beta \gamma)^n \quad (7.19)$$

and after some rearranging we obtain

$$\delta_n = p_0\eta(1 - (1 - \beta\gamma)^n) \quad (7.20)$$

We see that in the room temperature experiments, where $\gamma = 1$ and $n = 1$, equation 7.20 reduces to $\delta_n = p_0\eta\beta$, which is consistent with the data treatment applied to those experiments.

7.3.2 Experimental determination of γ and η

We first want to measure the value of $\gamma = P_r + P_d$. γ can be determined by fitting the expression of 7.20 to measurements of δ_n as a function of n , with $p_0\eta$ being one free parameter and γ being the other.

S_n was measured for $n = 1, 2, 3, 5$ on the R(1) transition with rotational cooling and corrected for the 266 contribution to obtain δ_n . As will be apparent later, when rotational cooling is applied, the population in $J = 2$ is negligible and any contribution from R(2) on the R(1) line can be neglected. Figure 7.5 shows the data and the result of the fit. The preliminary best fit parameters are $p_0\eta = 0.264 \pm 0.008$ and $\gamma = 0.88 \pm 0.07$.

With γ determined, we now turn our attention to η . We can find it by performing a sum of measurements over all populated lines in much the same way that the dissociation efficiency was determined in the room temperature trap. We see from equation 7.20 that

$$\frac{\delta_n}{1 - (1 - \beta\gamma)^n} = p_0\eta \quad (7.21)$$

which we can sum over all populated states to obtain

$$\sum_J \frac{\delta_n}{1 - (1 - \beta\gamma)^n} = \eta \quad (7.22)$$

since $\sum_J p_0 = 1$

We have two such distribution measurements we can use as a basis of a preliminary determination of η : The distribution without rotational cooling and the one with rotational cooling. For the distribution with cooling, states were probed through the transitions R(0), P(1), P(2), P(3), R(4) and R(5). In the uncooled case, $J = 6$ was also measured through the transition R(6). We use the γ determined above, the appropriate β factors and we take into account in the cooled case the reservoir of population in the $|v = 1, J = 1\rangle$

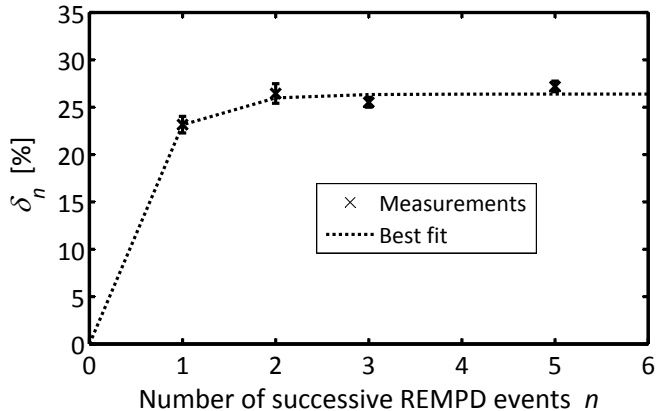


Figure 7.5: Preliminary data of the two photon corrected measurements δ_n on R(1) with rotational cooling as a function of the number of successive REMPd events n used for the measurement, along with the best fit to the data of the theoretical expression (equation 7.20). The preliminary best fit parameters are $p_0\eta = 0.264 \pm 0.008$ and $\gamma = 0.88 \pm 0.07$.

state equal to $3/5$ the population in $|v = 0, J = 2\rangle$ due to saturation of the cooling transition. $\eta = 0.947$ was determined for the cooled distribution and $\eta = 0.992$ was determined for the uncooled distribution. As our best preliminary estimate of η , we use the mean and standard deviation of those two values: $\eta = 0.970 \pm 0.023$. We can now conclude that $P_d = \gamma\eta = 0.85 \pm 0.07$ and $P_r = \gamma(1 - \eta) = 0.027 \pm 0.020$.

For reference, the ratios δ_n/p_0 are now calculated as a function of n and the transition used based on equation 7.20. These values are shown in table 7.1.

7.4 Ensemble state distribution measurements

After the initial setting up of the equipment was done and the REMPd scheme was optimized, the first thing to investigate was the time scales involved in equilibration, since this determined how long we would have to wait for each measurement. If the dynamics of the MgH^+ ions was that of a perfect 4K environment without collisions, the equilibration would be as shown in figure 7.4.

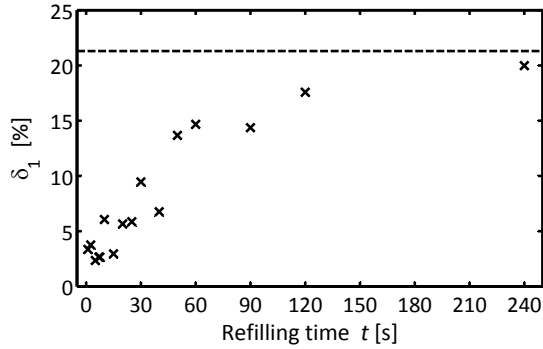
Transition	Correction factor δ_n/p_0				
	$n = 1$	$n = 2$	$n = 3$	$n = 4$	$n = 5$
P(1)	0.2834	0.4840	0.6260	0.7264	0.7975
P(2)	0.5102	0.7519	0.8665	0.9208	0.9465
P(3)	0.6074	0.8343	0.9191	0.9508	0.9626
P(4)	0.6613	0.8716	0.9385	0.9598	0.9665
P(5)	0.6957	0.8923	0.9478	0.9635	0.9679
any R	0.8503	0.9550	0.9679	0.9695	0.9697

Table 7.1: The preliminary correction factors that the two photon corrected measurements δ_n must be divided with to obtain the actual population in the addressed rotational state. This factor contains the effect of P transitions probing only $2J - 1$ out of $2J + 1$ magnetic substates and the effect of the preliminary finite dissociation probability P_d and redistribution probability P_r .

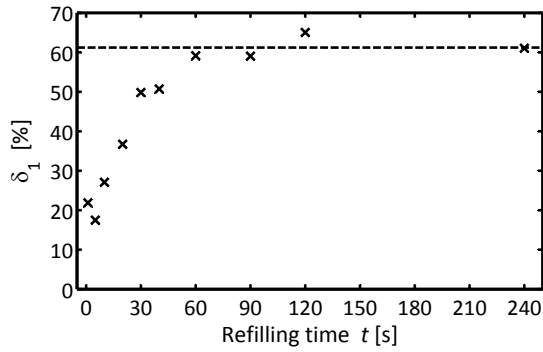
This did not prove to be the case, however. To obtain a measure of the effective rotational transition rates, we measured the rate at which the rotational states would re-fill themselves after being emptied by a single pair ($n = 1$) REMPD event. This was done with and without application of the rotational laser cooling and the results are shown in figure 7.6. The experimental procedure for this kind of measurement is the following:

1. Prepare a MgH^+/Mg^+ bicrystal ensemble in the ion trap and wait an 'infinite' time (≥ 4 min).
2. Shoot a single pair of pulses (an $n = 1$ REMPD event) on the state to empty it.
3. Wait a time t .
4. Shoot again with a single pair of pulses on the state.
5. Analyze the images to determine the fractional loss of molecules in the second event.

These refilling measurements yield the time scales for reobtaining equilibrium, which gives us a good indication of how long we have to wait in general before an ensemble is ready for measurements, either after the initial formation of the molecules through reactions or after a dissociation event. It is clear that



(a)



(b)

Figure 7.6: Preliminary data of the refilling of the $J = 0$ state addressed through the $R(0)$ transition. This was measured without and with application of the rotational laser cooling, shown in (a) and (b), respectively. The plotted quantity is δ_1 , which is proportional to and less than the population in the state. The infinite time asymptote is in both cases shown with the dashed line. In the uncooled case, the equilibrium is reached in about four minutes after the dissociation, while equilibrium is reached in about one minute in the cooled case.

the equilibrium is reobtained after four minutes in the uncooled case and after about one minute in the cooled case. The waiting times decided on for all subsequent measurements were four minutes and two minutes for the uncooled and cooled case, respectively.

These time scales are not consistent with the roughly 30 min expected for a hypothetical perfect 4 K black body radiation environment without collisions illustrated in figure 7.4. This could be due to collisions with background gas molecules that are not thermalized to 4 K or a more intense blackbody radiation field. Whatever the cause, I will in this thesis not attempt to model the dynamics but rather simply present preliminary measurements of rotational distributions.

Although it is too early to provide final numbers for the achieved populations and equivalent temperatures, the preliminary rotational distribution in CryP-TE_x with and without application of rotational laser cooling is presented in figure 7.7 along with two thermal Boltzmann distributions shown for estimates of best fit temperatures. Although neither of these distributions are expected to be thermal, a rough comparison reveals that the uncooled distribution seems to be best described by a temperature of about 38 K and the cooled distribution seems to be best described by a temperature of about 10 K.

To illustrate the effect of inserting the windows and aluminum discs into the 40 K environment, a preliminary comparison of the rotational distributions without rotational laser cooling before and after installation is shown in figure 7.8. Although the change did lower the effective temperature of the distribution, the change was not great.

7.5 Single ion measurements

As mentioned in section 6.4 in the chapter on the room temperature measurements, it is necessary to get rid of the micromotion as well to obtain truly cold molecules. Measurements on ensembles can be a fast way to troubleshoot equipment and may be perfectly fine for some types of experiments, but to perform a truly clean experiment where the ions do not exhibit micromotion, one has to go to the domain of single ions, which in the case of the linear Paul trap are resting on the radiofrequency field free center axis.

Working with single ions offers the additional benefit of the SCS_I-MS mass measurement technique that allows real-time monitoring of the mass of any co-trapped sympathetically cooled ion. Using this method it is, for example, possible to distinguish different isotopic compositions of the same molecule, something very important when applying resonant laser techniques to manipulate the ions.

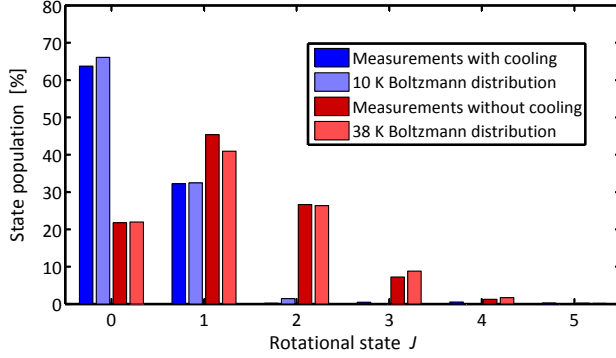


Figure 7.7: Preliminary data of the rotational distributions for MgH^+ ensembles in CryPTEX with and without rotational cooling applied. The raw data were measured on the lines R(0), P(1), P(2), P(3), R(4) and R(5) with three consecutive shots and the populations were calculated from equation 7.14 and table 7.1. Two thermal Boltzmann distributions are shown for comparison. A rough comparison reveals that the uncooled distribution seems to be best described by a temperature of about 38 K and the cooled distribution seems to be best described by a temperature of about 10 K.

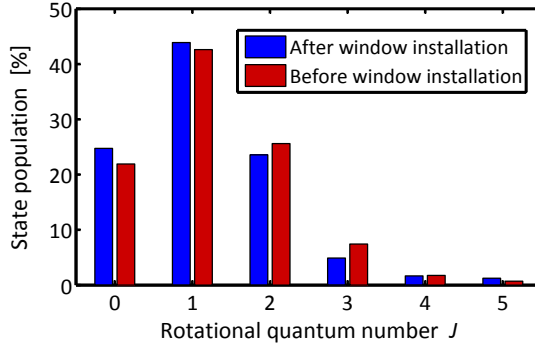


Figure 7.8: Preliminary data of the rotational distributions without rotational laser cooling before and after the installation of the windows and aluminum discs in the 40 K stage. The installation of the windows and discs seem to have had a small effect.

In an ensemble, removing and even identifying molecules with uncommon isotopes may in many cases be impossible and may lead to systematic errors.

For these reasons we measured the rotational distribution on single ions as well as ensembles by measuring the probability of dissociation. Measurements were made on R(0), P(1), P(2), P(3), R(4) and R(5) with 120, 193, 185, 162, 420 and 244 total dissociation attempts, respectively. For these measurements, the rotational laser cooling was applied and the mass of each molecular ion was verified to be 25 amu, consistent with $^{24}\text{MgH}^+$. The 68% confidence interval was calculated using the probability density function of equation 6.9 and the preliminary results are compared to ensemble measurements in figure 7.9. The two distributions seem to agree well, indicating that in the cryogenic environment of CryPTE_x, the micromotion does not couple significantly to the rotational degree of freedom, at least in this case where buffer gas cooling is not applied.

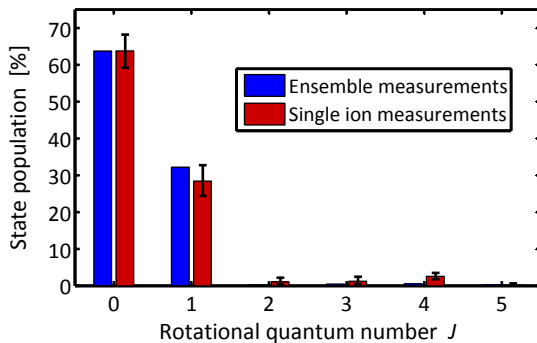


Figure 7.9: Preliminary data of the equilibrium rotational distributions with rotational laser cooling as measured with ensembles and with single ions. The error bars for the single ion measurements correspond to the 68% confidence interval of the likelihood distribution of equation 6.9. There seems to be good agreement between the single ion measurements and the ensemble measurements.

7.6 Helium buffer gas cooling

To investigate the effect of helium buffer gas cooling, the gas source previously used only for hydrogen was modified so that it could easily switch from delivering

hydrogen from a hydrogen bottle and helium from a helium bottle. In this way, after the usual reaction phase of an experiment, the gas delivery system could be switched over to helium and helium could be leaked in to a constant pressure to provide a background gas for buffer cooling of the molecular ions. The helium gas is expected to reach 4K rapidly due to collisions against the many 4K surfaces in the immediate vicinity of the trap center.

While the following data are also preliminary, a series of measurements were made to check the effect of the Coulomb crystal micromotion on the achieved equilibrium temperature. Since the molecules in smaller crystals reside at lower radial distances to the trap axis, their micromotion will, assuming unchanged trapping parameters a and q , be less energetic and the effective collisional temperature with a cold background gas will be lower. The characteristic temperature of the micromotion is on the order of tens of kelvin, so this addition to the collisional temperature was expected to have some effect on the final rotational distribution. To examine buffer gas cooling in the limit of no micromotion, we also carried out the same measurements on single ions residing on the center axis of the trap.

For these measurements, the rotational cooling laser was not applied. The effect of buffer gas cooling was observed to have reached a plateau at a partial pressure of helium of $\sim 2 \times 10^{-8}$ mbar, which was the pressure used for all the following measurements. Two different crystal sizes were used: 'large' crystals with a molecule mean kinetic energy due to micromotion of ~ 10 meV and 'small' crystals with a molecule mean kinetic energy due to micromotion of ~ 5 meV. The buffer gas cooling effect is clear, and a general trend for smaller crystals to be colder is clearly visible in the comparison, shown in figure 7.10. The single ion case stands out as the coldest, as was expected.

Although the data is preliminary, we can make a conservative upper bound on the characteristic temperature of the molecules. In figure 7.11, the single ion distribution is compared to a 10K Boltzmann distribution. From this, we conclude in the preliminary analysis that the ions have been buffer gas cooled to a temperature below 10K.

7.7 Measurement of the $\text{MgH}^+ |v = 1; J = 1\rangle_X \rightarrow |v = 0; J = 0\rangle_X$ decay rate

Determination of the critically important rovibrational decay rate from the $v = 1, J = 1$ state to the $v = 0, J = 0$ ground state was done by measuring the fast

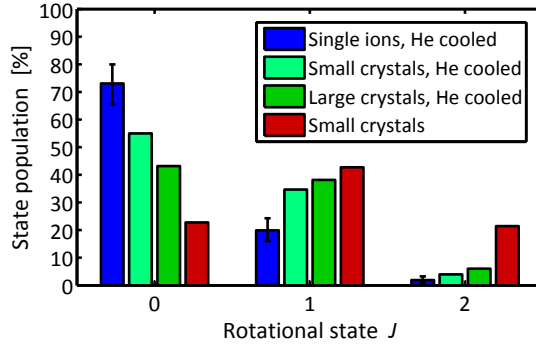


Figure 7.10: Preliminary data of the equilibrium rotational distributions without rotational laser cooling and with and without helium buffer gas cooling. The size of the crystals is qualitatively seen to have an effect, as would be expected due to the increased micromotion energy of the molecules in large crystals. The single ion case is clearly the coldest.

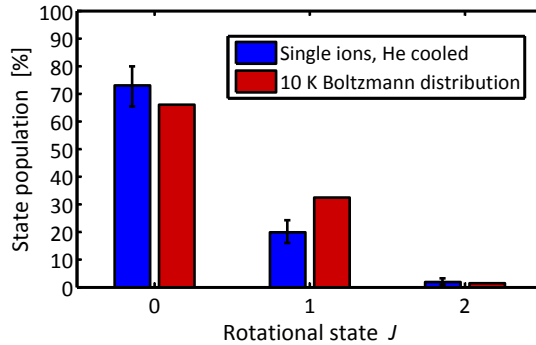


Figure 7.11: The single ion data of figure 7.10 compared to a Boltzmann distribution of 10 K. 10 K was chosen to represent a conservative upper bound on the characteristic temperature.

depletion of the $v = 0, J = 2$ state when applying the rotational cooling laser. Before laying out the theory, I will outline the steps of the experiment:

1. Prepare a MgH^+/Mg^+ bicrystal ensemble in the ion trap and wait 4 min for equilibration. During this, the rotational cooling beam is blocked by a shutter.
2. Open the shutter (rise time $\sim 200 \mu\text{s}$) to start the optical pumping of the rotational cooling scheme.
3. Wait a time t , where t is on the scale of the vibrational decay, about one second.
4. Shoot a single pair of pulses (an $n = 1$ REMPD event) on either line P(2) or R(0).
5. Analyze the images to determine the fractional loss of molecules, probing the population of state $J = 2$ or $J = 0$.

Let us denote the $|v = 0; J = 2\rangle_X$ state a , the $|v = 1; J = 1\rangle_X$ state b and the rovibrational ground state $|v = 0; J = 0\rangle_X$ c . The time-dependent populations in the three states are denoted $p_a(t)$, $p_b(t)$ and $p_c(t)$, respectively. The scheme is then the following: Upon application of the rotational cooling laser, the transition $a \leftrightarrow b$ is saturated and an equilibrium is achieved between those two states distributing the population equally over each magnetic substate. Since there are three magnetic substates in b and five in a we have, after application of the laser at $t = 0$,

$$p_b(t) = \frac{3}{5}p_a(t) \quad \text{for } t > 0 \quad (7.23)$$

This expression assumes both the rapid coupling between the magnetic substates of a mentioned in section 7.3.1 and rapid loss of coherence, which will become apparent as the lack of any distinguishable Rabi oscillations in the resulting decay measurement.

Now the molecules in state b can spontaneously decay to c according to equation 4.4 with $\rho(\omega_{cb}) = 0$:

$$\dot{N}_{cb}(t) = A_{cb}p_b(t) = A_{cb}\frac{3}{8}(p_b(t) + p_a(t)) \quad (7.24)$$

The characteristic time scale for the emptying of the strongly coupled a and b states through vibrational decay is thus $\frac{8}{3}A_{cb}$. The value for this Einstein A coefficient determined in section 4.1.5 is 6.14 Hz, corresponding to an expected

rate of depletion of the states of 2.30 Hz. The same time scale will be apparent if measuring $p_c(t)$ in this scheme. In addition to the initial population $p_c(0)$, the molecules that resided in a at $t = 0$ will move to c on the same time scale, 2.30 Hz.

To summarize, we expect the following curves:

$$p_a(t) = \begin{cases} p_a(0) & \text{for } t \leq 0 \\ \frac{5}{8}p_a(0)e^{-\frac{3}{8}At} & \text{for } t > 0 \end{cases} \quad (7.25)$$

$$p_c(t) = \begin{cases} p_c(0) & \text{for } t \leq 0 \\ p_c(0) + p_a(0)(1 - e^{-\frac{3}{8}At}) & \text{for } t > 0 \end{cases} \quad (7.26)$$

The preliminary data treatment of the measurements are shown in figure 7.12 along with the theoretical prediction of the above expressions. The agreement seems good, lending credibility to the determination of the Einstein A coefficients in general.

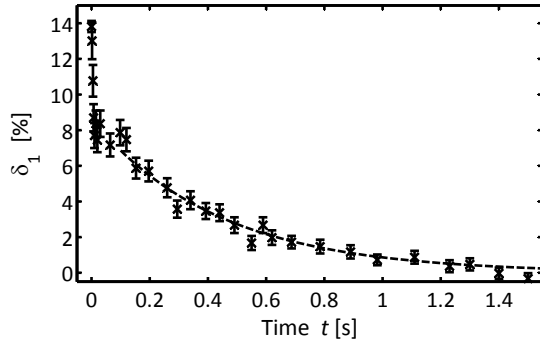
7.8 Preliminary conclusions

From the measurements and analysis made so far on the CryPTEx experiments on MgH^+ ions, we can conclude a few things of major importance.

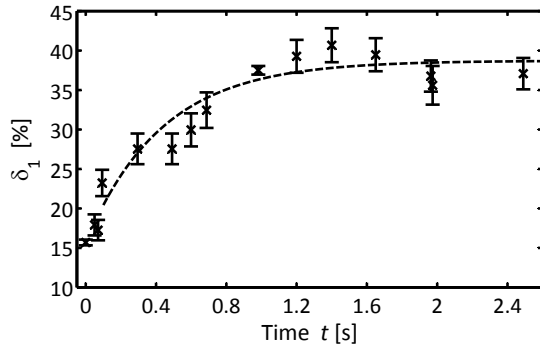
Even though the cryogenic environment of CryPTEx is comparatively well-shielded after the addition of the windows and discs in the 40 K stage and the pressure at the position of the ions is expected to be lower than 10^{-13} mbar, neither the equilibration times nor the equilibrium rotational distribution are consistent with a 4 K black body radiation environment without background collisions. Instead, the rotational distribution corresponds best to a Boltzmann distribution at about 38 K. The molecular ions were further cooled by the application of the rotational cooling laser, decreasing the characteristic rotational temperature to about 10 K.

An important take-away message from this is that, in some cryogenic environments, it will not be possible to make the assumption that the ions equilibrate internally to the temperature of the cryogenic environment. To make a claim as to the rotational distribution or internal temperature of molecules, it is in general necessary to have a direct means of measuring the rotational distribution such as the REMPD scheme implemented in our setups.

In the spirit of migrating towards performing experiments on micromotion-free ions, rotational distribution measurements were performed on rotationally



(a)



(b)

Figure 7.12: Preliminary data showing in (a) the depletion of the $J = 2$ state and in (b) the corresponding filling of the $J = 0$ state. The plotted quantity is δ_1 , which is proportional to and less than the population in the state. The dashed curves are the theoretical predictions based on expressions 7.25 and 7.26 with the Einstein A coefficient calculated in 2012 ($\frac{3}{8}A_{cb} = 2.30$ Hz). Although the results are preliminary, the agreement looks good.

cooled single ions as well, since these reside on the micromotion free center axis of the trap. Although single ion rotational cooling had been briefly investigated in the room temperature chamber, the measurements made in CryPTEx are much more detailed and conclusive. The probability of the molecule residing in each addressed state corresponds closely with the population in the state for the Coulomb crystal ensembles, demonstrating the feasibility and validity of measuring rotational distributions on single ions. Additionally, due to the agreement between the distributions, the micromotion in Coulomb crystals seems to have little effect on the rotational temperature in the absence of buffer gas.

Subsequently, the effect of helium buffer gas cooling was measured on single ions and with small and large crystals. The characteristic rotational temperature of the single ions with helium buffer gas cooling and without rotational laser cooling seems in the preliminary analysis clearly below 10 K. Comparing this to the equilibria for the ensembles illustrates that in order for buffer gas cooling to work to its maximum extent, one must operate in a micromotion-free regime such as that of ions on a string in a linear Paul trap.

To test the validity of the Einstein A coefficients calculated in 2012, the vibrational decay rate from the $v = 1, J = 1$ state to the $v = 0, J = 0$ ground state was measured using the REMPD scheme and the rotational cooling laser. The rate of this decay is fast enough that rotational dynamics and background collisions can be neglected, providing a clear measurement of this important quantity. The agreement with theory is good, lending credibility to both the *ab initio* calculations of the A coefficients and the measurement method.

The following three points are the main conclusions of this chapter:

1. In general, direct measurements of the rotational distribution of molecules are necessary to make a statement regarding their rotational temperature.
2. Measuring the rotational distribution of a single molecular ion is feasible—essentially a temperature probe in a single point in space!
3. While micromotion plays an important role in the equilibrium distribution achieved with buffer gas cooling, its effect on the rotational distribution in the absence of buffer gas seems negligible. The micromotion will of course still adversely impact various experiments due to its kinetic energy contribution.

Ca⁺ + HD recycling reactions experiment

One of the great applications of cold atoms and molecules is to study the fascinating chemical phenomena that arise when the reaction energies are very low. This field is called cold or ultracold chemistry depending on the temperature and provides a new type of window into the quantum world.

To work towards cold chemistry experiments, we carried out an experiment studying the reaction between Doppler laser cooled Ca⁺ ions and room temperature hydrogen (H₂) and hydrogen deuteride (HD) molecules in a linear Paul trap. The experiment served three main purposes: To determine a value for the rate constant of the reaction, to determine the relative formation probability of the two possible products, CaD⁺ and CaH⁺, and to demonstrate a method of regenerating the original atomic reactant ion by means of photodissociation after each reaction. The experiments were finished around July 2010 and published in *Angewandte Chemie* in July 2012 [111].

8.1 Motivation

Various challenges face the experimentalist who wishes to perform cold and ultracold chemistry. All degrees of freedom have to be cold, ideally cooled to the ground state to obtain the greatest degree of knowledge of the system. Cold reactions with atoms requires cooling of their translational degree of freedom, while molecules additionally require cooling of their internal degrees of freedom such as the rotational cooling demonstrated in chapters 6 and 7.

To reach the lowest translational temperatures, atomic ions trapped in a Paul trap must reside at points that are free from the radiofrequency (rf) field such that micromotion, with a temperature often on the order of tens of kelvin, is avoided. This can be accomplished by trapping the ions on a string on the rf free center axis of a linear Paul trap such as the ones used in the Ion Trap Group. Cold ion chemistry is thus limited to having few ions in the trap at a time and, indeed, experimenting with just a single reaction target ion sympathetically cooled by a single Doppler cooled ion offers a variety of important fundamental advantages over, for example, Coulomb crystal ensemble measurements.

These advantages include enabling the use of the SCSI-MS technique (section 2.1.5) to identify the trapped ions with certainty. Any impurities that might be undetectable and unremovable in an ensemble are easily detectable and discardable in the single ion case. Another advantage is that the use of image analysis

algorithms for determining the number of atoms and molecules in an ensemble become unnecessary, eliminating another potential source of systematic errors.

To extend into the field of ultracold chemistry, the temperatures have to be below 1 mK and Doppler laser cooling is no longer enough to reach such low temperatures. Starting from typical Doppler cooling temperatures slightly above 1 mK, sideband cooling [66] can be applied to cool the translational degree of freedom to the ground state of the trapping potential, resulting in temperatures on the order of tens of microkelvins.

Such translational state preparation requires a great deal of control over the trapping voltages and it is essential to avoid patch potentials that may arise on the insulating surfaces near the trap center due to the atomic beam or photoionization beam involved in the loading process of the trap. For this reason, the ability to regenerate by photodissociation an ion that has reacted is an important tool removing the need to reload the trap after every reaction measurement. This not only saves time and enables better sideband cooling by providing greater control of the electric fields in the trap but also enables experiments with ion species that are very infrequently produced.

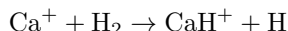
Such ions could include rare or unstable isotopes of common elements or even transactinides (atomic number $Z \geq 104$), with half-lives of up to 32 h [112] and very low production rates of sometimes only a few detected per day at only a few accelerator facilities worldwide.

Besides the demonstration of the useful tool of photodissociation as a means of regenerating the reactant ion in ion chemistry experiments, our measurements of the branching ratio of the $\text{Ca}^+ + \text{HD}$ reaction are highly relevant to the chemistry in interstellar clouds [113] and in general provide experimental data for theoretical chemists to test their reaction dynamics modelling [114] against, especially when compared to similar measurements performed previously on the $\text{Mg}^+ + \text{HD}$ reaction with electronically excited single ions [115] and with ground state ions in beam experiments [116]. Additionally, the determined reaction rate constant can also be compared to that of the $\text{Mg}^+ + \text{HD}$ reaction and serves as another test for theoretical models. Potential curves for the CaH_2^+ reaction complex are available in the literature [117], as well as a general *ab initio* study of MH_2^{n+} ($\text{M} = \text{Li}, \text{Be}, \text{Na}, \text{Mg}, \text{K}, \text{Ca}; n = 1, 2$) complexes [118].

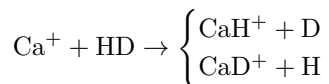
8.2 Theory

In the experiment, two Ca^+ ions are co-trapped and Doppler cooled with trapping parameters chosen such that $\omega_r > \omega_z$, so that the ions lie next to each

other on the center axis of the trap. Just as for Mg^+ ions, a reaction with H_2 or HD can occur from the P state involved in the Doppler cooling scheme, but is not energetically possible if the Ca^+ ion resides in the S ground state or the D shelving state in the Doppler cooling scheme. To stimulate this reaction, the excitation rate of the Doppler cooling is increased to maximize the time averaged population in the P state, while extra H_2 or HD gas is introduced through a leak valve. A reaction with an H_2 molecule can only proceed according to



while a reaction with an HD molecule can have two outcomes:



A reaction is apparent by the vanishing of the fluorescence from one of the ions and the identity of the formed molecular ion is determined using the SCSIMS technique, introduced in section 2.1.5. In this technique, the resonance frequency of the ions' axial motion is measured and referenced against equation 2.15 to reveal the mass of the molecular ion. Some experiments were performed with the most naturally abundant isotope of calcium, ^{40}Ca , in which case CaH^+ has a mass of 41 amu and CaD^+ has a mass of 42 amu. Other measurements were performed with the rare isotope ^{48}Ca , in which case CaH^+ had mass 49 amu and CaD^+ mass 50 amu.

The identification of the molecule constitutes one gathered data point and one would like to prepare a new set of two co-trapped Ca^+ ions to serve as the reaction target. While it would be possible to simply eject the two ions from the trap and load two new Ca^+ ions, a core principle of the experiment was the demonstration of photodissociation of the CaH^+ or CaD^+ ion to reobtain the original Ca^+ ion. As it turns out, a laser beam with a wavelength of 272 nm has the right energy to excite the molecule from its ground state X to the Franck-Condon point of the dissociating C state, which means that the Ca photoionization beam can also be used for $\text{CaH}^+/\text{CaD}^+$ photodissociation.

In figure 8.1, illustrations are provided of the Doppler cooling level scheme, the disappearance of fluorescence at a reaction event and the level scheme of CaH^+ as determined by Boutalib, Daudey and Mouhtadi [119].

8.2.1 Modelling the reaction process

The model we have chosen to describe the reaction process between Ca^+ and H_2/HD is the two step model also used in the article on reactions between Mg^+

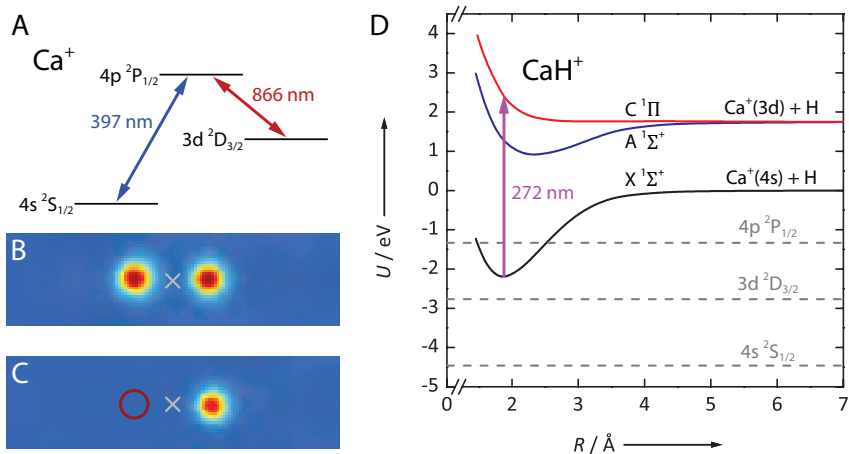


Figure 8.1: A: The level scheme of Ca^+ ions showing the Doppler laser cooling transitions. The main cooling transition is addressed with 397 nm light, while the repumping laser beam at 866 nm prevents shelving in the $^2D_{3/2}$ state. B: False color image showing two Ca^+ ions fluorescing due to the Doppler cooling. The trap center is shown with the gray cross and the horizontal extent of the image is 22 μm . C: After a reaction, the trap contains one fluorescing Ca^+ ion and one nonfluorescing $\text{CaH}^+/\text{CaD}^+$ ion, indicated by the red circle. D: The relevant lowest lying singlet potential curves for CaH^+ [119]. The horizontal dashed lines show the energies of the populated electronic states of Ca^+ shifted down by the binding energy of the HD molecule. It is clear that only the P state contributes enough energy to form CaH^+ . The photodissociation transition is indicated by the violet arrow.

and H₂/HD/D₂ [52]. First, the neutral molecule is captured by the Ca⁺ ion at long range to form a CaH₂⁺/CaHD⁺ collision complex. In the second step, a stable molecular ion CaH⁺/CaD⁺ may be formed from this complex.

The first step is, as in section 6.3.1, characterized by the Langevin capture cross section [107]

$$\sigma = \frac{e}{2\epsilon_0} \sqrt{\frac{\alpha}{\mu v^2}} \quad (8.1)$$

where α is the mean polarizability of the neutral, μ is the reduced mass of the ion-neutral system and v_r is the relative velocity in the ion-neutral center of mass frame. In the case of an ion stationary in the laboratory frame, the relative velocity is equal to the velocity of the neutral in the laboratory frame, v . Using n as the density of molecules, the collision rate Γ_c is then

$$\Gamma_c = nv\sigma = n \frac{e}{2\epsilon_0} \sqrt{\frac{\alpha}{\mu}} \quad (8.2)$$

which is independent of the velocity v .

The molecular ion formation rate is then given by

$$\Gamma = p_{\text{exc}} \eta \Gamma_c \quad (8.3)$$

where p_{exc} is the probability of finding the Ca⁺ ion in the excited P state from which the reaction is energetically allowed and η is the probability for formation of the molecular product in the second step in the case of collision with an ion in the P state. In these experiments, there are three such probabilities: $\eta_{\text{CaD}^+}^{\text{HD}}$, $\eta_{\text{CaH}^+}^{\text{HD}}$ and $\eta_{\text{CaH}^+}^{\text{H}_2}$, where the subscript denotes the product and the superscript denotes the reactant molecule.

In the experiments performed, the background gas would always contain some non-negligible amount of H₂ besides HD, so the effect of H₂ in the gas mixture is taken into account by measuring the fractional formation of CaD⁺ $N_{\text{CaD}^+}/(N_{\text{CaD}^+} + N_{\text{CaH}^+})$ at various values of the relative HD pressure $P_{\text{HD}}/(P_{\text{HD}} + P_{\text{H}_2})$ and extrapolating to the case of a pure HD gas using the formalism below. The relative HD pressure could be regulated in a controlled way by preparing a mixture in a reservoir connected to the leak valve.

For a given experiment with HD partial pressure P_{HD} and H₂ partial pressure P_{H_2} , we measure the amount of reactions that lead to formation of CaH⁺,

N_{CaH^+} , and formation of CaD^+ , N_{CaD^+} . We have

$$\begin{aligned} \frac{N_{\text{CaD}^+}}{N_{\text{CaD}^+} + N_{\text{CaH}^+}} &= \frac{\Gamma_{\text{CaD}^+}}{\Gamma_{\text{CaD}^+} + \Gamma_{\text{CaH}^+}} \\ &= \frac{\eta_{\text{CaD}^+}^{\text{HD}} \Gamma_{\text{c}}^{\text{HD}}}{\eta_{\text{CaD}^+}^{\text{HD}} \Gamma_{\text{c}}^{\text{HD}} + \eta_{\text{CaH}^+}^{\text{HD}} \Gamma_{\text{c}}^{\text{HD}} + \eta_{\text{CaH}^+}^{\text{H}_2} \Gamma_{\text{c}}^{\text{H}_2}} \end{aligned} \quad (8.4)$$

Since the polarizabilities of H_2 and HD are equal to within 1%, we here take the polarizabilities to be identical. Using that partial pressure is proportional to density, we then have

$$\frac{N_{\text{CaD}^+}}{N_{\text{CaD}^+} + N_{\text{CaH}^+}} = \frac{\eta_{\text{CaD}^+}^{\text{HD}} \frac{P_{\text{HD}}}{\sqrt{\mu_{\text{HD}}}}}{\eta_{\text{CaD}^+}^{\text{HD}} \frac{P_{\text{HD}}}{\sqrt{\mu_{\text{HD}}}} + \eta_{\text{CaH}^+}^{\text{HD}} \frac{P_{\text{HD}}}{\sqrt{\mu_{\text{HD}}}} + \eta_{\text{CaH}^+}^{\text{H}_2} \frac{P_{\text{H}_2}}{\sqrt{\mu_{\text{H}_2}}}} \quad (8.5)$$

which we can rearrange to the form

$$\frac{N_{\text{CaD}^+}}{N_{\text{CaD}^+} + N_{\text{CaH}^+}} = A \frac{x}{x + (1-x)B} \quad (8.6)$$

where

$$x = \frac{P_{\text{HD}}}{P_{\text{HD}} + P_{\text{H}_2}} \quad (8.7)$$

$$A = \frac{\eta_{\text{CaD}^+}^{\text{HD}}}{\eta_{\text{CaD}^+}^{\text{HD}} + \eta_{\text{CaH}^+}^{\text{HD}}} \quad (8.8)$$

$$B = \frac{\eta_{\text{CaH}^+}^{\text{H}_2}}{\eta_{\text{CaD}^+}^{\text{HD}} + \eta_{\text{CaH}^+}^{\text{HD}}} \sqrt{\frac{\mu_{\text{HD}}}{\mu_{\text{H}_2}}} \quad (8.9)$$

Expression 8.6 can then be fitted to data points gathered at various x values. The extrapolation to $x = 1$ then reflects the case of a pure HD gas and the fractional formation of CaD^+ there is simply given by the fitting parameter A . B is also an interesting figure, since it is the ratio of probabilities of formation of any stable molecule in a collision with H_2 to that in a collision with HD, multiplied by $\sqrt{\mu_{\text{HD}}/\mu_{\text{H}_2}}$. $\sqrt{\mu_{\text{HD}}/\mu_{\text{H}_2}}$ is 1.210 for $^{40}\text{Ca}^+$ and 1.213 for $^{48}\text{Ca}^+$.

8.3 Experimental procedure

Experiments involving Ca^+ ions share many methods with those with Mg^+ ions. The laser sources are different: The Doppler cooling light at 397 nm is generated

for these experiments from frequency doubling a Ti:Sa laser, two diode lasers at 866 nm and 854 nm excite repumping transitions and the 272 nm photoionization is performed with the twice frequency doubled output of a fiber laser.

Each step of the experiment has been explained in the previous sections, but here the steps are summarized for clarity and reference:

1. Starting with an empty ion trap, the shutter blocking the atomic Ca beam inside the vacuum chamber is moved to admit a beam of Ca atoms through the trap center.
2. The photoionizing beam at 272 nm is admitted in short pulses to the trap center, intersecting the atomic beam at a right angle. This slowly creates Ca^+ ions, which are initially hot.
3. At all times, the Doppler cooling beam at 397 nm and the repumper beam at 866 nm also pass through the trap center, cooling the Ca^+ ions down to millikelvin temperatures within milliseconds. When two Ca^+ ions have been produced, the ion loading process is stopped by blocking the photoionizing beam and the atomic beam. The two ions arrange themselves next to each other on the center axis of the trap and the imaging system provides real time observation of the fluorescence emitted by the ions.
4. The desired gas (H_2 , HD or a mixture) is introduced through a leak valve to start the reaction. To increase the rate of reactions, the Doppler cooling laser powers and detunings are at this point optimized for maximum fluorescence. Since the fluorescence of the ions is proportional to the time averaged probability of finding the ion in the P state, which in turn is proportional to the reaction rate, maximizing fluorescence means maximizing the reaction rate.
5. Once an ion reacts, it remains sympathetically cooled by the unreacted Ca^+ ion and the identity of the formed molecule is determined using the SCS-MS technique. This identification is fast enough that it is not necessary to stop the flow of gas into the chamber.
6. After successful identification, a short (~ 100 ms) pulse of 272 nm light is introduced, photodissociating the molecule to regenerate the original Ca^+ ion. Go to step 5.

A total of 263 reactions were recorded at four different relative partial pressures for the most abundant isotope of calcium, $^{40}\text{Ca}^+$ to provide data for the

fit determining the A and B parameters of equation 8.6. After those measurements we switched to the rare $^{48}\text{Ca}^+$ isotope (isotopic abundance 0.189%) and recorded a total of 87 reactions in an eight hour long series using the same two ions throughout the whole series, regenerating them through photodissociation after each reaction.

Since reactions with H_2 and HD occur with much lower probability for Ca^+ ions than for Mg^+ , it was necessary to raise the partial pressure two orders of magnitude higher than what had been necessary in the Mg^+ experiments. The vacuum chamber pressure during the eight hour long series was thus kept constant at 1×10^{-7} mbar to ensure reactions would happen frequently enough.

8.3.1 q -purification of impurity ions

Occasionally during the experiments, a non-fluorescing third ion would enter the trap and become sympathetically cooled by the Doppler cooled Ca^+ ions. Although it is still not clear where these ions come from, we could remove them from the trap by performing q -purification (see section 2.1.2), that is, changing the amplitude of the radiofrequency voltage component applied to the trap electrodes. Some ions were lighter than the Ca^+ ions and could be removed by increasing the amplitude of the radiofrequency field, while others were heavier and were purged by lowering the amplitude.

During the eight hour long $^{48}\text{Ca}^+$ series, 27 such unwanted ions were purged from the trapping region while leaving the two $^{48}\text{Ca}^+$ ions in the trap.

8.4 Results

One way to illustrate the progression of the experiment is through the use of a trace of the fluorescence integrated over the whole imaging area as a function of time. This is shown in figure 8.2 along with a collection of images recorded during the experiment.

8.4.1 Determination of the reaction rate constant

Also shown in the trace of figure 8.2 is the time until reaction τ , defined as the time from a photodissociation event to the following reaction event, from which we can determine the reaction rate constant Γ_{P}/n for reaction between a $^{48}\text{Ca}^+$ ion in the P state and the used gas mixture. The gas mixture had a total pressure of 1×10^{-7} mbar and $P_{\text{HD}}/(P_{\text{HD}} + P_{\text{H}_2}) = 0.83$. Since the reactivities

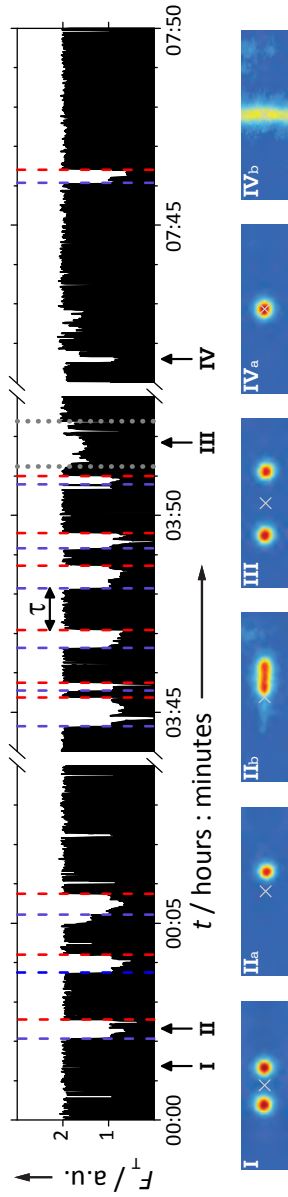


Figure 8.2: Top: Graph showing the integrated fluorescence over the whole imaging area as a function of time. The units are arbitrary but correspond roughly to the fluorescence caused by one fluorescing $^{48}\text{Ca}^+$ ion. The blue dashed lines indicate times at which a reaction occurred, and the red dashed lines indicate the dissociation events in which the original $^{48}\text{Ca}^+$ ion was regenerated. The gray dotted lines indicate an interval where an impurity ion was present in the trap. Bottom: Images of the ions at various points during the experiment with the trap center shown with the gray cross. I: Pre-reaction. IIa: Post-reaction, not on SCSL-MS resonance. IIb: Post-reaction, on SCSL-MS resonance. III: Two $^{48}\text{Ca}^+$ ions and a non-fluorescing impurity ion. IVa: One ion temporarily hot due to a non-reactive collision with background gas. IVb: Both ions temporarily hot due to a non-reactive collision with background gas.

of the CaHD^+ collision complex turn out to be equal to the reactivity of the CaH_2^+ collision complex within the error bars, the rate constant should also be representative of reactions with pure H_2 or pure HD gas.

Recall that we model the reaction process as equation 8.3. The molecular ion formation rate for ions in the P state is then

$$\Gamma_{\text{P}} = \frac{\Gamma}{p_{\text{exc}}} = \eta n v \sigma \quad (8.10)$$

Since the mean time until reaction τ in this case is equal to Γ^{-1} , we get the reaction rate constant

$$\frac{\Gamma_{\text{P}}}{n} = \eta v \sigma = \frac{1}{\tau n p_{\text{exc}}} \quad (8.11)$$

The excitation probability p_{exc} was calculated from the total fluorescence signal captured by the imaging system. A calibration was carried out to determine the sensitivity of the image intensifier and camera system by sending a highly attenuated laser beam of 397 nm light with well known power onto the image intensifier and referencing this to the integrated CCD chip pixel response. Losses of the optics (vacuum chamber imaging window, imaging lens) were estimated to 8 % and the solid angle of collection of the fluorescence photons was geometrically calculated to be $4\pi \times 1.2\%$. The calculated total power of fluorescence emission of each Ca^+ ion was determined as a function of time during the experiment, taking into account a small drift of the power of the 397 nm light over the eight hour period of data gathering. This emitted power was then compared to the theoretical instantaneous power of emission of a Ca^+ ion 100 % prepared in the P state. The result is $p_{\text{exc}} = 3.7\%$, slightly dependent on the time during the experiment.

After normalizing of the times until reaction to the time dependent excitation probability $\tau_{\text{N}} = \tau/p_{\text{exc}}$, the values are plotted in a histogram shown in figure 8.3.

The maximum likelihood estimate of $\bar{\tau}_{\text{N}}$ is 6.6 s with a 68.3 % confidence interval of 5.9 s to 7.5 s. From this mean value and the gas molecule density $n = P/(k_{\text{B}}T)$ we find a reaction rate constant Γ_{P}/n on the order of $3 \times 10^{-11} \text{ cm}^3 \text{ s}^{-1}$.

8.4.2 Determination of reactivity ratios

The $N_{\text{CaD}^+}/(N_{\text{CaD}^+} + N_{\text{CaH}^+})$ values recorded for the four different pressure ratios for $^{40}\text{Ca}^+$ and the one pressure ratio for $^{48}\text{Ca}^+$ are shown in figure 8.4

along with the fit of equation 8.6 to the data. The best fit is obtained with $A = 0.59 \pm 0.03$ and $B = 1.3 \pm 0.2$.

From the fitting parameters we conclude that

$$\frac{\eta_{\text{CaD}^+}^{\text{HD}}}{\eta_{\text{CaD}^+}^{\text{HD}} + \eta_{\text{CaH}^+}^{\text{HD}}} = A = 0.59 \pm 0.03$$

$$\frac{\eta_{\text{CaH}^+}^{\text{H}_2}}{\eta_{\text{CaD}^+}^{\text{HD}} + \eta_{\text{CaH}^+}^{\text{HD}}} = \frac{B}{\sqrt{\frac{\mu_{\text{HD}}}{\mu_{\text{H}_2}}}} = 1.1 \pm 0.2$$

and we can see that the data point taken with the two $^{48}\text{Ca}^+$ ions agrees with the $^{40}\text{Ca}^+$ data within the error bars.

8.4.3 Photodissociation of CaO^+ and CaOH^+

While performing the $^{40}\text{Ca}^+$ measurements, a few times we observed reactions resulting in molecules of mass 56 amu and mass 57 amu. It turned out that these molecules were also dissociatable with the 272 nm beam, although a longer (~ 5 s) exposure was necessary to induce the dissociation.

Thinking that these molecules might be CaO^+ and CaOH^+ , we verified that introduction of O_2 and H_2O , respectively, did indeed induce these reactions. While introducing O_2 , three reactions lead to formation of a molecule with mass 56 amu, assumed to be CaO^+ . Introduction of H_2O resulted in 14 molecules with mass 57 amu, assumed to be CaOH^+ . All of these were dissociated using a few seconds of 272 nm light exposure. Although the potential curves of CaO^+ and CaOH^+ are different to those of CaH^+ , it seems that the energy of 272 nm photons still enables a weak coupling to a dissociation continuum for those molecules.

8.5 Comparison with $\text{Mg}^+ + \text{HD}$ results and conclusions

To summarize the results of these experiments, the isotope dependence of the $\text{Ca}^+(4p \ ^2P_{1/2}) + \text{HD}$ reaction was determined in terms of the reactivity ratios, revealing a slight preference for formation of CaD^+ with reactivity ratio $59 \pm 3\%$. A comparison with the measurements previously performed on $^{26}\text{Mg}^+(3p \ ^2P_{3/2})$ ions is shown in figure 8.5.

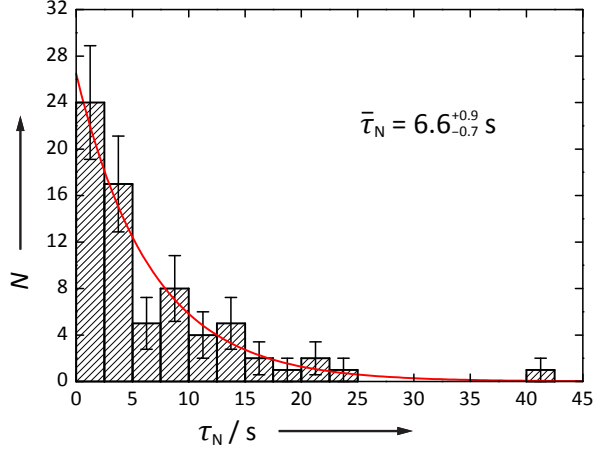


Figure 8.3: A histogram of the normalized times until reaction τ_N . The maximum likelihood estimate of $\bar{\tau}_N$ is 6.6 s with a 68.3% confidence interval of 5.9 s to 7.5 s. As a guide to the eye, the red curve is an exponential decay with a time constant 6.6 s.

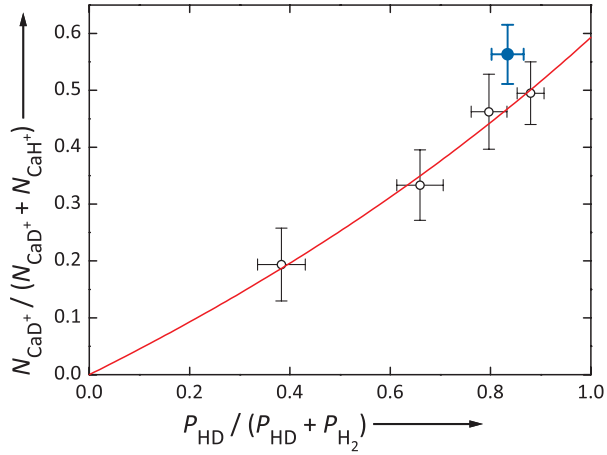


Figure 8.4: Graph of the relative formation of CaD^+ versus the pressure ratio of the gas mixture used. Expression 8.6 is fitted to the data gathered for the $^{40}\text{Ca}^+$ isotope. The best fit is shown in the red curve and has $A = 0.59 \pm 0.03$ and $B = 1.3 \pm 0.2$.

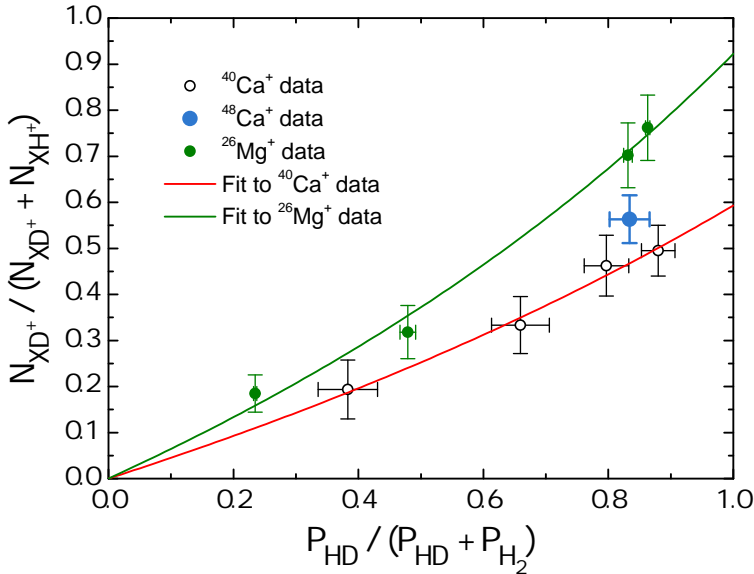


Figure 8.5: Graph of the relative formation of CaD^+ or MgD^+ versus the pressure ratio of the gas mixture used. Expression 8.6 is fitted to the data gathered for the $^{40}\text{Ca}^+$ isotope and for $^{26}\text{Mg}^+$. A marked difference in isotope effect is seen between Ca^+ and Mg^+ .

Ca and Mg reside in the same group in the periodic table and might naively be expected to exhibit the same chemical behavior. Nevertheless, these experiments have shown that there is a marked difference in isotope preference in reactions between their electronically excited ions and HD gas.

The fact that a reaction rate constant $\sim 3 \times 10^{-11} \text{ cm}^3 \text{ s}^{-1}$ and a fractional CaD^+ formation rate 0.56 ± 0.05 was determined using only one pair of $^{48}\text{Ca}^+$ ions demonstrates the usefulness of the regeneration scheme. The fact that CaO^+ and CaOH^+ molecules were also dissociatable with the same wavelength lends credibility to the generality of the approach. Using more than one laser, even more complex molecules could be regenerated in this type of experiment.

Although these reactions were carried out between cold ions and room temperature molecules, the extension to reacting with cold molecules is straightforward with the use of, for example, a state-specific velocity filter, a Stark decelerator or a Zeeman decelerator.

Summary

In this thesis I have presented results which demonstrate the implementation and measurement of laser-induced cooling of the rotational degree of freedom of MgH^+ ions confined in an ion trap. The merit of a two color REMPD rotational distribution measurement scheme is shown by the excellent agreement between the uncooled distribution in the room temperature environment and a 297 K Boltzmann distribution.

Cooling the internal rotational degree of freedom to the equivalent of an 18 ± 2 K thermal distribution with regard to the ground state population demonstrates the applicability of this new cooling scheme for generating cold molecules in a laboratory, both for ensembles and single ions. With suitable mid-infrared laser sources, such a scheme should be generally applicable to any polar diatomic molecule that can be held localized for minutes, for example, via sympathetic cooling in an ion trap.

Dissociative state preparation was performed on single ions in the room temperature ion trap, leading to ground state preparation probabilities of 64 % to 68 %, depending on the simulation model applied.

In addition to this, the rotational distribution of MgH^+ inside the cryogenically cooled environment of the CryPTEEx trap constructed at the Max-Planck-Institut für Kernphysik in Heidelberg was measured and corresponds in the preliminary analysis to a temperature of about 38 K. With the addition of the rotational laser cooling, the characteristic rotational temperature dropped to about 10 K in the preliminary analysis.

Detailed measurements of the rotational distribution of single ions was shown in the CryPTEEx trap to be feasible, constituting in a sense a temperature probe in a single point in space. Experiments with single ions are often preferable compared to ensemble experiments in part because of the applicability of the SCS-MS technique to verify the identity of the molecule being experimented on and in part because single ions on the center axis of the trap are to good approximation free from micromotion.

10 K was also the conservative upper bound on the characteristic temperature when cooling single ions with helium buffer gas without the use of rotational laser cooling. Helium buffer gas cooling of Coulomb crystal ensembles was shown to equilibrate to temperatures higher than the single ion case, presumably due to the increased micromotion energy of the molecules when off-axis.

A measurement of the $\text{MgH}^+ |v = 1; J = 1\rangle_X \rightarrow |v = 0; J = 0\rangle_X$ decay rate

was performed and found in preliminary analysis to be in agreement with the new Einstein A coefficients calculated in 2012 with the assistance of theoretical chemist Frank Jensen from the Department of Chemistry at Aarhus University. This lends credibility to the accuracy of the simulation of the radiative dynamics involved in the rotational laser cooling process. However, the spectral energy density of the background radiation may still be difficult to estimate in environments with non-blackbody surfaces and non-uniform temperature, just as the influence of background collisions on the applied cooling scheme.

The experiment concerning the branching ratio of the $\text{Ca}^+ + \text{HD}$ reaction was also successfully concluded and shows the benefits of applying photodissociation regeneration in a single ion experiment. From only a single pair of the isotopically rare $^{48}\text{Ca}^+$ ions, a reaction rate constant of $\sim 3 \times 10^{-11} \text{ cm}^3 \text{ s}^{-1}$ and a fractional CaD^+ formation rate of $56 \pm 5\%$ were determined. The possibility of performing many reaction measurements without reloading ions into the trap makes new experiments possible, e.g., chemistry studies involving radioactive transactinide elements which currently suffer from very low rates of production and have half-lives of the order of hours.

Additionally, the reactivity ratio describing the preference of $^{40}\text{CaD}^+$ formation over $^{40}\text{CaH}^+$ for reactions with a pure HD gas was found to be $59 \pm 3\%$, in contrast to similar measurements made with $^{26}\text{Mg}^+$ ions. Any future theoretical modelling of the $\text{Ca}^+/\text{Mg}^+ + \text{HD}$ reaction dynamics will have to be able to reproduce these results.

Appendix A

The Mg⁺ ion

A.1 Atomic data for Mg

Isotope	Atomic mass (amu)	Abundance (%) [120]	Nuclear spin
24	23.985041700(14)	78.99(4)	0
25	24.98583692(3)	10.00(1)	5/2
26	25.982592929(30)	11.01(3)	0

Resonant transition for photoionization of ²⁴Mg ($3s^2\ ^1S_0 \leftrightarrow 3s3p\ ^1P_1$) [121]:

$$\lambda_{\text{vac}} = 285.2965\text{ nm}$$

$$\lambda_{\text{air}} = 285.2127\text{ nm}$$

A.2 Transition data for ²⁴Mg⁺

Doppler cooling transition of ²⁴Mg⁺ ($3s\ ^2S_{1/2} \leftrightarrow 3p\ ^2P_{3/2}$) [121]:

$$\lambda_{\text{vac}} = 279.6352\text{ nm}$$

$$\lambda_{\text{air}} = 279.5528\text{ nm}$$

$$\Gamma/2\pi = 41\text{ MHz}$$

$$\tau = 3.8\text{ ns}$$

Appendix B

The MgH⁺ ion

B.1 Transitions in the ²⁴MgH⁺ ion

General terminology used throughout the thesis:

$R_a(b)$ denotes the rovibrational $|v = 0, J = b\rangle_X \rightarrow |v = a, J = b + 1\rangle_X$ transition.

$P_a(b)$ denotes the rovibrational $|v = 0, J = b\rangle_X \rightarrow |v = a, J = b - 1\rangle_X$ transition.

$R(b)$ denotes the electronic $|v = 0, J = b\rangle_X \rightarrow |v = 0, J = b + 1\rangle_A$ transition.

$P(b)$ denotes the electronic $|v = 0, J = b\rangle_X \rightarrow |v = 0, J = b - 1\rangle_A$ transition.

Transition	Wavenumber (cm ⁻¹)	Vac. wavelength (μm)	Frequency (THz)
R ₀ (0)	12.59	794.53	0.378
R ₀ (1)	25.16	397.54	0.755
R ₀ (2)	37.82	264.43	1.135
R ₀ (3)	50.19	199.23	1.506
R ₀ (4)	62.85	159.12	1.885
R ₀ (5)	75.22	132.95	2.256
R ₀ (6)	87.66	114.07	2.630
R ₀ (7)	99.95	100.05	2.999
R ₀ (8)	112.30	89.05	3.369
R ₀ (9)	124.45	80.35	3.734

Table B.1: Data for some rotational transitions of interest. Calculated from [94].

Transition	Wavenumber (cm^{-1})	Vac. wavelength (nm)	Frequency (THz)
P ₁ (5)	1568.03	6377.45	47.041
P ₁ (4)	1582.06	6320.89	47.462
P ₁ (3)	1595.56	6267.41	47.867
P₁(2)	1608.96	6215.19	48.269
P ₁ (1)	1621.77	6166.11	48.653
R ₁ (0)	1646.70	6072.74	49.401
R ₁ (1)	1658.53	6029.44	49.756
R ₁ (2)	1670.07	5987.79	50.102
R ₁ (3)	1681.07	5948.61	50.432
R ₁ (4)	1691.86	5910.67	50.756

Table B.2: Data for some rovibrational transitions of interest. The transition used for the rotational cooling results of this thesis is shown in bold. Calculated from [94].

$ v, J\rangle_{\text{ini}}$	$\Delta v = 0$ $\Delta J = -1$	-1		-2		-3		-4		
		1	-1	1	-1	1	-1	1	-1	1
0	0									
	1	0.0023								
	2	0.022								
	3	0.081								
	4	0.199								
	5	0.396								
	6	0.691								
	7	1.104								
	8	1.652								
1	0									
	1	0.0020	6.139	15.753						
	2	0.020	7.955	9.701						
	3	0.070	9.195	8.059						
	4	0.172	10.277	7.079						
	5	0.343	11.316	6.345						
	6	0.599	12.358	5.740						
	7	0.957	13.424	5.219						
	8	1.430	14.527	4.760						
2	0									
	1	0.0017	14.061	36.614		2.676				
	2	0.017	18.093	22.721	0.802	1.872				
	3	0.060	20.773	19.025	0.907	1.762				
	4	0.147	23.065	16.851	0.911	1.750				
	5	0.293	25.237	15.231	0.883	1.769				
	6	0.511	27.392	13.899	0.839	1.800				
	7	0.816	29.579	12.750	0.787	1.838				
	8	1.220	31.826	11.735	0.731	1.878				
3	0									
	1	0.0015	23.391	61.632		5.918		0.633		
	2	0.014	29.927	38.480	1.741	4.172	0.202	0.431		
	3	0.050	34.167	32.422	1.947	3.953	0.236	0.396		
	4	0.124	37.731	28.899	1.934	3.949	0.247	0.385		
	5	0.246	41.063	26.289	1.847	4.012	0.250	0.382		
	6	0.429	44.335	24.147	1.728	4.103	0.248	0.382		
	7	0.684	47.630	22.299	1.592	4.205	0.245	0.383		
	8	1.021	50.991	20.661	1.448	4.311	0.241	0.386		
4	0									
	1	NC	33.466	89.030		7.861		2.501		0.053
	2	NC	42.614	55.856	2.245	5.609	0.795	1.704	0.017	0.036
	3	NC	48.423	47.292	2.466	5.372	0.931	1.567	0.020	0.033
	4	NC	53.224	42.360	2.399	5.417	0.972	1.523	0.021	0.032
	5	NC	57.656	38.723	2.237	5.549	0.981	1.509	0.021	0.031
	6	NC	61.966	35.742	2.035	5.715	0.975	1.510	0.021	0.031
	7	NC	66.268	33.167	1.816	5.893	0.961	1.517	0.021	0.031
	8	NC	70.624	30.879	1.589	6.073	0.942	1.529	0.021	0.031

Table B.3: Einstein A coefficients (Hz) for some rotational and rovibrational transitions, calculated in 2012 (see section 4.1.5). NC: Not calculated.

Appendix C

The Ca⁺ ion

C.1 Atomic data for Ca

Isotope	Atomic mass (amu)	Abundance (%) [120]	Nuclear spin
40	39.9625906(13)	96.941(156)	0
42	41.9586176(13)	0.647(23)	0
43	42.9587662(13)	0.135(10)	7/2
44	43.9554806(14)	2.086(110)	0
46	45.953689(4)	0.004(3)	0
48	47.952533(4)	0.187(21)	0

Resonant transition for photoionization of ⁴⁰Ca ($4s^2\ ^1S_0 \leftrightarrow 4s5p\ ^1P_1$) [121]:

$$\lambda_{\text{vac}} = 272.246 \text{ nm}$$

$$\lambda_{\text{air}} = 272.165 \text{ nm}$$

C.2 Transition data for ⁴⁰Ca⁺

Transition wavelengths:

	$4s\ ^2S_{1/2} \leftrightarrow 4p\ ^2P_{1/2}$	$3d\ ^2D_{3/2} \leftrightarrow 4p\ ^2P_{1/2}$	$3d\ ^2D_{5/2} \leftrightarrow 4p\ ^2P_{3/2}$
λ_{vac} [nm]	396.959	866.452	854.444
λ_{air} [nm]	396.847	866.214	854.209
$\Gamma/2\pi$ [MHz]	22	-	-

Radiative lifetimes:

$$4p\ ^2P_{1/2} \rightarrow 4s\ ^2S_{1/2} : \tau = 7.1 \text{ ns}$$

$$3d\ ^2D_{3/2} \rightarrow 4s\ ^2S_{1/2} : \tau = 0.77 \text{ s}$$

Bibliography

- [1] L. D. Carr, D. DeMille, R. V. Krems, and J. Ye, “Cold and ultracold molecules: science, technology and applications,” *New Journal of Physics*, vol. 11, no. 5, p. 055049, 2009.
- [2] J. C. J. Koelemeij, B. Roth, A. Wicht, I. Ernsting, and S. Schiller, “Vibrational Spectroscopy of HD^+ with 2-ppb Accuracy,” *Phys. Rev. Lett.*, vol. 98, p. 173002, Apr 2007.
- [3] J. J. Hudson, B. E. Sauer, M. R. Tarbutt, and E. A. Hinds, “Measurement of the electron electric dipole moment using YbF molecules,” *Phys. Rev. Lett.*, vol. 89, p. 023003, Jun 2002.
- [4] E. R. Hudson, H. J. Lewandowski, B. C. Sawyer, and J. Ye, “Cold molecule spectroscopy for constraining the evolution of the fine structure constant,” *Phys. Rev. Lett.*, vol. 96, p. 143004, Apr 2006.
- [5] O. Asvany, O. Ricken, H. S. P. Müller, M. C. Wiedner, T. F. Giesen, and S. Schlemmer, “High-resolution rotational spectroscopy in a cold ion trap: H_2D^+ and D_2H^+ ,” *Phys. Rev. Lett.*, vol. 100, p. 233004, Jun 2008.
- [6] K.-A. B. Soderberg, N. Gemelke, and C. Chin, “Ultracold molecules: vehicles to scalable quantum information processing,” *New Journal of Physics*, vol. 11, no. 5, p. 055022, 2009.
- [7] D. DeMille, “Quantum computation with trapped polar molecules,” *Phys. Rev. Lett.*, vol. 88, p. 067901, Jan 2002.
- [8] A. André, D. DeMille, J. M. Doyle, M. D. Lukin, S. E. Maxwell, P. Rabl, R. J. Schoelkopf, and P. Zoller, “A coherent all-electrical interface between polar molecules and mesoscopic superconducting resonators,” *Nature Phys.*, vol. 2, pp. 636–642, 2006.
- [9] P. Hlavenka, R. Otto, S. Trippel, J. Mikosch, M. Weidemüller, and R. Wester, “Absolute photodetachment cross section measurements of the O^- and OH^- anion,” *The Journal of Chemical Physics*, vol. 130, p. 061105, Feb. 2009.
- [10] S. A. Rice and M. Zhao, *Optical control of molecular dynamics*. New York: John Wiley & Sons, 2000.
- [11] M. Shapiro and P. Brumer, “Coherent control of molecular dynamics,” *Reports on Progress in Physics*, vol. 66, no. 6, p. 859, 2003.

- [12] S. Willitsch, M. T. Bell, A. D. Gingell, and T. P. Softley, “Chemical applications of laser- and sympathetically-cooled ions in ion traps,” *Phys. Chem. Chem. Phys.*, vol. 10, pp. 7200–7210, 2008.
- [13] R. V. Krems, “Cold controlled chemistry,” *Phys. Chem. Chem. Phys.*, vol. 10, pp. 4079–4092, 2008.
- [14] D. Gerlich and M. Smith, “Laboratory astrochemistry: studying molecules under inter- and circumstellar conditions,” *Physica Scripta*, vol. 73, no. 1, p. C25, 2006.
- [15] S. Schiller and V. Korobov, “Tests of time independence of the electron and nuclear masses with ultracold molecules,” *Phys. Rev. A*, vol. 71, p. 032505, Mar 2005.
- [16] M. Kajita, “Prospects of detecting m_e/m_p variance using vibrational transition frequencies of $^2\Sigma$ -state molecules,” *Phys. Rev. A*, vol. 77, p. 012511, Jan 2008.
- [17] C. Chin, V. V. Flambaum, and M. G. Kozlov, “Ultracold molecules: new probes on the variation of fundamental constants,” *New Journal of Physics*, vol. 11, no. 5, p. 055048, 2009.
- [18] E. R. Meyer, J. L. Bohn, and M. P. Deskevich, “Candidate molecular ions for an electron electric dipole moment experiment,” *Phys. Rev. A*, vol. 73, p. 062108, Jun 2006.
- [19] R. Sahai and L. Åke Nyman, “The Boomerang Nebula: The coldest region of the universe?,” *The Astrophysical Journal Letters*, vol. 487, no. 2, p. L155, 1997.
- [20] E. Herbst and T. J. Millar, *Low temperatures and cold molecules*. World Scientific Publishing, 2008.
- [21] A. V. Avdeenkov and J. L. Bohn, “Linking ultracold polar molecules,” *Phys. Rev. Lett.*, vol. 90, p. 043006, Jan 2003.
- [22] E. S. Shuman, J. F. Barry, and D. DeMille, “Laser cooling of a diatomic molecule,” *Nature*, vol. 467, pp. 820–823. 10 p, Mar 2011.
- [23] J. T. Bahns, W. C. Stwalley, and P. L. Gould, “Laser cooling of molecules: A sequential scheme for rotation, translation, and vibration,” *The Journal of Chemical Physics*, vol. 104, no. 24, pp. 9689–9697, 1996.

- [24] M. D. D. Rosa, “Laser-cooling molecules,” *The European Physical Journal D - Atomic, Molecular, Optical and Plasma Physics*, vol. 31, no. 2, pp. 395–402, 2004.
- [25] P. D. Lett, K. Helmerson, W. D. Phillips, L. P. Ratliff, S. L. Rolston, and M. E. Wagshul, “Spectroscopy of Na_2 by photoassociation of laser-cooled na,” *Phys. Rev. Lett.*, vol. 71, pp. 2200–2203, Oct 1993.
- [26] A. Fioretti, D. Comparat, A. Crubellier, O. Dulieu, F. Masnou-Seeuws, and P. Pillet, “Formation of cold Cs_2 molecules through photoassociation,” *Phys. Rev. Lett.*, vol. 80, pp. 4402–4405, May 1998.
- [27] M. Viteau, A. Chotia, M. Allegrini, N. Bouloufa, O. Dulieu, D. Comparat, and P. Pillet, “Optical pumping and vibrational cooling of molecules,” *Science*, vol. 321, no. 5886, pp. 232–234, 2008.
- [28] J. D. Weinstein, R. deCarvalho, T. Guillet, B. Friedrich, and J. M. Doyle, “Magnetic trapping of calcium monohydride molecules at millikelvin temperatures,” *Nature*, vol. 395, p. 148, 1998.
- [29] H. L. Bethlem, G. Berden, and G. Meijer, “Decelerating neutral dipolar molecules,” *Phys. Rev. Lett.*, vol. 83, pp. 1558–1561, Aug 1999.
- [30] E. R. Hudson, C. Ticknor, B. C. Sawyer, C. A. Taatjes, H. J. Lewandowski, J. R. Bochinski, J. L. Bohn, and J. Ye, “Production of cold formaldehyde molecules for study and control of chemical reaction dynamics with hydroxyl radicals,” *Phys. Rev. A*, vol. 73, p. 063404, Jun 2006.
- [31] S. A. Rangwala, T. Junglen, T. Rieger, P. W. H. Pinkse, and G. Rempe, “Continuous source of translationally cold dipolar molecules,” *Phys. Rev. A*, vol. 67, p. 043406, Apr 2003.
- [32] H. L. Bethlem, G. Berden, F. M. H. Cromptoets, R. T. Jongma, A. J. A. van Rooij, and G. Meijer, “Electrostatic trapping of ammonia molecules,” *Nature*, vol. 406, 2000.
- [33] T. Rieger, T. Junglen, S. A. Rangwala, P. W. H. Pinkse, and G. Rempe, “Continuous loading of an electrostatic trap for polar molecules,” *Phys. Rev. Lett.*, vol. 95, p. 173002, Oct 2005.
- [34] S. Hoekstra, J. J. Gilijamse, B. Sartakov, N. Vanhaecke, L. Scharfenberg, S. Y. T. van de Meerakker, and G. Meijer, “Optical pumping of trapped

- neutral molecules by blackbody radiation,” *Phys. Rev. Lett.*, vol. 98, p. 133001, Mar 2007.
- [35] S. Jochim, M. Bartenstein, A. Altmeyer, G. Hendl, S. Riedl, C. Chin, J. Hecker Denschlag, and R. Grimm, “Bose-Einstein condensation of molecules,” *Science*, vol. 302, no. 5653, pp. 2101–2103, 2003.
- [36] M. Greiner, C. A. Regal, and D. S. Jin, “Emergence of a molecular Bose-Einstein condensate from a Fermi gas,” *Nature*, vol. 426, 2003.
- [37] E. Kuznetsova, M. Gacesa, P. Pellegrini, S. F. Yelin, and R. Côté, “Efficient formation of ground-state ultracold molecules via STIRAP from the continuum at a Feshbach resonance,” *New Journal of Physics*, vol. 11, no. 5, p. 055028, 2009.
- [38] K.-K. Ni, S. Ospelkaus, M. H. G. de Miranda, A. Pe’er, B. Neyenhuis, J. J. Zirbel, S. Kotochigova, P. S. Julienne, D. S. Jin, and J. Ye, “A high phase-space-density gas of polar molecules,” *Science*, vol. 322, no. 5899, pp. 231–235, 2008.
- [39] S. Ospelkaus, A. Pe’er, K.-K. Ni, J. J. Zirbel, B. Neyenhuis, S. Kotochigova, P. S. Julienne, J. Ye, and D. S. Jin, “Efficient state transfer in an ultracold dense gas of heteronuclear molecules,” *Nat Phys*, vol. 4, 2008.
- [40] J. G. Danzl, E. Haller, M. Gustavsson, M. J. Mark, R. Hart, N. Bouloufa, O. Dulieu, H. Ritsch, and H.-C. Nägerl, “Quantum gas of deeply bound ground state molecules,” *Science*, vol. 321, no. 5892, pp. 1062–1066, 2008.
- [41] J. Deiglmayr, A. Grochola, M. Repp, K. Mörtilbauer, C. Glück, J. Lange, O. Dulieu, R. Wester, and M. Weidemüller, “Formation of ultracold polar molecules in the rovibrational ground state,” *Phys. Rev. Lett.*, vol. 101, p. 133004, Sep 2008.
- [42] D. Gerlich, “Ion-neutral collisions in a 22-pole trap at very low energies,” *Physica Scripta*, vol. 1995, no. T59, p. 256, 1995.
- [43] D. Gerlich and G. Borodi, “Buffer gas cooling of polyatomic ions in rf multi-electrode traps,” *Faraday Discussions*, vol. 142, pp. 57–72, 2009.
- [44] O. Asvany, F. Biela, D. Moratschke, J. Krause, and S. Schlemmer, “Note: New design of a cryogenic linear radio frequency multipole trap,” *Review of Scientific Instruments*, vol. 81, 2010.

- [45] K. Mølhave, “Construction of and experiments with a linear Paul trap,” Master’s thesis, University of Aarhus, 2000.
- [46] K. Højbjerg, *Experiments with cold trapped molecular ions*. PhD thesis, Danish National Research Foundation Center for Quantum Optics - Quantop Department of Physics and Astronomy, The University of Aarhus, 2009.
- [47] M. Drewsen, I. Jensen, J. Lindballe, N. Nissen, R. Martinussen, A. Mortensen, P. Sta anum, and D. Voigt, “Ion Coulomb crystals: a tool for studying ion processes,” *International Journal of Mass Spectrometry*, vol. 229, no. 1-2, pp. 83–91, 2003.
- [48] M. Drewsen, A. Mortensen, R. Martinussen, P. Sta anum, and J. L. Sørensen, “Nondestructive identification of cold and extremely localized single molecular ions,” *Phys. Rev. Lett.*, vol. 93, p. 243201, Dec 2004.
- [49] P. Blythe, B. Roth, U. Fröhlich, H. Wenz, and S. Schiller, “Production of ultracold trapped molecular hydrogen ions,” *Phys. Rev. Lett.*, vol. 95, p. 183002, Oct 2005.
- [50] A. Ostendorf, C. B. Zhang, M. A. Wilson, D. Offenber g, B. Roth, and S. Schiller, “Sympathetic cooling of complex molecular ions to millikelvin temperatures,” *Phys. Rev. Lett.*, vol. 97, p. 243005, Dec 2006.
- [51] K. Højbjerg, D. Offenber g, C. Z. Bisgaard, H. Stapelfeldt, P. F. Sta anum, A. Mortensen, and M. Drewsen, “Consecutive photodissociation of a single complex molecular ion,” *Phys. Rev. A*, vol. 77, p. 030702, Mar 2008.
- [52] P. F. Sta anum, K. Højbjerg, R. Wester, and M. Drewsen, “Probing isotope effects in chemical reactions using single ions,” *Physical Review Letters*, vol. 100, no. 24, pp. 243003+, 2008.
- [53] X. Tong, A. H. Winney, and S. Willitsch, “Sympathetic cooling of molecular ions in selected rotational and vibrational states produced by threshold photoionization,” *Phys. Rev. Lett.*, vol. 105, p. 143001, Sep 2010.
- [54] S. Willitsch, M. T. Bell, A. D. Gingell, S. R. Procter, and T. P. Softley, “Cold reactive collisions between laser-cooled ions and velocity-selected neutral molecules,” *Phys. Rev. Lett.*, vol. 100, p. 043203, Jan 2008.

- [55] A. T. Grier, M. Cetina, F. Oručević, and V. Vuletić, “Observation of cold collisions between trapped ions and trapped atoms,” *Phys. Rev. Lett.*, vol. 102, p. 223201, Jun 2009.
- [56] C. Zipkes, S. Palzer, C. Sias, and M. Köhl, “A trapped single ion inside a Bose-Einstein condensate,” *Nature*, vol. 464, 2010.
- [57] S. Schmid, A. Härter, and J. H. Denschlag, “Dynamics of a cold trapped ion in a Bose-Einstein condensate,” *Phys. Rev. Lett.*, vol. 105, p. 133202, Sep 2010.
- [58] R. Côté, V. Kharchenko, and M. D. Lukin, “Mesoscopic molecular ions in Bose-Einstein condensates,” *Phys. Rev. Lett.*, vol. 89, p. 093001, Aug 2002.
- [59] J. Mikosch, H. Kreckel, R. Wester, R. Plašil, J. Glosík, D. Gerlich, D. Schwalm, and A. Wolf, “Action spectroscopy and temperature diagnostics of H_3^+ by chemical probing,” *The Journal of Chemical Physics*, vol. 121, no. 22, p. 11030, 2004.
- [60] J. Glosík, P. Hlavenka, R. Plašil, F. Windisch, D. Gerlich, A. Wolf, and H. Kreckel, “Action spectroscopy of H_3^+ and D_2H^+ using overtone excitation,” *Phil. Trans. R. Soc. A*, vol. 364, no. 1848, pp. 2931–2942, 2006.
- [61] S. Schlemmer, T. Kuhn, E. Lescop, and D. Gerlich, “Laser excited N_2^+ in a 22-pole ion trap:: Experimental studies of rotational relaxation processes,” *International Journal of Mass Spectrometry*, vol. 185–187, no. 0, pp. 589 – 602, 1999.
- [62] K. Mølhave and M. Drewsen, “Formation of translationally cold MgH^+ and MgD^+ molecules in an ion trap,” *Phys. Rev. A*, vol. 62, p. 011401, Jun 2000.
- [63] I. S. Vogelius, L. B. Madsen, and M. Drewsen, “Blackbody-radiation-assisted laser cooling of molecular ions,” *Phys. Rev. Lett.*, vol. 89, p. 173003, Oct 2002.
- [64] N. Kjærgaard, *Methods in Laser Cooling of Ions in Storage Rings and Traps*. PhD thesis, Danish National Research Foundation Center for Quantum Optics - Quantop Department of Physics and Astronomy, The University of Aarhus, 2001.

- [65] A. Mortensen, *Aspects of Ion Coulomb Crystal based Quantum Memory for Light*. PhD thesis, Danish National Research Foundation Center for Quantum Optics - Quantop Department of Physics and Astronomy, The University of Aarhus, 2005.
- [66] G. Poulsen, *Sideband Cooling of Atomic and Molecular Ions*. PhD thesis, Danish National Research Foundation Center for Quantum Optics - Quantop Department of Physics and Astronomy, The University of Aarhus, 2011.
- [67] A. Mortensen, J. J. T. Lindballe, I. S. Jensen, P. Staantum, D. Voigt, and M. Drewsen, “Isotope shifts of the $4s^2\ ^1S_0 \rightarrow 4s5p\ ^1P_1$ transition and hyperfine splitting of the $4s5p\ ^1P_1$ state in calcium,” *Phys. Rev. A*, vol. 69, p. 042502, Apr 2004.
- [68] D. N. Madsen, S. Balslev, M. Drewsen, N. Kjærgaard, Z. Videsen, and J. W. Thomsen, “Measurements on photo-ionization of $3s3p\ ^1P_1$ magnesium atoms,” *Journal of Physics B: Atomic, Molecular and Optical Physics*, vol. 33, no. 22, p. 4981, 2000.
- [69] W. D. Phillips, “Nobel lecture: Laser cooling and trapping of neutral atoms,” *Rev. Mod. Phys.*, vol. 70, pp. 721–741, Jul 1998.
- [70] H. J. Metcalf and P. van Straten, *Laser cooling and trapping*. New York; Berlin; Heidelberg: Springer, 1999.
- [71] P. Herskind, *Cavity Quantum Electrodynamics with Ion Coulomb Crystals*. PhD thesis, Danish National Research Foundation Center for Quantum Optics - Quantop Department of Physics and Astronomy, The University of Aarhus, 2008.
- [72] G. Morigi and H. Walther, “Two-species Coulomb chains for quantum information,” *The European Physical Journal D - Atomic, Molecular, Optical and Plasma Physics*, vol. 13, pp. 261–269, 2001.
- [73] N. Kjærgaard, L. Hornekær, A. M. Thommesen, Z. Videsen, and M. Drewsen, “Isotope selective loading of an ion trap using resonance-enhanced two-photon ionization,” *Applied Physics B: Lasers and Optics*, vol. 71, no. 2, pp. 207–210, 2000.
- [74] P. Herskind, J. Lindballe, C. Clausen, J. L. Sørensen, and M. Drewsen, “Second-harmonic generation of light at 544 and 272 nm from an

- ytterbium-doped distributed-feedback fiber laser,” *Optics Letters*, vol. 32, no. 3, pp. 268–270, 2007.
- [75] “Menlo Systems website.”
<http://www.menlosystems.com/>.
- [76] F. L. Pedrotti, L. M. Pedrotti, and L. S. Pedrotti, *Introduction to Optics*. Pearson Education, 2007.
- [77] P. W. Milonni and J. H. Eberly, *Lasers*. Wiley, 1988.
- [78] G. D. Boyd and D. A. Kleinman, “Parametric interaction of focused Gaussian light beams,” *Journal of Applied Physics*, vol. 39, no. 8, pp. 3597–3639, 1968.
- [79] H. Kogelnik and T. Li, “Laser beams and resonators,” *Appl. Opt.*, vol. 5, pp. 1550–1567, Oct 1966.
- [80] A. Ashkin, G. Boyd, and J. Dziedzic, “Resonant optical second harmonic generation and mixing,” *Quantum Electronics, IEEE Journal of*, vol. 2, pp. 109 – 124, Jun 1966.
- [81] A. Borsutzky, R. Brüngrer, C. Huang, and R. Wallenstein, “Harmonic and sum-frequency generation of pulsed laser radiation in BBO, LBO, and KD*P,” *Applied Physics B: Lasers and Optics*, vol. 52, pp. 55–62, 1991.
- [82] K. Kato, “Second-harmonic generation to 2048 Å in β -BaB₂O₄,” *Quantum Electronics, IEEE Journal of*, vol. 22, pp. 1013 – 1014, Jul 1986.
- [83] “Encyclopedia of Laser Physics and Technology website.”
http://www.rp-photonics.com/spatial_walk_off.html.
- [84] T. Hansch and B. Couillaud, “Laser frequency stabilization by polarization spectroscopy of a reflecting reference cavity,” *Optics Communications*, vol. 35, no. 3, pp. 441 – 444, 1980.
- [85] S. Feng and H. G. Winful, “Physical origin of the Gouy phase shift,” *Opt. Lett.*, vol. 26, no. 8, pp. 485–487, 2001.
- [86] T. Ukachi, R. J. Lane, W. R. Bosenberg, and C. L. Tang, “Measurements of noncritically phase-matched second-harmonic generation in a LiB₃O₅ crystal,” *Applied Physics Letters*, vol. 57, no. 10, p. 980, 1990.

- [87] “Newlight Photonics Inc. website, LBO properties.”
<http://www.newlightphotonics.com/lbo-properties.html>.
- [88] R. W. P. Drever, J. L. Hall, F. V. Kowalski, J. Hough, G. M. Ford, A. J. Munley, and H. Ward, “Laser phase and frequency stabilization using an optical resonator,” *Applied Physics B: Lasers and Optics*, vol. 31, pp. 97–105, 1983.
- [89] E. D. Black, “An introduction to Pound-Drever-Hall laser frequency stabilization,” *American Journal of Physics*, vol. 69, no. 1, pp. 79–87, 2001.
- [90] “Ferropem Piezoceramics website.”
<http://www.ferropem-piezo.com/>.
- [91] A. Bertelsen, S. Jørgensen, and M. Drewsen, “The rotational temperature of polar molecular ions in Coulomb crystals,” *Journal of Physics B: Atomic, Molecular and Optical Physics*, vol. 39, no. 5, p. L83, 2006.
- [92] J. C. J. Koelemeij, B. Roth, and S. Schiller, “Blackbody thermometry with cold molecular ions and application to ion-based frequency standards,” *Phys. Rev. A*, vol. 76, p. 023413, Aug 2007.
- [93] B. H. Bransden and C. J. Joachain, *Physics of Atoms and Molecules*. Pearson Education, 2003.
- [94] W. J. Balfour, “Rotational analysis of the $A^1\Sigma^+ \rightarrow X^1\Sigma^+$ and $B^1\Pi \rightarrow X^1\Sigma^+$ systems of $^{24}\text{Mg}^+$, $^{25}\text{Mg}^+$ and $^{26}\text{Mg}^+$,” *Can. J. Phys.*, vol. 50, pp. 1082–1091, 1971.
- [95] M. J. F. et al., “Gaussian 09 Revision A.1.” Gaussian Inc. Wallingford CT 2009.
- [96] R. J. L. Roy, *LEVEL 8.0*, 2001.
- [97] I. S. Vogelius, *Cooling and Manipulating Trapped Molecular Ions*. PhD thesis, Department of Physics and Astronomy, University of Aarhus, 2005.
- [98] K. Bergmann and E. Gottwald, “Effect of optical pumping in two-step photoionization of Na_2 in molecular beams,” *Chem. Phys. Lett.*, vol. 78, no. 3, pp. 515–519, 1980.

- [99] P. S. Skyt, “Rotational laser cooling of vibrationally and translationally cold MgH^+ ions,” Master’s thesis, Danish National Research Foundation Center for Quantum Optics - Quantop Department of Physics and Astronomy, The University of Aarhus, 2009.
- [100] “Daylight Solutions website.”
<http://www.daylightsolutions.com>.
- [101] S. B. Kristensen, “Rotational manipulation of the MgH^+ molecule,” Master’s thesis, Danish National Research Foundation Center for Quantum Optics - Quantop Department of Physics and Astronomy, The University of Aarhus, 2012.
- [102] L. Hornekær, N. Kjærgaard, A. M. Thommesen, and M. Drewsen, “Structural properties of two-component Coulomb crystals in linear Paul traps,” *Physical Review Letters*, vol. 86, no. 10, pp. 1994–1997, 2001.
- [103] K. Højbjerg, A. K. Hansen, P. S. Skyt, P. F. Staantum, and M. Drewsen, “Rotational state resolved photodissociation spectroscopy of translationally and vibrationally cold MgH^+ ions: Toward rotational cooling of molecular ions,” *New J. Phys.*, vol. 11, p. 055026, 2009.
- [104] P. F. Staantum, K. Højbjerg, P. S. Skyt, A. K. Hansen, and M. Drewsen, “Rotational laser cooling of vibrationally and translationally cold molecular ions,” *Nature Physics*, vol. 6, pp. 271–274, 2010.
- [105] T. Schneider, B. Roth, H. Duncker, I. Ernsting, and S. Schiller, “All-optical preparation of molecular ions in the rovibrational ground state,” *Nature Phys.*, 2010.
- [106] G. Barinovs, G. Nyman, and S. Andersson, “Rotational transitions of CO^+ induced by atomic hydrogen,” *Molecules in Space & Laboratory*, 2007.
- [107] R. D. Levine, *Molecular Reaction Dynamics*. Cambridge: Cambridge University Press, 2005.
- [108] T. N. Olney, N. Cann, G. Cooper, and C. Brion, “Absolute scale determination for photoabsorption spectra and the calculation of molecular properties using dipole sum-rules,” *Chemical Physics*, vol. 223, no. 1, pp. 59 – 98, 1997.

- [109] M. Schwarz, O. O. Versolato, A. Windberger, F. R. Brunner, T. Ballance, S. N. Eberle, J. Ullrich, P. O. Schmidt, A. K. Hansen, A. D. Gingell, M. Drewsen, and J. R. C. López-Urrutia, “Cryogenic linear Paul trap for cold highly charged ion experiments,” *Review of Scientific Instruments*, vol. 83, no. 8, 2012.
- [110] M. Schwarz, *Lasermanipulation von rotationsgekühlten Molekülionen in einer neuen kryogenen Paul-Falle*. PhD thesis, Max-Planck-Institut für Kernphysik & Ruprecht-Karls-Universität Heidelberg, 2009.
- [111] A. K. Hansen, M. A. Sørensen, P. F. Staantum, and M. Drewsen, “Single-ion recycling reactions,” *Angewandte Chemie International Edition*, vol. 51, no. 32, pp. 7960–7962, 2012.
- [112] M. Gupta and T. W. Burrows, “Nuclear data sheets for $A = 266$ –294,” *Nuclear Data Sheets*, vol. 106, no. 2, pp. 251 – 366, 2005.
- [113] T. Millar, “Deuterium fractionation in interstellar clouds,” *Space Science Reviews*, vol. 106, pp. 73–86, 2003.
- [114] P. D. Kleiber and J. Chen, “Spectroscopy and chemical dynamics of weakly bound alkaline-earth metal ion-H and alkaline-earth metal ion-hydrocarbon complexes 2,” *International Reviews in Physical Chemistry*, vol. 17, no. 1, pp. 1–34, 1998.
- [115] P. F. Staantum, K. Højbjerg, R. Wester, and M. Drewsen, “Probing isotope effects in chemical reactions using single ions,” *Phys. Rev. Lett.*, vol. 100, p. 243003, Jun 2008.
- [116] N. F. Dalleska, K. C. Crellin, and P. B. Armentrout, “Reactions of alkaline earth ions with hydrogen, deuterium, and hydrogen deuteride,” *The Journal of Physical Chemistry*, vol. 97, no. 13, pp. 3123–3128, 1993.
- [117] E. Czuchaj, M. Krosnicki, and H. Stoll, “Theoretical study of ground and excited state potential energy surfaces for the $\text{Ca}^+\text{-H}_2$ complex,” *Molecular Physics*, vol. 98, no. 7, pp. 419–427, 2000.
- [118] A. J. Page, D. J. D. Wilson, and E. I. von Nagy-Felsobuki, “Trends in MH_2^{n+} ion-quadrupole complexes ($\text{M} = \text{Li}, \text{Be}, \text{Na}, \text{Mg}, \text{K}, \text{Ca}; n = 1, 2$) using ab initio methods,” *Phys. Chem. Chem. Phys.*, vol. 12, pp. 13788–13797, 2010.

- [119] A. Boutalib, J. P. Daudey, and M. E. Mouhtadi, "Theoretical study of the lowest electronic states of CaH and CaH⁺ molecules," *Chemical Physics*, vol. 167, no. 1-2, pp. 111 – 120, 1992.
- [120] K. J. R. Rosman and P. D. P. Taylor, "Isotopic compositions of the elements 1997 (Technical Report)," *Pure & Appl. Chem.*, vol. 70, no. 1, pp. 217–235, 1998.
- [121] "National Institute of Standards and Technology (NIST) Atomic Spectra Database."
http://physics.nist.gov/PhysRefData/ASD/lines_form.html.